

Optically and environmentally responsive fibres

Citation for published version (APA):

Dai, M. (2013). *Optically and environmentally responsive fibres*. [Phd Thesis 1 (Research TU/e / Graduation TU/e), Chemical Engineering and Chemistry]. Technische Universiteit Eindhoven.
<https://doi.org/10.6100/IR756860>

DOI:

[10.6100/IR756860](https://doi.org/10.6100/IR756860)

Document status and date:

Published: 01/01/2013

Document Version:

Publisher's PDF, also known as Version of Record (includes final page, issue and volume numbers)

Please check the document version of this publication:

- A submitted manuscript is the version of the article upon submission and before peer-review. There can be important differences between the submitted version and the official published version of record. People interested in the research are advised to contact the author for the final version of the publication, or visit the DOI to the publisher's website.
- The final author version and the galley proof are versions of the publication after peer review.
- The final published version features the final layout of the paper including the volume, issue and page numbers.

[Link to publication](#)

General rights

Copyright and moral rights for the publications made accessible in the public portal are retained by the authors and/or other copyright owners and it is a condition of accessing publications that users recognise and abide by the legal requirements associated with these rights.

- Users may download and print one copy of any publication from the public portal for the purpose of private study or research.
- You may not further distribute the material or use it for any profit-making activity or commercial gain
- You may freely distribute the URL identifying the publication in the public portal.

If the publication is distributed under the terms of Article 25fa of the Dutch Copyright Act, indicated by the "Taverne" license above, please follow below link for the End User Agreement:

www.tue.nl/taverne

Take down policy

If you believe that this document breaches copyright please contact us at:

openaccess@tue.nl

providing details and we will investigate your claim.

Optically and Environmentally Responsive Fibres

PROEFSCHRIFT

ter verkrijging van de graad van doctor aan de Technische Universiteit Eindhoven, op gezag van de rector magnificus prof.dr.ir. C.J. van Duijn, voor een commissie aangewezen door het College voor Promoties, in het openbaar te verdedigen op woensdag 21 augustus 2013 om 16:00 uur

door

Mian Dai

geboren te Changzhou, China

Dit proefschrift is goedgekeurd door de promotiecommissie:

Voorzitter: prof.dr.ir. R.A.J. Janssen
1^o promotor: prof.dr. D.J. Broer
copromotor: prof.dr.ing. C.W.M. Bastiaansen
leden: prof.dr.ing. A.A.J.M. Peijs (Queen Mary, University
of London)
dr. J.G.H. Joosten (DSM, Dutch Polymer Institute)
dr. A.P.H.J. Schenning
adviseurs: dr.ir. J.G.P. Goossens
prof.dr.ir. J.M.J. den Toonder

A catalogue record is available from the Eindhoven University of Technology Library

ISBN: 978-90-386-3414-2

Copyright © 2013 by Mian Dai

This research forms part of the research programme of the Dutch Polymer Institute (DPI), project # 679.



Contents

SUMMARY	V
1 INTRODUCTION.....	1
1.1 AN OVERVIEW OF SMART TEXTILES	1
1.2 APPEARANCE OF TEXTILE FIBRES	3
1.2.1 <i>Specific die design</i>	5
1.2.2 <i>Mechanical embossing</i>	5
1.2.3 <i>Photoembossing</i>	6
1.3 RESPONSIVE TEXTILE FIBRES	7
1.3.1 <i>Liquid crystals</i>	8
1.3.2 <i>Liquid crystal polymer actuator</i>	10
1.4 MOTIVATION AND OBJECTIVE OF THE THESIS.....	14
1.5 ORGANISATION AND SCOPE OF THE THESIS	15
1.6 REFERENCES	16
2 MODELLING OF DIFFRACTION GRATINGS	23
2.1 INTRODUCTION	23
2.2 ANGULAR DISPERSION	23
2.3 DIFFRACTION EFFICIENCY.....	25
2.3.1 <i>Diffraction efficiency at normal incidence</i>	26
2.3.2 <i>Angular-dependent diffraction efficiency</i>	27
2.4 GRATINGS ON CURVED SURFACES	30
2.5 CONCLUSIONS.....	31
2.6 REFERENCES	31
3 PHOTOEMBOSSING VIA MASK EXPOSURE.....	33
3.1 INTRODUCTION	33
3.2 EXPERIMENTAL.....	34
3.3 RESULTS AND DISCUSSION	36

3.4 CONCLUSIONS	41
3.5 REFERENCES	42
4 PHOTOEMBOSSING VIA INTERFERENCE HOLOGRAPHY.....	45
4.1 INTRODUCTION	45
4.2 EXPERIMENTAL.....	46
4.3 RESULTS AND DISCUSSION	49
4.3.1 <i>Interference holography using CW and pulsed laser</i>	49
4.3.2 <i>RT photoembossing versus HT photoembossing</i>	52
4.4 CONCLUSIONS	59
4.5 REFERENCES	59
5 SURFACE STRUCTURING OF FIBRES USING PHOTOEMBOSSING.	61
5.1 INTRODUCTION	61
5.2 SURFACE STRUCTURING OF SINGLE FIBRES	62
5.2.1 <i>Experimental</i>	62
5.2.2 <i>Results and discussion</i>	65
5.3 SURFACE STRUCTURING OF BI-COMPONENT FIBRES.....	71
5.3.1 <i>Experimental</i>	72
5.3.2 <i>Results and discussion</i>	75
5.4 CONCLUSIONS	78
5.5 REFERENCES	79
6 HUMIDITY RESPONSIVE BILAYER ACTUATOR VIA BENDING.....	81
6.1 INTRODUCTION	81
6.2 HUMIDITY RESPONSIVE LC POLYMER.....	83
6.3 EXPERIMENTAL.....	86
6.4 RESULTS AND DISCUSSION	89
6.5 CONCLUSIONS.....	95
6.6 REFERENCES	96
7 HUMIDITY RESPONSIVE BILAYER ACTUATOR VIA CURLING	99

7.1 INTRODUCTION	99
7.2 EXPERIMENTAL.....	101
7.3 RESULTS.....	102
7.4 DISCUSSION	106
7.5 CONCLUSIONS.....	110
7.6 REFERENCES	110
8 TECHNICAL ASSESSMENT	113
8.1 INTRODUCTION	113
8.2 TEXTILES FOR FASHION DESIGN.....	113
8.3 BIOMEDICAL APPLICATION	114
8.4 BREATHABLE TEXTILES	115
8.5 STRAIN SENSOR.....	118
8.6 RECOMMENDATIONS FOR FUTURE RESEARCH	119
8.7 REFERENCES	120
APPENDIX A: ANISOTROPIC DEFORMATION OF LC POLYMER ACTUATOR.....	123
APPENDIX B: CALCULATION OF DIRECTOR ROTATION ANGLE..	125
SAMENVATTING.....	127
ACKNOWLEDGEMENTS.....	131
CURRICULUM VITAE.....	135
PUBLICATIONS	136

Summary

Optically and Environmentally Responsive Fibres

Smart textiles represent the next generation of fibres, fabrics and the articles produced from them. This new generation of "intelligent clothing" makes considerable new demands on the innovative ability within academia and industry and potentially offers new applications. The thesis is aimed at the creation of new functionalities into textile fibres, woven and non-woven fabrics related to visual perception or responsiveness to external triggers such as humidity.

Traditionally, inorganic or organic dyes are used to produce colours in textiles, which are based on absorption of light. These conventional fibres usually have a smooth surface and appear to have a single, angular-independent colour. To satisfy the requirements of fashion designers for novel visual effects, novel techniques were explored to obtain visual effects based on diffraction of visual light, which can be achieved by the creation of nano- and/or micro-structures on the surface of fibres.

The accurate nano- and/or micro-structuring of textile fibres remains an issue especially if relief structures perpendicular to the fibre axis are desired. Photoembossing is a comparatively new technique to produce such surface relief structures without etching procedures, which potentially facilitates incorporation of the process in a spinning line. Usually the photoembossing procedure includes formation of a film on a substrate, patterned UV exposure at room temperature via mask or interference holography, thermal development and flood exposure. A typical photopolymer mixture consists of a polymeric binder such as poly(benzyl methacrylate) (PBMA) and a multifunctional monomer (dipentaerythritol penta-/hexa- acrylate) (DPPHA) in a 1/1 ratio and the mixture is a solid and non-tacky material at room temperature. In this thesis, a new mixture for photoembossing is presented which contains a polymer binder with a higher glass transition

temperature (T_g) such as poly(methyl methacrylate) (PMMA). This results in mixtures that are solid at room temperature even at high monomer contents ($> 1/1$), which enhances the height of the relief structures, especially for the larger pitches. Interference holography with a pulsed laser was investigated to generate patterns in moving objects, such as fibres in a high speed spinning line. High temperature photoembossing was developed. The patterned exposure is done at an elevated temperature instead of room temperature. As a result, the height of the surface relief structures is increased by a factor ~ 2 while the optimal exposure energy is reduced.

The PMMA-DPPHA photopolymer mixture was directly spun into a monofilament fibre and surface relief structures were generated perpendicular to fibre axis by photoembossing using a photo-mask exposure. The experimental results show that structured fibres are produced with well-defined surface relief structures at optimised conditions. However, the fibres are rather brittle which is related to the crosslinked chemical network in the fibres. To improve the mechanical properties, a bi-component fibre system was explored, which consists of a conventional synthetic core fibre, such as PET or PA6 fibre, and a photopolymer coating. High temperature photoembossing using pulsed laser interference holography was performed to obtain diffractive grating structures with the grating vector along the fibre axis. The results demonstrate that the diffraction efficiency of visible light can be optimised in accordance with Rigorous Coupled-Wave Analysis (RCWA) and a relatively small grating pitch is selected to obtain a high wavelength dispersion. The obtained structured fibres with proper grating pitch exhibit clearly separated, distinct colours at different viewing angles.

Simultaneously, this thesis aims to develop responsive fibres based on liquid crystalline networks that respond to external stimuli such as temperature, humidity and/or UV-light. Here, the prime objective is to develop fibres that

respond to humidity via bending and/or curling. In a fabric it is expected that these deformations of the fibres can change the water vapour transmission and air permeability. To create humidity sensitive fibres, dedicated liquid crystal coatings consisting of a chemical network having hydrogen-bonded entities were explored which respond to a change in humidity after activation. As a model system, a stretched polymer tape is utilised to induce the alignment in the liquid crystal network. Thus, a well-aligned liquid crystal network coating is generated on the surface of the oriented polymer substrate. A bilayer actuator is created. It responds to humidity changes with a mechanical deformation, for instance, bending or curling deformation depending on the alignment of liquid crystal network. A splay aligned liquid crystal network is first generated without using any chiral dopant so that a bending deformation is obtained in the bilayer system. The influences of the substrate thickness and width on the bending deformation of the bilayer system were investigated. If a small amount of chiral dopant is utilised, a director rotation is induced into the liquid crystal network. When the rotation angle of the director is 90° or a multiple of 90° , the bilayer system exhibits a bending deformation. Otherwise, the bilayer system exhibits a curling deformation.

In conclusion, it is shown in this thesis that a surface relief structure can be created on fibres by photoembossing to obtain novel diffractive optical effects that are potentially useful in fashion design. Also, humidity responsive bilayer actuators are developed that are potentially useful in the breathable textile applications that adapt to humidity changes in the environment.

1 Introduction

1.1 An Overview of Smart Textiles

Traditionally, sources of raw materials for textiles were of animal protein in nature, such as the hairs from wool and the silk thread produced by the silk worm. Equally important were vegetable fibres from crops such as cotton and linen. In the last century, these fibres were overshadowed by man-made fibres based on cellulosic viscose, polyester, polypropylene and polyamides. Standard textile fabrics have properties which are set during fabric construction and that are maintained despite changes in ambient conditions and/or physical activity. These standard products are quite effective, especially when layered with other textile fabrics for synergistic effects and enhancement of comfort.

Smart textiles represent the next generation of fibres, fabrics and the articles produced from them.¹ A widely accepted definition states that smart textiles are materials and structures that can react or adapt to stimuli from the environment by integration of active functionalities.^{2,3} They are capable of showing a significant change in their mechanical properties, colour, shape, or their optical, electromagnetic, or thermal properties in response to the stimuli.² The stimulus can be of an electrical, thermal, chemical, magnetic or other origin.²⁻⁵ Moreover, the term “smart” is frequently used parallel to the other ones like “intelligent” or “adaptive”.⁴ This new generation of "smart textiles" are often high-tech products with a high added value. It makes considerable new demands on the innovative ability within academia and industry, which also offer huge potential for future

new applications.

Smart textiles can be divided into three subgroups based on their functions:^{2,3}

- 1) Passive smart textiles are textiles that can only sense the environment. They are sensors.
- 2) Active smart textiles are textiles that can sense and respond to stimuli from the environment. They are both sensors and actuators.
- 3) Adaptive smart textiles are textiles that can sense, respond and adapt to the stimuli from the environment.

Current smart textiles are utilised in different fields that can be divided by application area: fashion, sports, medical and military.⁵⁻¹⁶

Many of the innovations in smart textiles in the past years started with military applications, e.g. fragment and bullet resistant body armour and chemical agent protective clothing.^{6-9, 17} Usually these smart textiles for military applications show capabilities such as: sensing and responding, power and data transmission, transmitting and receiving radio frequency (RF) signals, self-repairing materials, automatic voice warning systems of dangers, monitoring near skin temperature, exterior temperature and toxic levels.¹⁷ Sometimes, these smart textiles are also utilised for civilian personnel engaged in high-risk activities to provide the most effective survivability.¹⁷

Smart textiles used in the medical and applied healthcare and hygiene sectors are important and become an growing part of the textile industry.¹¹ The application of smart textiles in medical and healthcare products can be categorised into: biocompatible implants and tissues, biosensors, antibacterial wound treatment materials, prosthetics, and medical wear for monitoring body temperature and humidity.¹¹ For example, wearable electronics and smart textiles can be utilised for a medical application, i.e. the continuous and long-term monitoring of electrocardiogram and respiration rate of children in a hospital environment.¹³ As the first-ever commercial wireless, biosensor baby pyjama,

Exmobaby is specifically designed for newborns and infants to monitor ECG, skin temperature and movement and it can transmit alerts to a PC or smart phone.¹⁶

Smart textiles in fashion are also becoming more important. Recently there have been rapid developments in clothing with electronic systems incorporated into the fibres, fabrics and the prints applied to garments.¹⁸ For instance, the CuteCircuit Galaxy Dress shows the fashion possibilities of integrating electronic systems into textiles. The dress provides a spectacular effect with 24,000 full-colour LEDs integrated into layers of silk. It is the largest wearable display in the world.¹²

Compared to other applications, smart textiles for the entertainment market are still not mature. For the time being, smart textiles for entertainment are prototypes such as textiles with built-in MP3 player controller.⁵ Most of the commercial products are based on the Fibretronic Embedded Textile Device.⁵ The devices are set in forms of a keypad or joystick integrated in the garment and a controller module connecting the garment to a range of personal electronics such as iPod, iPhone, MP3 players and smart phone.^{5, 14} Based on it, they allow the operation of personal electronics from our garment.

Smart textiles as a new generation of textiles are expected to interact with the environment. In this thesis, fibres as the units of smart textiles will be discussed with respect to two aspects: new visual perception and responsiveness to external triggers.

1.2 Appearance of Textile Fibres

Traditionally, chemical dyes and pigments are used to produce colours in textile fibres which are based on absorption of light.¹⁹ These conventional fibres usually have a smooth surface and appear to have a single, angular-independent colour. To satisfy people's diversified taste and increasing demands on the perception of

textiles by fashion designers, it becomes a challenge to make new visual effects in textile fibres.

In nature, colours mostly come from the inherent colours of the materials based on spectral absorption, but it sometimes has a purely non-absorbing origin, such as diffraction or interference of the light. The latter is called “structural colours” or “iridescence”.²⁰⁻²³ Structural colours differ considerably from the ordinary coloration mechanisms in pigments, dyes and metals. It can’t be mimicked by chemical dyes or pigments. Furthermore, structural colour is free from photobleaching, unlike traditional dyes or pigments.²⁴ The brilliant blue colour of the wing of the *Morpho* Butterflies from South America is one of the most representative examples from nature possessing so-called structural colour. The colour in *Morpho* butterfly originates from the submicron structure covering the *Morpho*'s wings, as shown in Fig. 1.1.²¹⁻²³

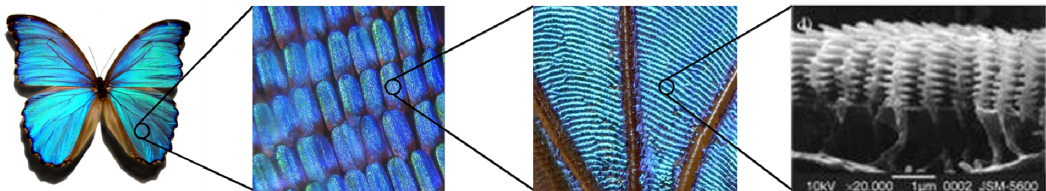


Figure 1.1: Images of *Morpho* Butterfly and wing-scale structure.²⁴

Structural colouration has potential for textile application with biomimetic surfaces that could provide brilliant colours and adaptive camouflage. Previously, the Japanese company Teijin Limited developed Morphotex fibres which are named after the *Morpho* butterfly.²⁵ The cross section of these fibres consists of alternate layers with different refractive indexes. By accurately controlling the thickness of the layers, different colours are generated based on the diffraction of light.²⁵⁻²⁷

In this thesis, we aim to get angular-dependent visual effect on fibres based on the diffraction of light, which can be simply produced by making diffractive structures on the surfaces of fibres. There are several techniques that can be

applied to create structures on the surface of fibres. The most relevant techniques are described in the following sections.

1.2.1 Specific die design

Specific die designs are used during spinning processes to generate micro-structured fibres with different shapes.^{28, 29} However, this technology has two disadvantages. First, the surface structuring occurs only in a single dimension, i.e. along the fibre length. Secondly, the fineness of the fibre relief surface (height/pitch of the relief structure) is related to the fabrication fidelity of the spinning dies, the surface tension and the viscosity of the spinning dope.³⁰ The surface tension might cause the shape of fibres distorted from the original spinneret die design.³¹ High viscosity of the polymer melt results in coarser fibres.³²

1.2.2 Mechanical embossing

The accurate nano- and/or micro-structuring of textile fibres remains an issue especially if relief structures perpendicular to the fibre axis are desired. In fact, at the moment this is mostly achieved via mechanical embossing of fibres.^{30, 33, 34} Schiff et al. introduced the surface structuring of textile fibres using roll embossing.³⁰ In this process, the fibres were guided through a gap between two cylinders and one of the cylinders was micro-structured and the other opposite was smooth and heated with a hot-air fan. This roll embossing allows fibres to be laterally structured.³⁰ However, it was found that fibres deformed during mechanical embossing and also that the structuring of the fibres was restricted within a very confined area.³⁰ For the time being, this method is difficult to apply to multifilament yarns and is hard to implement in a high-speed and continuous spinning line.

1.2.3 Photoembossing

Photoembossing is a promising new technique that was recently developed to produce relief structures in thin films that are deposited on polymeric or glass substrates.³⁵⁻⁴³ The typical photoembossing process is a simple procedure as shown in Fig. 1.2. Usually, it utilises a photopolymer mixture consisting of a polymeric binder, a multifunctional monomer, a photoinitiator and a retarder/inhibitor, which is applied from solution to form a transparent solid thin film on the substrate. Typically linear thermoplastic polymers like poly(benzyl methacrylate) or poly(methyl methacrylate) are used as polymeric binder.⁴⁴ Multifunctional monomers with more than two reactive acrylate groups like dipentaerythritol penta/hexa-acrylate are used as reactive species and a retarder/inhibitor like tert-butyl hydroquinone (TBHQ), tetra-fluorohydroquinone (TFHQ) or trimethyl hydroquinone (TMHQ) are utilised.³⁸⁻⁴² A patterned UV exposure is first applied to the photopolymer film using a mask (see Fig. 1.2). The photoinitiator is activated and generates free radicals in the exposed areas. The polymerisation of monomers in the exposed area is inhibited by the glassy state of the photopolymer mixture at room temperature. After exposure, the sample is heated above the glass transition temperature to increase mobility and to start the polymerisation of monomer, which causes a reaction driven diffusion of reactive species to the exposed area.³⁷ This mass transport creates a local volume increase and a corresponding relief structure on the surface of film. Subsequently, a flood exposure step is applied to completely polymerise the relief structure. Various processing parameters were identified that influence the height and shape of the final relief structure, which determine its performance in specific applications.^{37, 41, 45, 46} These factors include UV exposure dose, exposure time, development temperature, photopolymer blend composition, film thickness and periods of the patterned photo-mask, which will be discussed in detail in Chapter 3.

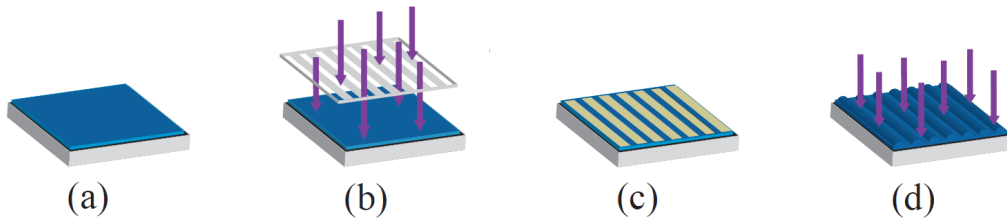


Figure 1.2: Schematic of typical photoembossing procedure: (a) Formation of film on a substrate, (b) Patterned UV exposure, (c) Thermal development and (d) Flood exposure.

Compared to other techniques, the main advantage of photoembossing is that it can be a very fast, cost-effective technique that generates nano- and/or micro-structures without etching procedures. Potentially its processing features facilitate incorporation of this process in a spinning line and also can be applied to multifilament yarns. In this thesis, the photoembossing will be utilised for the surface structuring of fibres.

1.3 Responsive Textile Fibres

Nature offers magic ways to protect living species against severe climate conditions. Many organisms are able to change their properties, such as their shape, in response to the changes in the environment, e.g. moisture and temperature. A common example in nature is the pine cone. The opening of the pine cones is associated with their moisture content. They are open when dry, facilitating the release of the cone's seed, and closed when wet.⁴⁷

To broaden the application of textiles, we also want to make responsive textiles that can interact with the user and/or environment. Previously, it was reported that adaptive garments could be produced that fit all sizes without tension and that recover to the original given size upon heating.⁴⁸⁻⁵⁰ This kind of smart garment is shape memory polyurethane (SMPU) knitted fabric that contains SMPU fibres and cotton fibres. The shape memory effect is controlled by the content of SMPU fibres.

Stimuli-responsive polymers are a class of materials that can mimic the responsive capabilities of natural systems and change properties upon changes in the environment. For instance, hydrogels that contain hydrophilic groups have a high affinity to water. Usually they exhibit dramatic volume change in response to an environmental change, such as temperature, pH, humidity, electric fields and light.⁵¹⁻⁵⁵ Interestingly, these responsive polyelectrolytes have been integrated into bilayer actuators showing humidity responsive bending resulting in a walking device.⁵⁶ Another class of interesting actuators are based on crosslinked liquid crystalline networks that also respond to the external stimuli with a mechanical deformation. Compared to the hydrogels, the liquid crystal polymer actuators can easily exhibit different kinds of deformations, such as contraction/expansion, bending motion, and even more complex anisotropic deformations giving spiral ribbons, helicoids, cone and anticone shapes.^{57, 58} This makes the liquid crystal polymer actuators potentially more attractive for the textile applications.

1.3.1 Liquid crystals

Liquid crystals (LC) are a state of matter that has properties between a conventional liquid and a solid crystal. The liquid crystals have a distinguishing state between the traditional solid and liquid phases. LC molecules (mesogens) are typically rod- or disc-like and tend to point along a common axis which is called the director. LCs can be divided into thermotropic and lyotropic liquid crystals. In this thesis, we will focus on thermotropic LCs that exhibit a phase transition into the LC phase as temperature is changed.

Many thermotropic LCs exhibit various phases within the liquid crystal state, such as smectic and nematic phases that can be distinguished by positional order and orientation order (see Fig. 1.3). In this thesis, the LCs will be used in the nematic phase where the molecules have no positional order but align to have long-range directional order with their long axis roughly parallel and therefore

mono-domain orientation is relatively easy to achieve.⁵⁹

In the nematic phase, the molecules are aligned with respect to the director, \bar{n} , as depicted in Fig. 1.3. The orientation order of the nematic phase is quantified by the order parameter S (equation 1.1), which is a function of the angle θ , where θ is the angle between the director and long axis of the molecules.

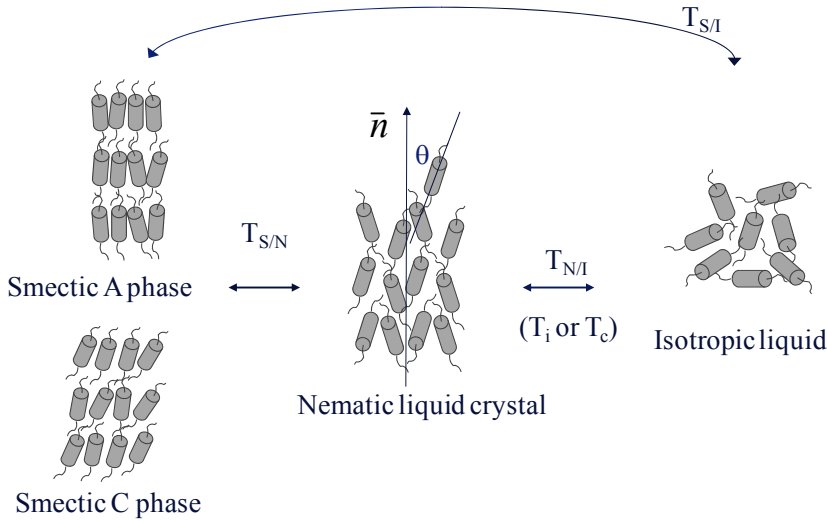


Figure 1.3: Types of LC phases, which can be induced upon a change of temperature.

$$S = \left\langle \frac{3 \cos^2 \theta - 1}{2} \right\rangle \quad (1.1)$$

When the molecules are randomly aligned in the isotropic state, S is zero, whereas $S=1$ denotes a perfect crystal structure or an ideal orientation order. Typically the order parameter of a nematic phase LC has values between 0.4 to 0.8.

Liquid crystals are used in a variety of applications because external perturbation can cause significant changes in the macroscopic properties of LC systems through aligning the molecules. There are several ways to induce alignment in liquid crystals. An external field, such as electrical field,⁶⁰ magnetic field,⁶¹ or shear-flow mechanical field,⁶² can be used to induce these changes because of the anisotropic properties of the molecules. Also specific surface

treatments can be used to force the director to point in a specific direction. For example, a thin polymer coating (usually a polyimide) that is spread on the glass slides and rubbed in a single direction with a cloth will align liquid crystal molecules in the rubbing direction, based on the combined action of sterical and dispersive interactions.

1.3.2 Liquid crystal polymer actuator

Liquid crystal polymers (LCP) are polymers that can exhibit liquid crystallinity. As shown in Fig. 1.4, liquid crystal polymers can be distinguished into three groups: LC main chain polymers where the LC units are head-to-tail connected to the polymer backbone; LC side chain polymers having LC side groups on the polymer backbone; LC networks which are densely crosslinked polymers and the LC units are linked on both sides to the polymer backbone. In this thesis, LC networks created by photopolymerisation are predominantly used because the polymerisation temperature can be chosen as desired within the LC phases and premature polymerisation can be avoided before the desirable LC molecular order is established, which usually occurs in thermal polymerisation.

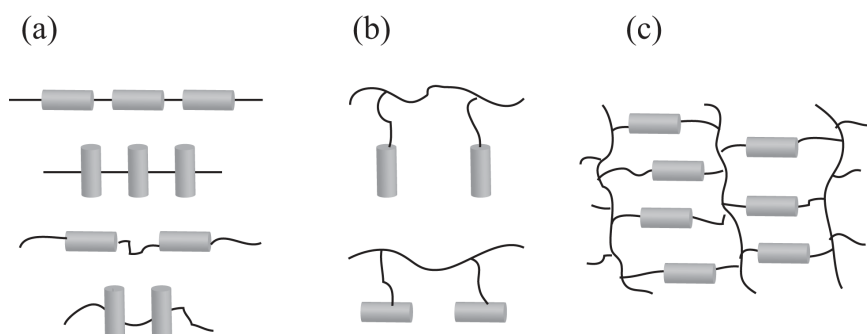


Figure 1.4: Different liquid crystal polymer structures: (a) LC main chain polymer, (b) LC side chain polymer, and (c) LC polymer network.

The liquid crystal networks (LCNs) can be fabricated by a single-step polymerisation of LC monomers that contain more than one polymerisable group. Un-reacted low-molecular-mass LC mesogens allow the alignment of molecules

using different techniques as mentioned above. The order will be preserved during and after the photopolymerisation. The polymerised LC networks have a high crosslink density that results in a limited mobility for the LC units in these systems. As a consequence, the nematic-isotropic transition temperature is often not observed and the systems remain nematic upon heating to elevated temperatures.⁶³

The traditional driving trigger for the LC polymer actuators is heat. The temperature changes result in thermal expansion/contraction in the LC polymer actuators. When adding additional functional moieties to reactive mesogens, such as light-responsive azo moieties, LC polymer actuators can respond to light.⁶⁴⁻⁷⁶ By controlling the wavelength, the polarisation state, intensity of light and the alignment of the LC, the deformation of the LC polymer actuators can be controlled. For instance, the deformation direction can be controlled by using polarized light because of the dichroic properties of the azobenzene moieties.⁷⁷ There is another class of actuators that are sensitive to pH, humidity, and other chemical species.⁷⁸⁻⁸⁴ These agent-sensitive actuators are formed based on liquid crystal networks consisting of both covalent and secondary (hydrogen) bonds. The secondary bonds, such as hydrogen bonds, can be reversibly broken upon the action of an agent. Previously, Harris et al. applied a hydrogen-bond-based dimerisation of benzoic acid to form nematic liquid crystal acrylate monomers.⁷⁸⁻⁸⁰ The monomers are copolymerised with fully covalent diacrylate monomers to get mechanical integrity. After the formation of the polymer network, a controlled and reversible rupture of the hydrogen bonds can be initiated, which requires a reaction with a base. Under alkaline conditions, the network is converted into a polymer salt that retains less nematic order, resulting in a macroscopic, pH-induced deformation. Exposure to acids restores the hydrogen-bonded diacid and the original dimensions.⁷⁸⁻⁸⁰

LC polymer actuators can exhibit different mechanical deformations, such as

expansion, contraction, bending, or curling, in response to the external stimuli. The nature of the deformation depends on the alignment and molecular order of the LC units in all three dimensions in the polymer network.⁸⁵ Examples of molecular orientation profiles and their response upon a change of the order parameter are shown in Fig. 1.5.

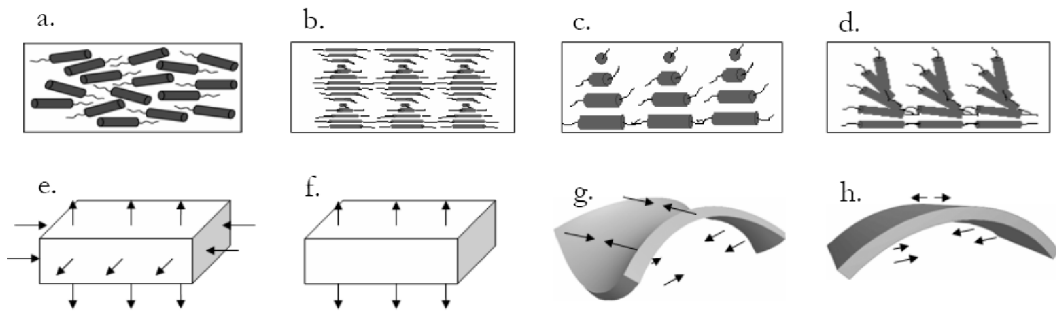


Figure 1.5: Schematic representation of various molecular orientation profile, planar uniaxial (a), cholesteric (b), twisted nematic (c) and splay (d), with the corresponding deformations (e-h) upon a decrease of molecular order.⁸⁶

Among them, the most interesting actuation modes are the splayed and twisted nematic configurations that can result in a mechanical bending/curling deformation. A simple example is given in Fig. 1.6. The molecules are aligned in a so-called splayed configuration with their long axis planar to the surface on one side and perpendicular to the surface on the opposite side. Upon heating, the decrease of the order parameter leads to the contraction of the surface with planar alignment and expansion of the opposite surface with perpendicular alignment. This results in a bending deformation.⁸⁷

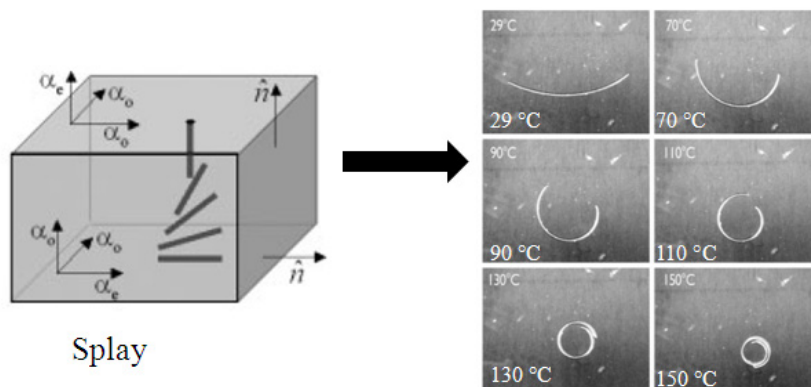


Figure 1.6: Temperature-induced deformation of a LC polymer actuator with a splayed configuration.⁸⁷

The material demonstrated in Fig. 1.7 shows a light-induced deformation. In this case, there are azobenzene groups in the system and a so-called twisted-nematic (TN) alignment is fabricated where the mesogenic units are oriented in the plane of the film but rotate over 90° . Upon UV illumination, the azobenzene units undergo a trans-cis isomerisation, which results in film contraction along the director and expansion in the perpendicular direction. When the film is cut at 90° or 0° to the alignment direction of the surface, it exhibits a bending deformation. When the film is cut at 45° to the alignment direction of the surface, it shows a curling deformation.⁶⁹ Selinger et al. also made temperature-induced LC polymer actuators that are based on TN alignment. Thermal-responsive curling deformation with a handedness change was observed when the film was cut at 45° to the alignment direction of the surface of the sample. More importantly, the materials gave different type of shapes, such as helicoids and spiral ribbons, dependent on the geometry of the samples, i.e. the width to thickness ratio, as shown in Fig. 1.8.⁵⁸

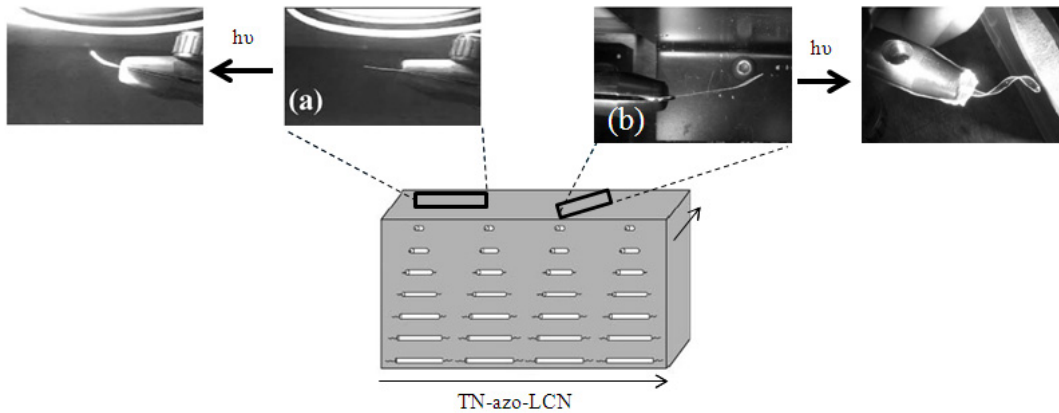


Figure 1.7: Light-induced deformation of a TN film cut at (a) $0^\circ/90^\circ$ and (b) 45° with the alignment direction of the surface.⁶⁹

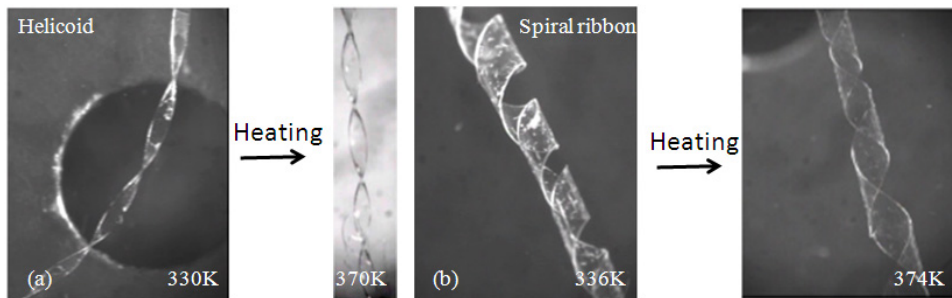


Figure 1.8: Thermal responsive deformation of helicoids (a) and spiral ribbons (b) formed from a TN film.⁵⁸

1.4 Motivation and Objective of the Thesis

The project is aimed at the creation of new functionalities into textile fibres, woven and non-woven fabrics to generate specific properties for a broad range of potential applications.

The first part of this thesis aims to change the visual perception of the textiles. A promising new technique, i.e. photoembossing, will be utilised to create micro-/nano- surface structures on fibres so that new visual effects for fibres can be obtained based on the diffraction of visual light. New materials and processes are developed to open the possibility to produce nano- and/or micro-structured fibres

in high-speed spinning lines.

Simultaneously, it is intended to develop responsive fibres based on liquid crystalline networks that respond to external stimuli such as humidity and/or temperature. Here, the prime objective is to develop fibres that respond to environmental conditions via bending and/or curling (or visa versa). In a fabric, it is expected that such deformations of the fibres can change the water vapour transmission rate in a response to autonomous triggers humidity and/or temperature.

1.5 Organisation and Scope of the Thesis

In this thesis, two different functionalities, i.e. new visual perception and responsiveness to external triggers, will be created into the textile fibres.

Chapters 2-5 focus on the visual perception of the textile fibres. In Chapter 2 a model to describe the diffractive properties of surface relief structures is explored. It is attempted to predict the desirable grating pitch and relief height of surface relief structures from a theoretical viewpoint with emphasis on angular-dependent diffractive visual effects. The prime objective is to use photoembossing to create the desired surface relief structures. Chapter 3 describes the photoembossing via photo-mask exposure. A new photopolymer system is explored to improve the surface relief structures with respect to the relief height in comparison to a conventional photopolymer system. In Chapter 4, photoembossing with pulsed laser interference holography is investigated and the possibility of combining this process with moving substrates is explored to design a process that potentially can be incorporated in a high-speed spinning line. Moreover, the photoembossing of polymer-monomer mixtures at elevated temperature is described to further enhance the relief height and reduce the optimum exposure energy. Chapter 5 first investigates whether the photopolymer mixture can be directly spun into fibres and embossed. Also bi-component fibre systems consisting of core fibre and

photopolymer coating are investigated to enhance fibre properties and to integrate photoembossing in more or less conventional spinning lines.

Chapters 6 and 7 focus on the responsive fibres that exhibit shape deformation in response to external triggers. Special emphasis is devoted to stimuli, which are already present in the environment such as (changes in) humidity to obtain smart fibres and/or fabrics without the need for electrical fields. A LC network having hydrogen bonded entities, which, after activation with an alkaline solution, exhibits humidity responsive deformation is utilised. Here, a bilayer system is investigated, which consists of an oriented polymer substrate (PA-6) and a LC coating. The uniaxially stretched polymer film is utilised to induce the alignment in the liquid crystal network. A splay-aligned LC network was first generated on the surface of oriented substrate that induces a bending deformation into the bilayer system (Chapter 6). Furthermore, a chiral dopant is utilised to induce a director rotation in the LC network, and the corresponding bending or curling deformation of the bilayer actuator is investigated in Chapter 7.

In the last chapter, the assessment of the technologies described in the thesis is presented and also recommendations for the future research are given.

1.6 References

1. R. Hibbert, *Textile Innovation: Interactive, Contemporary and Traditional Materials*, Line, London, UK, 2004.
2. H. H. Dadi, University of Borås, Sweden, 2010.
3. L. van Langenhove and C. Hertleer, *Int J Cloth Sci Tech*, 2004, **16**, 63-72.
4. A. Boczkowska and M. Leonowicz, *Fibres & Textiles East. Eur.*, 2006, **14**, 13-17.
5. M. Suh, K. Carroll and N. Cassill, *J Text Apparel Technol Manage*, 2010, **6**, 1-18.

6. P. Smith, P. J. Lemstra and H. C. Booij, *J Polym Sci Part B: Polym Phys*, 1981, **19**, 877-888.
7. P. Smith and P. J. Lemstra, US Patent 4430383, 1984.
8. P. Smith and P. J. Lemstra, US Patent 4422993, 1983.
9. P. Smith and P. J. Lemstra, US Patent 4344908, 1982.
10. S. L. Kwolek, P. W. Morgan, J. R. Schaeffgen and L. W. Gulrich, *Macromolecules*, 1977, **10**, 1390-1396.
11. R. Czajka, *Fibres & Textiles East. Eur.*, 2005, **13**, 13-15.
12. CuteCircuit, <http://www.cutecircuit.com>.
13. M. Catrysse, R. Puers, C. Hertleer, L. Van Langenhove, H. van Egmond and D. Matthys, *Sensors Actuat A-Phys*, 2004, **114**, 302-311.
14. Fibretronic Limited, <http://fibretronic.com/>.
15. International Fashion Machines, <http://www.ifmachines.com>.
16. Exmovere Holdings, Inc., <http://exmobaby.exmovere.com/>.
17. X. Tao, *Smart Fibres, Fabrics, and Clothing*, Woodhead, 2001.
18. R. R. Mather, *Rev Prog Color*, 2001, **31**, 36.
19. E. S. B. Ferreira, A. N. Hulme, H. McNab and A. Quye, *Chem Soc Rev*, 2004, **33**, 329-336.
20. S. Kinoshita and S. Yoshioka, *Sen-I Gakkaishi*, 2003, **59**, 35-39.
21. S. Kinoshita and S. Yoshioka, *Chem Phys Chem*, 2005, **6**, 1442-1459.
22. S. Kinoshita, S. Yoshioka and K. Kawagoe, *Proc R Soc B: Bioll Sci*, 2002, **269**, 1417-1421.
23. S. Kinoshita, S. Yoshioka and J. Miyazaki, *Rep Prog Phys*, 2008, **71**, 076401.
24. H. Kim, J. P. Ge, J. Kim, S. Choi, H. Lee, H. Lee, W. Park, Y. Yin and S. Kwon, *Nat Photonics*, 2009, **3**, 534-540.
25. M. Yokohama, T. Osaka, S. Kanagawa, A. Kanagawa, K. Kanagawa and H. Yokohama, US Patent 6326094B1, 2001.
26. K. Yokosuka, H. Yokohama and J. Yokosuka, US Patent 5472798, 1995.
27. S. Aichi, T. Osaka, S. Kanagawa, A. Kanagawa, K. Kanagawa, M. Osaka and H. Yokohama, US Patent 6243521B1, 2001.

28. W. Nijdam, J. de Jong, C. J. M. van Rijn, T. Visser, L. Versteeg, G. Kapantaidakis, G. H. Koops and M. Wessling, *J Membr Sci*, 2005, **256**, 209-215.
29. P. Z. Culfaz, E. Rolevink, C. van Rijn, R. G. H. Lammertink and M. Wessling, *J Membr Sci*, 2010, **347**, 32-41.
30. H. Schiff, M. Halbeisen, U. Schutz, B. Delahoche, K. Vogelsang and J. Gobrecht, *Microelectron Eng*, 2006, **83**, 855-858.
31. M. Ahmed, *Textile Science and Technology: Polypropylene Fibers-Science and Technology*, Elsevier Scientific Publishing Company, New York, 1982.
32. N. Ogata, G. Lu, T. Iwata, S. Yamaguchi, K. Nakane and T. Ogihara, *J Appl Polym Sci*, 2007, **104**, 1368-1375.
33. M. Halbeisen and H. Schiff, *Chem Fibres Int*, 2004, **54**, 378-379.
34. W. J. Shi and P. H. Zhang, *Melliand China*, 2008, **3**, 28-33.
35. F. T. O'Neill, I. C. Rowsome, A. J. Carr, S. M. Daniels, M. R. Gleeson, J. V. Kelly, J. R. Lawrence and J. T. Sheridan, *Opto-Ireland 2005: Photonic Engineering*, 2005, **5827**, 445-456.
36. A. Liedtke, C. H. Lei, M. O'Neill, P. E. Dyer, S. P. Kitney and S. M. Kelly, *Acs Nano*, 2010, **4**, 3248-3253.
37. C. Sanchez, B. J. de Gans, D. Kozodaev, A. Alexeev, M. J. Escuti, C. van Heesch, T. Bel, U. S. Schubert, C. W. M. Bastiaansen and D. J. Broer, *Adv Mater*, 2005, **17**, 2567-2571.
38. N. Adams, B. J. de Gans, D. Kozodaev, C. Sanchez, C. W. M. Bastiaansen, D. J. Broer and U. S. Schubert, *J Comb Chem* 2006, **8**, 184-191.
39. K. Hermans, C. W. M. Bastiaansen, D. J. Broer and J. Perelaer, Int. Pat., WO 2008025508, 2008.
40. K. Hermans, M. van Delden, C. W. M. Bastiaansen and D. J. Broer, *J Micromech Microeng*, 2008, **18**, 095022.
41. K. Hermans, F. K. Wolf, J. Perelaer, R. A. J. Janssen, U. S. Schubert, C. W. M. Bastiaansen and D. J. Broer, *Appl Phys Lett*, 2007, **91**, 174103.
42. B. J. de Gans, C. Sanchez, D. Kozodaev, D. Wouters, A. Alexeev, M. J. Escuti, C. W. M. Bastiaansen, D. J. Broer and U. S. Schubert, *J Comb Chem*, 2006, **8**, 228-236.

43. S. Liu, M. R. Gleeson, J. X. Guo and J. T. Sheridan, *Macromolecules*, 2010, **43**, 9462-9472.
44. S. Piazzolla and B. K. Jenkins, *Opt Lett*, 1996, **21**, 1075-1077.
45. K. Hermans, S. Z. Harnidi, A. B. Spoelstra, C. W. M. Bastiaansen and D. J. Broer, *App Opt*, 2008, **47**, 6512-6517.
46. K. Hermans, I. Tomatsu, M. Matecki, R. P. Sijbesma, C. W. M. Bastiaansen and D. J. Broer, *Macromol Chem Physic*, 2008, **209**, 2094-2099.
47. C. Dawson, J. F. V. Vincent and A. M. Rocca, *Nature*, 1997, **390**, 668-668.
48. J. L. Hu, Y. Zhu, H. H. Huang and J. Lu, *Prog Polym Sci*, 2012, **37**, 1720-1763.
49. J. L. Hu and S. J. Chen, *J Mater Chem*, 2010, **20**, 3346-3355.
50. Y. Liu, A. Chung, J. L. Hu and J. Lv, *J Zhejiang Univ-Sc A*, 2007, **8**, 830-834.
51. G. P. Chen, Y. Imanishi and Y. Ito, *Langmuir*, 1998, **14**, 6610-6612.
52. H. Tokuyama and T. Iwama, *Langmuir*, 2007, **23**, 13104-13108.
53. K. Sumaru, K. Ohi, T. Takagi, T. Kanamori and T. Shinbo, *Langmuir*, 2006, **22**, 4353-4356.
54. D. Kuckling, *Colloid Polym Sci*, 2009, **287**, 881-891.
55. Z. B. Hu, X. M. Zhang and Y. Li, *Science*, 1995, **269**, 525-527.
56. Y. Ma, Y. Y. Zhang, B. S. Wu, W. P. Sun, Z. G. Li and J. Q. Sun, *Angew Chem Int Ed*, 2011, **50**, 6254-6257.
57. L. T. de Haan, C. Sanchez-Somolinos, C. M. W. Bastiaansen, A. P. H. J. Schenning and D. J. Broer, *Angew Chem Int Ed*, 2012, **51**, 12469-12472.
58. Y. Sawa, F. F. Ye, K. Urayama, T. Takigawa, V. Gimenez-Pinto, R. L. B. Selinger and J. V. Selinger, *Proc Nat Acad Sci USA*, 2011, **108**, 6364-6368.
59. C. W. Oseen, *Trans Faraday Soc*, 1933, **29**, 883-899.
60. R. Barberi, F. Ciuchi, G. E. Durand, M. Iovane, D. Sikharulidze, A. M. Sonnet and E. G. Virga, *Eur Phys J E*, 2004, **13**, 61-71.
61. M. I. Boamfa, S. V. Lazarenko, E. C. M. Vermolen, A. Kirilyuk and T. Rasing, *Adv Mater*, 2005, **17**, 610-614.
62. M. G. Forest, X. Y. Zheng, R. H. Zhou, Q. Wang and R. Lipton, *Adv Funct Mater*, 2005, **15**, 2029-2035.

63. D. J. Broer, *Polymerisation Mechanisms*, Elsevier Applied Science, London and New York, Ch.12, 1993.
64. D. Corbett, C. L. van Oosten and M. Warner, *Phys Rev A*, 2008, **78**, 013823.
65. C. D. Modes, M. Warner, C. L. van Oosten and D. Corbett, *Phys Rev E*, 2010, **82**, 041111.
66. C. L. van Oosten, C. W. M. Bastiaansen and D. J. Broer, *Nat Mater*, 2009, **8**, 677-682.
67. C. L. van Oosten, D. Corbett, D. Davies, M. Warner, C. W. M. Bastiaansen and D. J. Broer, *Macromolecules*, 2008, **41**, 8592-8596.
68. C. L. van Oosten, K. D. Harris, C. W. M. Bastiaansen and D. J. Broer, *Eur Phys J E*, 2007, **23**, 329-336.
69. K. D. Harris, R. Cuypers, P. Scheibe, C. L. van Oosten, C. W. M. Bastiaansen, J. Lub and D. J. Broer, *J Mater Chem*, 2005, **15**, 5043-5048.
70. Y. L. Yu, M. Nakano, T. Maeda, M. Kondo and T. Ikeda, *Mol Crystals Liq Crystals*, 2005, **436**, 1235-1244.
71. Y. L. Yu, M. Nakano and T. Ikeda, *Pure Appl Chem*, 2004, **76**, 1467-1477.
72. Y. L. Yu, M. Nakano, A. Shishido, T. Shiono and T. Ikeda, *Chem Mater*, 2004, **16**, 1637-1643.
73. Y. L. Yu, M. Nakano and T. Ikeda, *J Syn Org Chem Jpn*, 2004, **62**, 471-479.
74. K. M. Lee, M. L. Smith, H. Koerner, N. Tabiryan, R. A. Vaia, T. J. Bunning and T. J. White, *Adv Funct Mater*, 2011, **21**, 2913-2918.
75. T. J. White, S. V. Serak, N. V. Tabiryan, R. A. Vaia and T. J. Bunning, *J Mater Chem*, 2009, **19**, 1080-1085.
76. T. J. White, N. V. Tabiryan, S. V. Serak, U. A. Hrozhyk, V. P. Tondiglia, H. Koerner, R. A. Vaia and T. J. Bunning, *Soft Matter*, 2008, **4**, 1796-1798.
77. Y. L. Yu, M. Nakano and T. Ikeda, *Nature*, 2003, **425**, 145-145.
78. K. D. Harris, C. W. M. Bastiaansen and D. J. Broer, *Macrom Rapid Comm*, 2006, **27**, 1323-1329.
79. K. D. Harris, C. W. M. Bastiaansen and D. J. Broer, *J Microelectromech Syst*, 2007, **16**, 480-488.

80. K. D. Harris, C. W. M. Bastiaansen, J. Lub and D. J. Broer, *Nano Lett*, 2005, **5**, 1857-1860.
81. H. Kihara, T. Kato, T. Uryu and J. M. J. Frechet, *Chem Mater*, 1996, **8**, 961-968.
82. T. Kato, N. Mizoshita and K. Kanie, *Macromol Rapid Comm*, 2001, **22**, 797-814.
83. T. Kato, N. Mizoshita and K. Kishimoto, *Angew Chem Int Ed*, 2006, **45**, 38-68.
84. T. Kato, T. Yasuda, K. Kanie, O. Ihata, N. Mizoshita, K. Hanabusa, M. Ukon and Y. Shimizu, *Abstr Pap Am Chem S*, 1999, **218**, U484-U484.
85. D. J. Broer, C. L. van Oosten, K. D. Harris, C. W. M. Bastiaansen, J. Lub and M. C. Luengo Gonzalez, Liquid crystal networks and self-organizing hydrogels: nanotechnology towards soft actuators and nanoporous systems, <http://www.sbpmat.org.br/icam2009dir/submission/palestrante/arquivos/PP2.pdf>
86. C. L. van Oosten, PhD thesis, Eindhoven University of Technology, 2009.
87. G. N. Mol, K. D. Harris, C. W. M. Bastiaansen and D. J. Broer, *Adv Funct Mater*, 2005, **15**, 1155-1159.

2 Modelling of Diffraction Gratings

2.1 Introduction

The first effect that we want to realise in this thesis is an angular-dependent visual effect on fibres based on diffraction of light. This can be realised by making periodic structures, e.g. diffraction gratings, on the surface of fibres.¹ A diffraction grating is a repetitive array of closely spaced elements which can split light into several beams travelling in different directions.² A common form of the diffraction gratings is a series of parallel small stripes or ridges on a surface, which is called surface relief grating.³⁻⁷ Such surface relief gratings can be either transmissive or reflective.⁸⁻¹⁰ This chapter provides the theoretical framework for the design of surface relief gratings to obtain the desired angular-dependent visual effects based on diffraction of light. The two most important aspects are the angle of diffraction and diffraction efficiency. These are explored from a theoretical viewpoint with an emphasis on the pitch and the height of the surface-relief grating.

2.2 Angular Dispersion

A beam of white light incident on a grating can be separated into its component colours by diffraction, with each colour diffracted along a different direction (see Fig. 2.1). In general, this is governed by the grating equation.³ Light incident on a

grating is diffracted according to:

$$\Lambda(n_m \sin \theta_m - n_{in} \sin \theta_{in}) = m\lambda \quad (2.1)$$

where Λ is the grating period, λ is the wavelength, m indicates the order of diffraction, θ_{in} is the angle of incidence and θ_m is the angle of diffraction of the m^{th} order diffracted beam. n_{in} and n_m are the refractive indices of the media where the incident and diffracted beams propagate, respectively, and in our case are both equal to unity (n_{air}).

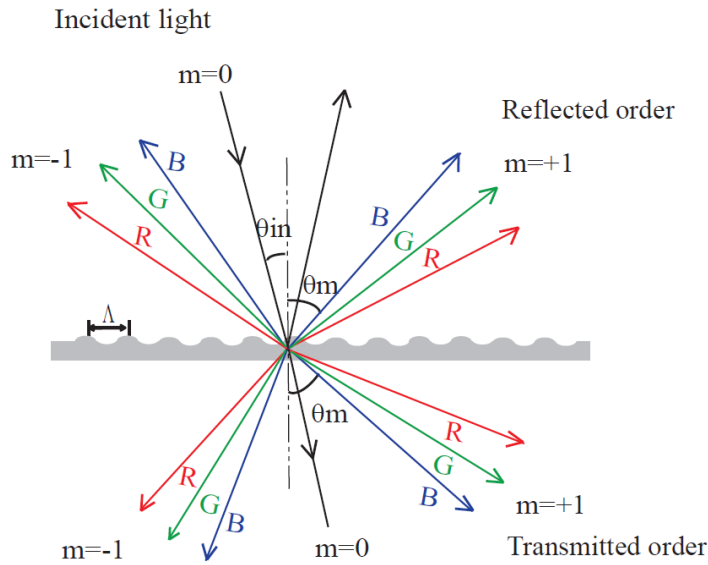


Figure 2.1: Sketch of a diffraction grating.

If white light encounters a grating, different colours are diffracted at different angles. The change in the diffraction angle per unit wavelength, which is called the angular dispersion (D), can be expressed as:³

$$D = \frac{d\theta_m}{d\lambda} \quad (2.2)$$

Differentiating the grating equation (Eq. 2.1) and assuming that the angle of incidence (θ_{in}) is constant, yields:³

$$D = \frac{m}{\Lambda \cos \theta_m} \quad (2.3)$$

It clearly demonstrates that the angular dispersion in a given diffraction order increases as the grating period decreases. The grating period could be smaller than the incident wavelength, close to the incident wavelength or larger than the incident wavelength. However, when the grating period is smaller than the incident wavelength, no far-field diffraction occurs.³ Therefore, to get a strong angular dispersion, a small grating period should be chosen provided that the grating period is still larger than the incident wavelength.

2.3 Diffraction Efficiency

Diffraction efficiency and its variation with the grating height and angle of the incidence are important characteristics of a diffraction grating. The diffraction efficiency η_m of an order m can be defined as the ratio of the incident intensity (I_{in}) and the intensity of that order (I_m). For different colours to be more easily and clearly observable, high diffraction efficiencies are required. In general, the diffraction intensity cannot be analytically calculated. Rigorous Coupled-Wave Analysis (RCWA) is a relatively straightforward method for accurate analysis of grating structures. For a given incident field, RCWA calculates the electromagnetic fields after gratings by solving Maxwell's equations numerically. Subsequently, the intensities of various diffracted orders are obtained by analytically propagating the diffracted near field to the far field. The detailed implementation can be found in the publications from Moharam et al.¹¹⁻¹⁴

In this chapter, the commercially available software GSolver (Grating Solver Development Company),¹⁵ which is based on RCWA, was utilised to study the influence of the grating height on the diffraction efficiency of the surface relief grating. To simplify the whole system, two different grating periods are chosen to do the simulations, which are 8 μm and 1 μm , respectively. These two grating periods are larger than the wavelengths of the visual spectrum (approximately 400-700 nm). The outcome of the simulations provides the information on the

influence of the grating period on the diffraction efficiency, which will provide guidance for the grating design in the subsequent chapters.

2.3.1 Diffraction efficiency at normal incidence

The simulations assume that the gratings have a sinusoidal profile. The incident light is defined by specifying its wavelength ($\lambda=633$ nm) and the angle of incidence (θ). The incident field can be decomposed into s-polarisation and p-polarisation. Here, only s-polarised incident light is considered so that the calculated diffraction efficiency can be compared to the experimental data, which were measured with a low power s-polarised He-Ne laser at 633 nm, and are displayed in Chapter 4. For the simple case of normal incidence ($\theta=0^\circ$), the sum of resulting transmitted and reflected orders ($m\neq 0$) for the grating of 8 μm (dashed line) and 1 μm (solid line) are plotted in Fig. 2.2. The diffraction efficiency fluctuates upon changes in the relief height of the gratings for both transmitted and reflected orders. In the case of the transmitted orders (see Fig. 2.2a), the diffraction efficiency for both gratings of 8 μm (dashed line) and 1 μm (solid line) initially increases as the relief height increases. A maximum diffraction efficiency is achieved when the relief height is up to ~ 1.0 μm . Above that height, for the larger grating period (8 μm), the diffraction efficiency slightly oscillates around the maximum diffraction efficiency upon further increasing the relief height. For the smaller grating period (1 μm), the diffraction efficiency significantly changes as the relief height increases and another local maximum diffraction efficiency is obtained when the relief height is up to ~ 2.5 μm . For the reflected orders (see Fig. 2.2b), it is not surprising that the diffraction efficiency is much lower than that of the transmitted orders since transparent materials are assumed. Again, the diffraction efficiency initially is improved when the relief height increases, for both gratings of 8 μm (dashed line) and 1 μm (solid line). A maximum diffraction efficiency is obtained when the relief height is up to ~ 250 nm. After that, the

diffraction efficiency changes again as the relief height increases. Nevertheless, the results indicate that high diffraction efficiency can be obtained over a broader range of the relief height for the grating period of $8\ \mu\text{m}$ than for the grating period of $1\ \mu\text{m}$.

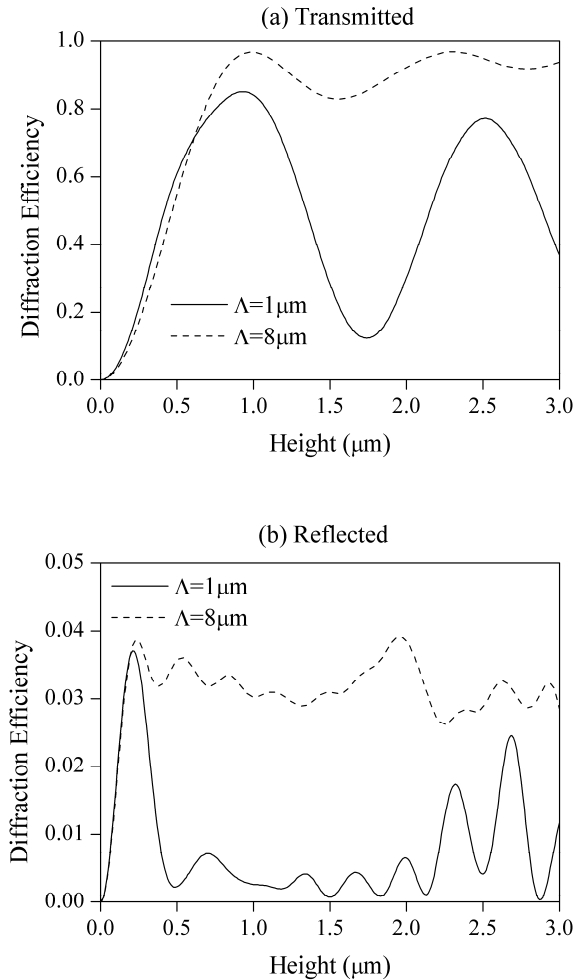


Figure 2.2: Calculated (RCWA) diffraction efficiency as a function of the grating height at normal incidence for a surface-relief grating ($n=1.49$) on glass ($n=1.5$): sinusoidal profile, $\lambda=633\ \text{nm}$. s -polarisation. (a) Sum of transmitted orders ($m \neq 0$). (b) Sum of reflected orders ($m \neq 0$).

2.3.2 Angular-dependent diffraction efficiency

In practical applications, there is not only normally incident light and light from

other directions needs to be taken into account. To study the angular dependence of a surface relief grating with a sinusoidal profile, we assumed in our model an incident wavelength $\lambda=633$ nm and that the incident light is linearly polarised (s- and p-polarised). The sum of the resulting diffraction efficiency ($m \neq 0$) for the grating of $8 \mu\text{m}$ and averaged over s- and p-polarisation is plotted in Fig. 2.3. The results demonstrate how the diffraction efficiency is dependent on both incident angle and relief height. In the case of the transmitted orders (see Fig. 2.3a), the diffraction efficiency initially increases to the maximum value upon increasing the relief height and then remains at a high value as the relief height further increases for a wide range of incident angles (0 - 80°). The diffraction efficiency is relatively insensitive to the incident angle. In the case of the reflected orders (see Fig. 2.3b), a maximum diffraction efficiency can be obtained when the relief height is within the range of ~ 0.5 to $\sim 1 \mu\text{m}$ and the incident angle approximately 60 - 70° .

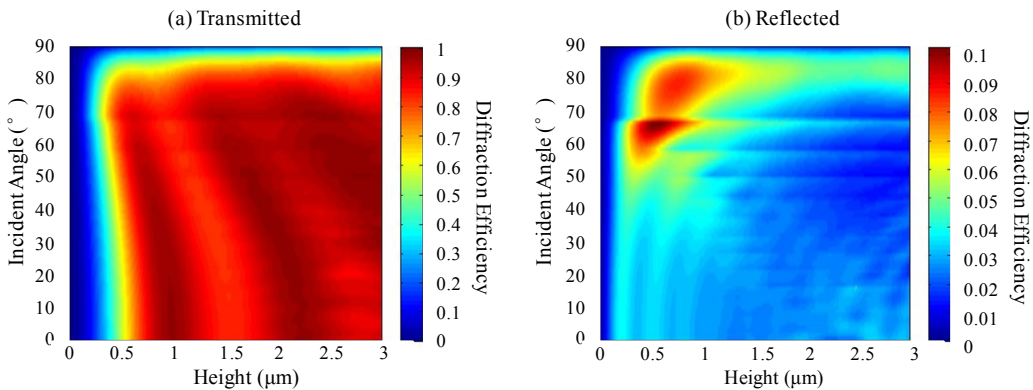


Figure 2.3: Calculated (RCWA) diffraction efficiency as a function of the grating height and incident angle for a surface-relief grating ($n=1.49$) on glass ($n=1.5$): sinusoidal profile, $A=8 \mu\text{m}$, $\lambda=633$ nm, averaged over s- and p-polarisation. (a) Sum of all transmitted orders ($m \neq 0$). (b) Sum of all reflected orders ($m \neq 0$). The colour in the plots represents the diffraction efficiency.

On the other hand, the sum of the resulting diffraction efficiencies ($m \neq 0$) for the grating of $1 \mu\text{m}$ is plotted in Fig. 2.4. Obviously, the diffraction efficiency does not only depend on the relief height. The incident angle has a strong influence on the diffraction efficiency. In the case of the transmitted orders (see

Fig. 2.4a), the diffraction efficiency initially increases as the relief height increases. After that, the diffraction efficiency fluctuates with increasing relief height and varying incident angle. A maximum diffraction efficiency is achieved when the relief height is approximately within 1.5-2 μm and the incident angle varies within 10-30°. In the case of the reflected orders, a relatively high diffraction efficiency is mostly observed at high incident angle. A maximum diffraction efficiency is obtained when the relief height is within 2.5-3 μm and the incident angle is up to 60-80°.

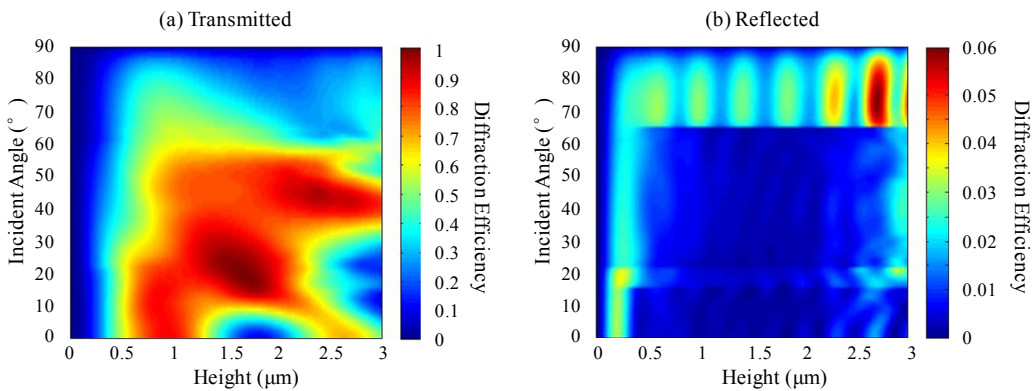


Figure 2.4: Calculated (RCWA) diffraction efficiency as a function of the grating height and incident angle for a surface-relief grating ($n=1.49$) on glass ($n=1.5$): sinusoidal profile, $\Lambda=1 \mu\text{m}$, $\lambda=633 \text{ nm}$, averaged over s - and p -polarisation. (a) Sum of all transmitted orders ($m \neq 0$). (b) Sum of all reflected orders ($m \neq 0$). The colour in the plots represents the diffraction efficiency.

Apparently, the diffraction efficiency of the small-size grating (1 μm) shows a larger dependence on the incident angle in comparison to the large-size grating (8 μm). More importantly, it is easier to maximise the diffraction efficiency for the large-size grating. In the case of the transmitted orders (see Fig. 2.3a and Fig. 2.4a), the maximum diffraction efficiency of the large-size grating (8 μm) can be achieved with a relatively low relief height ($\sim 1 \mu\text{m}$) for a wider range of the incident angles, while the diffraction efficiency of the small-size grating (1 μm) is obtained with a relatively high relief height ($\sim 1.5 \mu\text{m}$) and also within a smaller range of the incident angles. Again, in the case of the reflected orders (see Fig.

2.3b and 2.4b), a higher relief height ($\sim 2.5 \mu\text{m}$) is required for the small-size grating ($1 \mu\text{m}$) to maximise the diffraction efficiency in comparison to the lower relief height ($\sim 0.5 \mu\text{m}$) required for the large-size grating ($8 \mu\text{m}$). Remarkably, the diffraction efficiency of the gratings is shape-selective.¹⁶ These calculations are based on the assumption that the gratings have a sinusoidal profile.

2.4 Gratings on Curved Surfaces

Above-mentioned theoretical calculations are all based on a flat geometry. In this thesis, such surface relief gratings will be fabricated on the fibres that have highly curved geometries. Considering that, a beam of light incidence encounters the fibre surface might have different incident angles at different spots. Fig. 2.5 explains the situation in this specific condition. The incident angle (θ_{in}) of the incoming light with respect to the normal of fibre surface is expected to increase from the middle (spot A) of the fibre towards the edges (spot B) of the fibre, which causes the change of diffraction efficiency. However, the incoming light encountering the edges of fibre will still be diffracted into different directions by the grating. The fibres with such surface-relief gratings can exhibit angular-dependent visual effect as well. The next step is to fabricate surface gratings with an optimised grating pitch and relief height on fibres. How to and whether it is possible to make such surface gratings will be discussed in the following chapters.

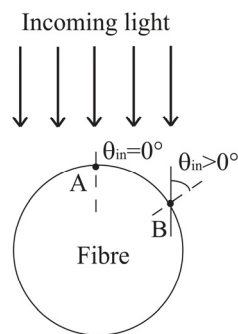


Figure 2.5: Illustration of the cross section of fibre normal to the incidence ($\theta_{in}=0^\circ$) and at an angle ($\theta_{in}>0^\circ$).

2.5 Conclusions

In this chapter, surface relief gratings were discussed, which can diffract light of different wavelengths into different directions. To get a strong angular separation among different colours, a small grating period close to the wavelength of visual spectrum should be chosen. The diffraction efficiencies of the transmitted and reflected orders of gratings were investigated using RCWA. The results show that the diffraction efficiency of the large-size grating is relatively insensitive to the angle of incidence in comparison to the small-size grating. More importantly, the diffraction efficiency can be optimised at relatively low relief height for the large-size grating, while the small-size grating requires a larger relief height to maximise the diffraction efficiency. Apparently, high diffraction efficiency requires a relatively large-size grating. This is in contrast with the strong angular dispersion requiring a small-size grating.

2.6 References

1. H. M. Whitney, M. Kolle, P. Andrew, L. Chittka, U. Steiner and B. J. Glover, *Science*, 2009, **323**, 130-133.
2. W. E. L. Grossman, *J Chem Educ*, 1993, **70**, 741-748.
3. E. Hecht, *Optics*, Chapter 10, Addison Wesley, 2002.
4. M. G. Moharam and T. K. Gaylord, *J Opt Soc Am*, 1982, **72**, 1385-1392.
5. T. M. de Jong, D. K. G. de Boer and C. W. M. Bastiaansen, *Opt Express*, 2011, **19**, 15127-15142.
6. M. C. Hutley and D. Maystre, *Opt Commun*, 1976, **19**, 431-436.
7. M. C. Hutley, *J Phys E Sci Instrum*, 1976, **9**, 513-520.
8. H. J. Gerritsen and M. L. Jepsen, *Appl Opt*, 1998, **37**, 5823-5829.
9. T. A. Strasser and M. C. Gupta, *Appl Opt*, 1994, **33**, 3220-3226.
10. L. Eisen, M. A. Golub and A. A. Friesern, *Opt Commun*, 2006, **261**, 13-18.
11. M. G. Moharam and T. K. Gaylord, *Appl Opt*, 1981, **20**, 240-244.
12. M. G. Moharam and T. K. Gaylord, *J Opt Soc Amer*, 1981, **71**, 811-818.

13. M. G. Moharam, E. B. Grann, D. A. Pommet and T. K. Gaylord, *J Opt Soc Am A: Opt Image Sci Vis*, 1995, **12**, 1068-1076.
14. M. G. Moharam, D. A. Pommet, E. B. Grann and T. K. Gaylord, *J Opt Soc Am A: Opt Image Sci Vis*, 1995, **12**, 1077-1086.
15. Grating Solver Development Co., <http://www.gsolver.com/>.
16. T. M. de Jong, PhD Thesis, Eindhoven University of Technology, Eindhoven, 2012.

3 Photoembossing via Mask Exposure

3.1 Introduction

In the previous chapter, a theoretical model was utilised to describe the diffractive properties of surface relief structures. By varying the grating design in the model we derived information on the desirable grating pitch and relief height of surface relief surfaces from a theoretical viewpoint with an emphasis on angular-dependent diffractive visual effects. In the past, various techniques were used to create the micro- and/or nano- structures including hot embossing, cast moulding and lithography.¹⁻³ In this chapter, we will report on photoembossing as a promising new technique that can be utilised to create the desired surface relief structures.⁴⁻¹⁰ The typical photopolymer mixture for photoembossing usually consists of a polymeric binder, a functional monomer, a photo-initiator and an inhibitor or retarder. This mixture is applied from solution to form a transparent solid thin film on the substrate. The photopolymer film is UV-irradiated through a photo-mask that is placed in close proximity of the film. This exposure locally activates the photoinitiator and generates free radicals. At room temperature these free radicals are relatively inactive because of diffusional mobility limitations. But when the sample is then heated, e.g. to a value above the glass transition temperature of the photopolymer, the mobility is increased and the polymerisation is started. The local consumption of monomer causes a reaction-driven diffusion

of reactive species from non-exposed (low exposed) areas to the exposed (high exposed) areas and a corresponding local volume change providing the relief structure. A flood exposure or a second heating step is applied to completely polymerise the relief structure and the dark areas during the first polymerisation step.¹¹⁻¹⁵ Various processing parameters influence the height and shape of the final relief structure, which include UV exposure dose, exposure time, development temperature, photopolymer blend composition, and film thickness.^{11, 16-18} Most of these parameters show an optimum level above which the relief height decreases again or remains constant.

More or less conventional systems for photoembossing are based on poly(benzyl methacrylate) (PBMA) as a polymeric binder and dipentaerythritol penta/hexa-acrylate (DPPHA) as a multi-functional monomer. However, a need persists to explore new systems for photoembossing with improved properties with respect to e.g. the height of the relief structures. Such systems are especially needed for applications in fibres (see also Chapter 5).

In this chapter, a new photopolymer system will be discussed in detail and compared to the conventional system. Polymers with an enhanced glass transition temperature will be explored in an attempt to improve the surface relief structure.

3.2 Experimental

Materials and Methods: Poly(benzyl methacrylate) (PBMA, $M_w=70$ kg/mol, Scientific Polymer Products) and Poly(methyl methacrylate) (PMMA, $M_w=120$ kg/mol, Sigma Aldrich) were used as the polymeric binder. Dipentaerythritol penta/hexa-acrylate (DPPHA, Sigma Aldrich) was used as the multifunctional monomer, Irgacure 819 (CIBA, Specialty Chemicals) as a photoinitiator, and tert-butyl hydroquinone (TBHQ, Sigma Aldrich) as the inhibitor/retarder. As a solvent a 50/50 wt% mixture of propylene glycol methyl ether acetate (PGMEA, Aldrich) and ethoxy propyl acetate (EPA, Avocado Research Chemicals) was used.

PBMA Photopolymer solutions were prepared using 47 wt% mixture of polymeric binder and monomer in ratio 1:1 (by weight), 3.6 wt% retarder, 2.4 wt% photoinitiator, and 47 wt% solvent mixture. PMMA photopolymer solutions were prepared using 3.6 wt% retarder, 2.4 wt% photoinitiator, 47 wt% solvent mixture, and 47 wt % mixture of polymeric binder and monomer in weight ratio 1:1 and 1:1.5, respectively.

The photopolymer solutions were spin-coated on the D263 glass substrates (5×5 cm) glass substrates with an RC-8 spin-coater (Suss Microtec, Garching, Germany). To remove the solvent, the samples were dried on a hotplate at 80 °C for 20 min and cooled afterwards to room temperature, resulting in dry films with a thickness of approximately 9-12 μm. The samples were exposed to UV-light from an OmniCure Series 2000 UV system (EXFO Photonic Solution Inc., Canada) in a nitrogen atmosphere. During exposure a square lithographic mask was placed onto the sample. On top and perpendicular to the line mask a lithographic optical density (OD) mask was placed in order to change the intensity of the light that reaches the sample. After exposure the masks were removed and the sample was gradually heated to the development temperature and kept for 10 minutes at this temperature in a nitrogen atmosphere. Finally, a flood exposure was applied at the development temperature in a nitrogen atmosphere.

Characterisation: The phase transition temperatures were determined with a TA Instruments Q1000 DSC. The thermal behaviour of the dry coatings was assessed by mechanically removing the coatings after the solvent was evaporated. The tested coatings did not contain photoinitiator.

The 3D images of surface relief structures were obtained by using confocal microscope (Sensofar, PLμ 2300) with a 50x objective. The pitch and relief height were measured from the profiles of surface relief structures.

3.3 Results and Discussion

Usually photo-embossing is performed using a contact mask exposure to facilitate processing and this requires a solid photo-resist with a glass transition temperature (T_g) above the room temperature to avoid contamination of the mask and damage to the film. In Fig. 3.1, the glass transition temperature of different polymer-monomer mixtures is plotted as a function of polymer weight fraction. In all cases, only a single phase transition is observed, which indicates the miscibility of polymeric binders and monomers. For both PBMA-DPPHA and PMMA-DPPHA systems, the T_g of photopolymer mixtures decreases rapidly with decreasing content of polymer. At a certain point, the T_g of the PBMA-DPPHA system is reduced to values around room temperature or below. The tackiness of the mixture increases and the photo-resist becomes more difficult to handle in contact mask exposure. The photopolymer mixture of PMMA-DPPHA system has a higher T_g at low monomer content, which is probably due to the higher T_g of the polymeric binder PMMA. The T_g of the PMMA-DPPHA system remains high in comparison to PBMA-DPPHA system and non-tacky mixtures are obtained even at relatively high monomer content (polymer:monomer = 1:1.5). Usually the T_g of the polymer mixture can be determined by using the Fox equation:¹⁹

$$\frac{1}{T_g} = \frac{w_1}{T_{g,1}} + \frac{w_2}{T_{g,2}} \quad (3.1)$$

where w_1 and w_2 are the weight fractions of components 1 and 2, respectively. $T_{g,1}$ and $T_{g,2}$ represent the corresponding glass transition temperatures of two components which are polymeric binder PMMA (or PBMA) and monomer DPPHA ($T_g = -36$ °C)²⁰ in this work. However, the T_g of the photopolymer mixture shows large deviation from the Fox equation, which is probably due to the specific interactions existent in the mixture, i.e. the hydrogen bonding.²¹⁻²⁴

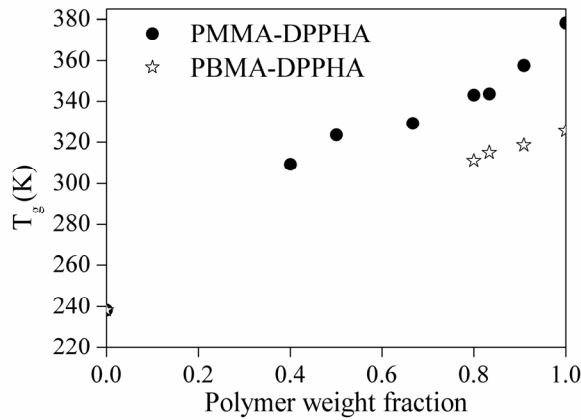


Figure 3.1: Glass transition temperature of PMMA-DPPHA and PBMA-DPPHA photopolymer mixtures as a function of polymer weight fraction.

The above-described results show that non-tacky mixtures of polymeric binders and monomers with T_g above room temperature can be obtained by a proper selection of the materials used. Next is to discuss the performance of the photopolymer systems in the photoembossing procedure, regarding the heights of the relief structures that are generated.

The photoembossing was first performed using a range of UV-light exposure dosages and at the development temperature of 110 °C for both PBMA-DPPHA (1/1) and PMMA-DPPHA (1/1) systems to obtain the optimum exposure dose. It was found that the optimum exposure dose is more or less the same for both PBMA-DPPHA and PMMA-DPPHA systems (see Fig. 3.2).

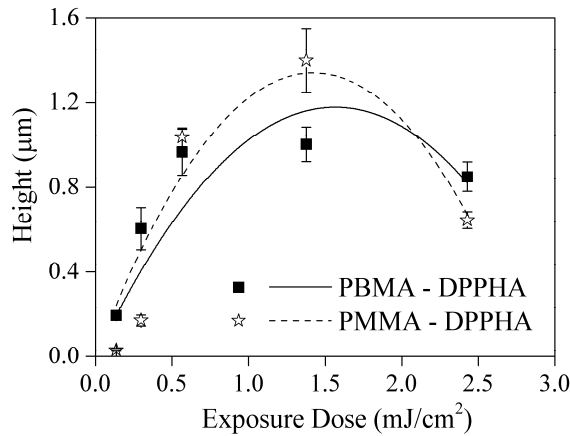


Figure 3.2: Relief height as a function of different exposure dose (20µm pitch) for PBMA-DPPHA (1/1) and PMMA-DPPHA (1/1) systems, respectively.

However, the optimum development temperature for the generation of the relief structures in the PMMA-DPPHA system is different from the PBMA-DPPHA system. As for the PMMA-DPPHA (1/1) system, the results, which are given in Fig. 3.3, show that a surface relief structure is generated above 50 °C and the height of the relief structure increases with the increasing development temperature. This is expected, because the monomer in the exposed area starts to polymerise above the T_g and also the system mobility is increased. A maximum height is obtained around 130 °C. After that, however, the height decreases again. Various reasons can be put forward for the decrease in the height, such as the decrease of polymerisation rate at high temperature, thermally initiated polymerisation, thermal degradation of the photoinitiator, or even the evaporation of the monomer or photoinitiator.²⁵ The optimum thermal development temperature for the PMMA-DPPHA system is approximately 20 °C higher than that for the PBMA-DPPHA system, which is not really surprising because of the increased T_g of the PMMA-DPPHA system in comparison to the PBMA-DPPHA system. In addition, a larger grating pitch leads to an increased relief height.

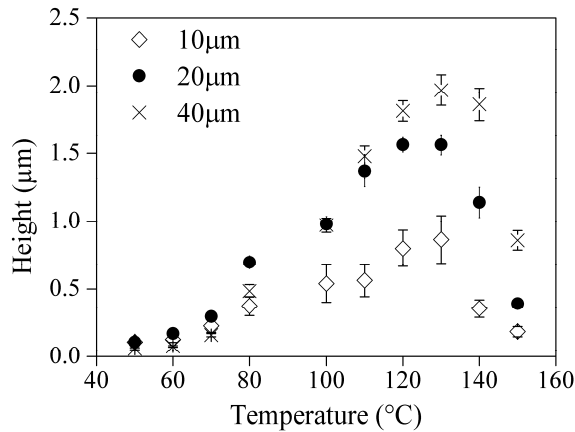


Figure 3.3: Relief height as a function of thermal development temperature for different pitches and PMMA-DPPHA system under the same optimum UV dose.

For each photopolymer mixture, the results of their photoembossing experiments based on the optimum conditions are plotted in Fig. 3.4. At identical monomer contents, the PMMA-DPPHA (1/1) system has a higher relief height, compared to the PBMA-DPPHA (1/1) system. The increase in the relief height is related to the diffusion of monomer from the non-exposed areas to the exposed areas before they are cured. The extent of diffusion is dependent on the interaction between the monomer and polymer, reactivity, monomer size and crosslinking ability.²⁶ A weaker polymer-monomer interaction allows an easier diffusion of monomer from the non-illuminated region to the illuminated region, which results in a higher relief height for the system with a same monomer concentration. The advantage of using a PMMA binder becomes more apparent at even higher monomer contents, i.e. PMMA-DPPHA (1/1.5) mixture. As for the PBMA-DPPHA system, very tacky samples are obtained when the monomer content is equal to or above 50 wt% of the mixture and the photopolymer mixtures cannot be processed easily any more, i.e. the photo-mask adheres to the mixtures and their residues tend to pollute the mask upon removal. In the case of the PMMA-DPPHA system, the monomer content can be increased above 50 wt% without

major tackiness issues and this leads to the increase in the height of the surface relief structures.

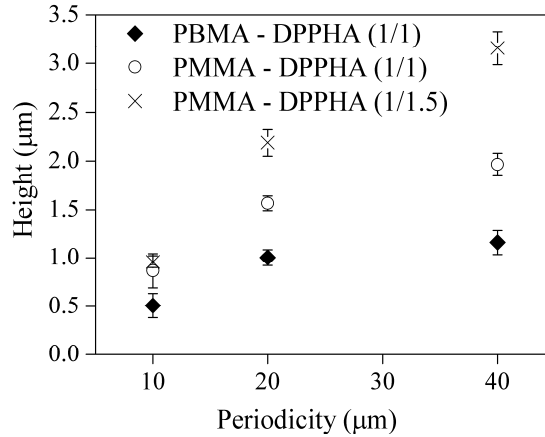


Figure 3.4: Relief height as a function of pitch for different photopolymer mixtures.

Next to relief height, the surface relief structures with various grating pitches formed using PMMA-DPPHA (1/1) photopolymer film are displayed in Fig. 3.5. It is observed that in the case of the 10 µm and 20 µm grating structures, the shape of surface relief structure resembles a sinusoid. In the case of the 40 µm grating structure, the surface relief profile shows a deviation from the sinusoidal shape due to the larger diffusion length.⁵

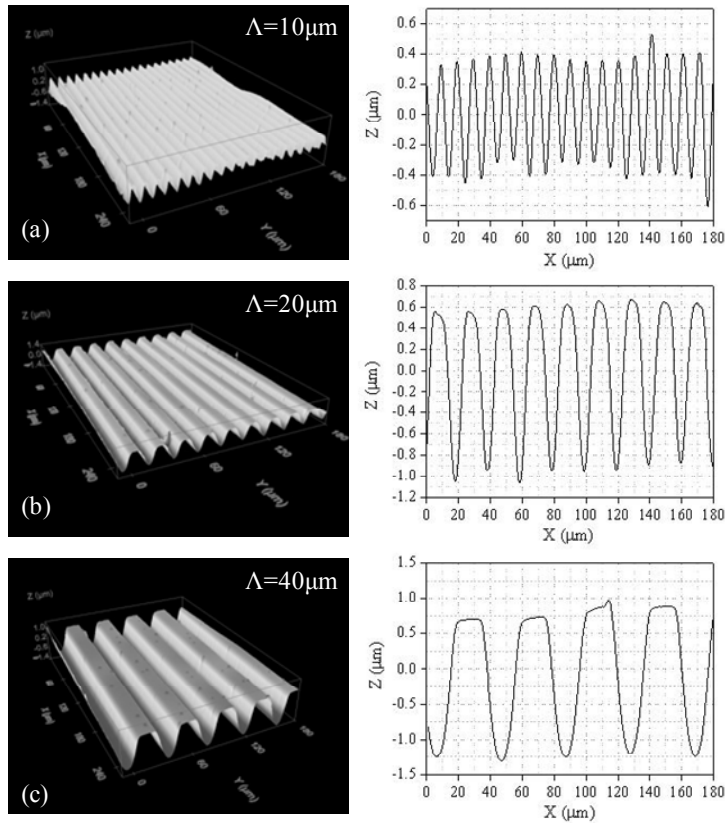


Figure 3.5: 3D confocal microscope images and corresponding cross section of surface relief structure formed by using PMMA-DPPHA (1/1) system with various grating pitches: (a) 10 μm , (b) 20 μm and (c) 40 μm .

3.4 Conclusions

In this chapter, the influence of the type and concentration of polymeric binder on the height of photoembossed relief structures were investigated. It is shown that the use of a polymeric binder (PMMA) with higher glass transition temperature requires a higher thermal development temperature and surface relief structures have been improved with respect to the relief height in comparison to the conventional photopolymer system (PBMA-DPPHA). More importantly, a higher monomer content is allowed for PMMA-DPPHA photopolymer system with respect to the glass transition temperature of the photopolymer mixture to

generate higher relief height. However, according to the calculated results presented in Chapter 2, smaller grating pitch is required. More effects on producing the gratings with desirable pitch and height need to be done, which will be discussed in Chapter 3.

3.5 References

1. D. Qin, Y. N. Xia and G. M. Whitesides, *Nat Protoc*, 2010, **5**, 491-502.
2. G. Fichet, N. Stutzmann, B. V. O. Muir and W. T. S. Huck, *Adv Mater*, 2002, **14**, 47-51.
3. E. Koukharenko, M. Kraft, G. J. Ensell and N. Hollinshead, *J Mater Sci-Mater El*, 2005, **16**, 741-747.
4. C. de Witz and D. J. Broer, *Polym Prepr*, 2003, **44**, 236-237.
5. C. F. van Nostrum, R. J. M. Nolte, D. J. Broer, T. Fuhrmann and J. H. Wendorff, *Chem Mater*, 1998, **10**, 135-145.
6. S. Piazzolla and B. K. Jenkins, *Opt Lett*, 1996, **21**, 1075-1077.
7. W. K. Smothers, B. M. Monroe, A. M. Weber and D. E. Keys, *Practical Holography IV*, 1990, **1212**, 20-29.
8. A. Liedtke, C. H. Lei, M. O'Neill, P. E. Dyer, S. P. Kitney and S. M. Kelly, *Acs Nano*, 2010, **4**, 3248-3253.
9. S. Liu, M. R. Gleeson, J. X. Guo and J. T. Sheridan, *Macromolecules*, 2010, **43**, 9462-9472.
10. F. T. O'Neill, I. C. Rowsome, A. J. Carr, S. M. Daniels, M. R. Gleeson, J. V. Kelly, J. R. Lawrence and J. T. Sheridan, *Opto-Ireland 2005: Photonic Engineering*, 2005, **5827**, 445-456.
11. K. Hermans, F. K. Wolf, J. Perelaer, R. A. J. Janssen, U. S. Schubert, C. W. M. Bastiaansen and D. J. Broer, *Appl Phys Lett*, 2007, **91**, 174103.
12. K. Hermans, C. W. M. Bastiaansen, D. J. Broer and J. Perelaer, Int. Pat., WO 2008025508, 2008.
13. K. Hermans, M. van Delden, C. W. M. Bastiaansen and D. J. Broer, *J Micromech Microeng*, 2008, **18**, 095022.

14. N. Adams, B. J. de Gans, D. Kozodaev, C. Sanchez, C. W. M. Bastiaansen, D. J. Broer and U. S. Schubert, *J Comb Chem* 2006, **8**, 184-191.
15. B. J. de Gans, C. Sanchez, D. Kozodaev, D. Wouters, A. Alexeev, M. J. Escuti, C. W. M. Bastiaansen, D. J. Broer and U. S. Schubert, *J Comb Chem*, 2006, **8**, 228-236.
16. C. Sanchez, B. J. de Gans, D. Kozodaev, A. Alexeev, M. J. Escuti, C. van Heesch, T. Bel, U. S. Schubert, C. W. M. Bastiaansen and D. J. Broer, *Adv Mater*, 2005, **17**, 2567-2571.
17. K. Hermans, S. Z. Harnidi, A. B. Spoelstra, C. W. M. Bastiaansen and D. J. Broer, *App Opt*, 2008, **47**, 6512-6517.
18. K. Hermans, I. Tomatsu, M. Matecki, R. P. Sijbesma, C. W. M. Bastiaansen and D. J. Broer, *Macromol Chem Physic*, 2008, **209**, 2094-2099.
19. W. Brostow, R. Chiu, I. M. Kalogeras and A. Vassilikou-Dova, *Mater Lett*, 2008, **62**, 3152-3155.
20. L. E. Schmidt, Y. Leterrier, D. Schmah, J. A. E. Manson, D. James, E. Gustavsson and L. S. Svensson, *J Appl Polym Sci*, 2007, **104**, 2366-2376.
21. X. Lu and R. A. Weiss, *Macromolecules*, 1992, **25**, 3242-3246.
22. J. H. Kim, B. R. Min and Y. S. Kang, *Macromolecules*, 2006, **39**, 1297-1299.
23. S. W. Kuo and F. C. Chang, *Macromolecules*, 2001, **34**, 5224-5228.
24. T. K. Kwei, *J Polym Sci Pol Lett*, 1984, **22**, 307-313.
25. D. J. Broer, G. N. Mol and G. Challa, *Polymer*, 1991, **32**, 690-695.
26. C. M. Lewis, A. M. de Jong, L. J. van IJzendoorn and D. J. Broer, *J Appl Phys*, 2004, **95**, 4125-4139.

4 Photoembossing via Interference Holography*

4.1 Introduction

In the previous chapter, a new photopolymer system (PMMA-DPPHA) was investigated in comparison to the conventional photopolymer system (PBMA-DPPHA). The use of polymeric binder with a high glass transition temperature proved to be useful for the enhancement of the surface relief structure and the ease of processing. However, the photoembossing presented in the previous chapter relies on a photo-mask to generate a UV-light patterned exposure. It is performed in a discontinuous process with static substrates, which limits the production speeds and in-line processing, e.g. continuous high-speed spinning line. The use of a photo-mask in combination with a moving substrate could be a costly technological challenge. Therefore, it is necessary to develop a technique for the patterned exposure, which can be compatible with the moving substrate.

In this chapter, the generation of UV-light patterns using interference holography with a continuous wave (CW) laser and a pulsed laser is reported. In the simplest case, two coherent laser beams with an equal linear polarisation direction are combined at an angle of 2θ on a photo-resist. The resulting

*This chapter is reproduced with the permission from *Macromol Mater Eng*:

O. T. Picot, R. Alcalá, C. Sánchez, M. Dai, N. F. Hughes-Brittain, D. J. Broer, T. Peijs and C. W. M. Bastiaansen, *Macromol. Mater. Eng.*, **2013**, 298, 33-37.

interference pattern has a period of $\lambda/2\sin\theta$ with λ being the wavelength of the light.¹⁻³ Compared to the photo-mask exposure, different grating spacings can be obtained with a single setup. To change the grating spacing only the angle between the interfering beams needs to be changed, while photo-mask photoembossing requires a new mask for every new spacing.⁴ More importantly, both static and dynamic substrates will be utilised to simulate processing conditions in a continuous operation, such as fibre spinning. The possibility of the interference holography using a CW laser and a pulsed laser to be incorporated in a continuous spinning line will be explored in this chapter.

Furthermore, to improve further on the compatibility of photoembossing with fibre spinning, a new photoembossing procedure is developed in which the patterned exposure is performed at high temperature. This method is compared to the classical photoembossing procedure where the patterned exposure is performed at room temperature, in terms of the relief height and optimum exposure energy.

4.2 Experimental

Materials: Poly(benzyl methacrylate) (PBMA, $M_w=70$ kg/mol, Scientific Polymer Products) and poly(methyl methacrylate) (PMMA, $M_w=120$ kg/mol) were used as polymeric binders and dipentaerythritol penta-/hexa-acrylate (DPPHA) as a multifunctional monomer. All materials were purchased from Sigma Aldrich. Irgacure 369 was applied as a photoinitiator and obtained from CIBA Specialty Chemicals (Germany).

The photopolymer solutions in propylene glycol monomethyl ether acetate (PGMEA) were prepared using polymeric binder and monomer in a 1:1 weight ratio and adding ~4.8 wt% of Irgacure 369. The obtained photopolymer solution was spin-coated on the glass substrates and the solvent was evaporated at 80 °C for 10 min to give films with a thickness of approximately 10 ± 1 μm .

Photoembossing using continuous wave (CW) and pulsed laser interference holography: Two types of lasers were utilised: an argon continuous wave laser operated at a wavelength of $\lambda=351$ nm and a pulsed Nd:Yag laser emitting a wavelength of $\lambda=1064$ nm. The pulsed laser is coupled to second and third harmonic modules to emit pulses of linearly polarised light with vertical polarisation and a wavelength of $\lambda=355$ nm. The pulse duration is 4 ns with a repetition rate of 10 Hz. The laser beam was split into two equal intensity beams to make an interference pattern on the substrate. The recording angle between two interference beams was 2.5° and 20.5° , which gave a grating pitch of ~ 8 μm and ~ 1 μm , respectively.

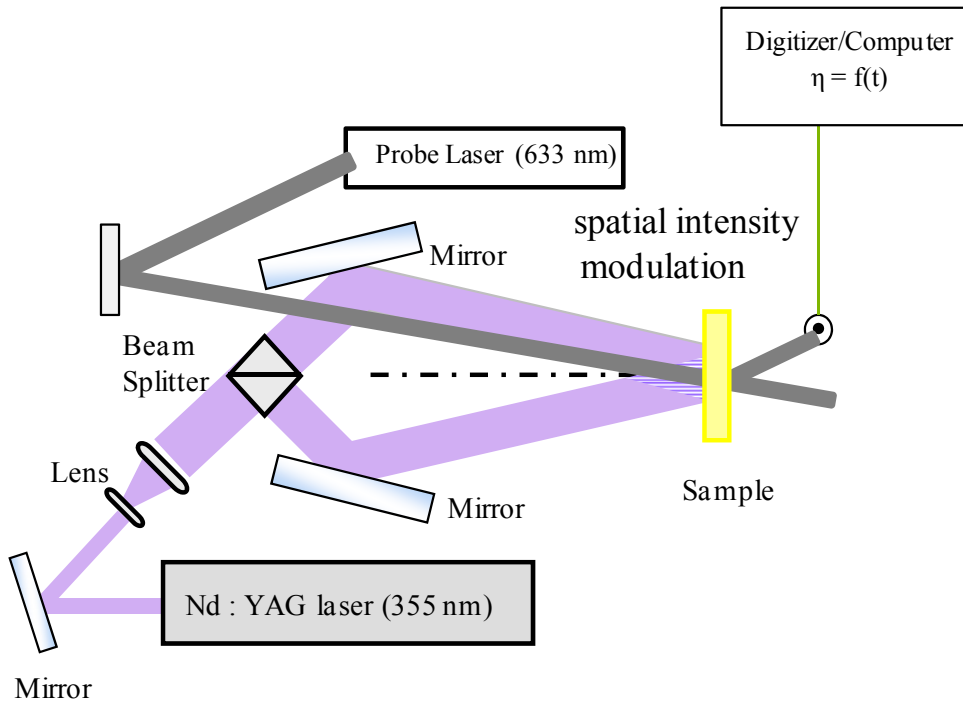
PBMA-DPPHA photopolymer system was first utilised to investigate the possibility of the interference holography using a CW and a pulsed laser to be incorporated in a continuous operation. The exposure of the photopolymer film to the UV pattern is performed at room temperature in air under two conditions: with a static substrate and with a moving substrate with a speed of approximately 0.05 $\text{m}\cdot\text{s}^{-1}$. In the latter case the displacement of the substrate is done perpendicularly to the incident beam. After exposure, the samples were heated to 80 $^\circ\text{C}$ for 10 min. The obtained structures were fixed using a flood exposure with a UV Exfo Mercury lamp for 10 min.

Room temperature (RT) and High temperature (HT) photoembossing: PMMA-DPPHA photopolymer system was utilised to improve the relief height. In RT photoembossing, the photopolymer films were exposed to UV interference pattern using the pulsed laser at room temperature in air. After exposure, the samples were heated at 130 $^\circ\text{C}$ for 10 min. The obtained relief structures were fixed by using a flood exposure via a UV Exfo Mercury Lamp for 10 min.

In HT photoembossing, the (PMMA-DPPHA) photopolymer films were preheated to 130 $^\circ\text{C}$ for 2 min and exposed to the UV interference pattern using the pulsed laser at 130 $^\circ\text{C}$. After exposure, the samples were heated at the same

temperature for 10 min. The obtained relief structures were fixed by using a flood exposure via a UV Exfo Mercury Lamp for 10 min.

The formation of the relief grating was monitored in-situ with a low power He-Ne laser at 633 nm by measuring the intensity of the +1 order diffracted beam in transmission mode during the thermal development (see Scheme 4.1).



Scheme 4.1: Illustration of pulsed laser interference holography setup with a probe laser in-situ monitoring the intensity of diffracted beam (+1 order).

Surface structure characterisation: The AFM investigation was performed using a Smena P47H microscope (NT-MDT Ltd, Russia) in semi-contact mode to measure the heights of the relief structures.

Diffraction efficiency measurement: A low power s-polarised He-Ne laser at 633 nm was used as the recording beam. The diffraction efficiency of the 0th transmitted order was measured as a function of relief height at normal incident.

4.3 Results and Discussion

4.3.1 Interference holography using CW and pulsed laser

The surface relief structures on PBMA-DPPHA photopolymer films are obtained by combining photoembossing with interference holography. First, an interference pattern is generated using the continuous wave laser. The height of the relief structures is plotted as a function of exposure energy for a moving substrate ($\dot{\epsilon} = 0.05 \text{ m}\cdot\text{s}^{-1}$) and a static substrate ($\dot{\epsilon} = 0 \text{ m}\cdot\text{s}^{-1}$) (see Fig. 4.1). It clearly demonstrates that a surface relief structure can be obtained with a static substrate. However, moving the substrate (translational motion) during the exposure does not produce any surface relief structures. The absence of surface relief structures on the moving substrate is directly related to the displacement of the substrate during the exposure, as light modulation sweeps the film along the grating vector direction, resulting in a homogeneous exposure dose all over the exposed area, i.e. the whole film is exposed to the same light dose.

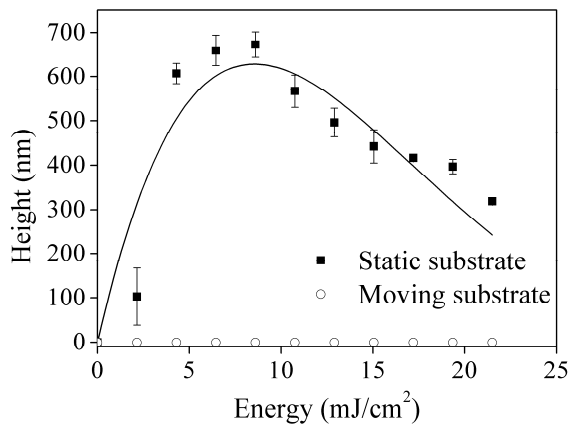


Figure 4.1: Relief height as a function of energy dose. Patterned exposure was done using a CW laser in combination with a static and a moving substrate.

Next, interference patterns are generated using a pulsed laser. A comparison is also done between a static substrate and a dynamic substrate (see Fig. 4.2). The result shows that desirable surface relief structures are produced in both static and

moving substrates, which is in contrast with the experiments done with the CW laser (see Fig. 4.1).

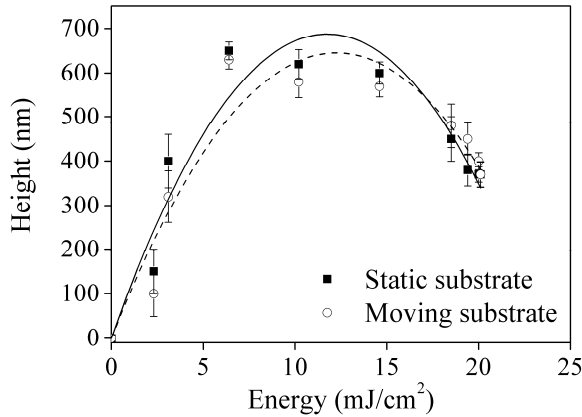


Figure 4.2: Relief height as a function of energy dose. Patterned exposure was done using a pulsed laser in combination with a static and a moving substrate.

In fact, to generate relief structures on a moving substrate, the exposure time needs to be short enough to obtain a small displacement of the substrate during the exposure compared to the grating pitch. Usually a pulsed UV-laser can provide exposure time in the range of a few nanoseconds. The displacement of the substrate during the exposure to a pulsed interference pattern is given by:

$$\Delta l = \dot{\epsilon} \times t \quad (4.1)$$

Where Δl is the displacement of the substrate (m), $\dot{\epsilon}$ the speed of the substrate ($\text{m}\cdot\text{s}^{-1}$) and t the pulse duration (s). In our experiments, $\dot{\epsilon}$ is $0.05 \text{ m}\cdot\text{s}^{-1}$ and t is 4×10^{-9} s. Therefore, the substrate displacement during the pulsed exposure is only 0.20 nm. As for an interference pattern with a grating pitch of 8000 nm, the displacement of the substrate during the exposure is small compared to the pitch. In other words, the sample can be considered to be nearly static during the 4 ns duration of the pulse and therefore similar relief modulation is obtained in moving and static substrates.

However, it should be noted that the height of the surface relief structure

presented here is in the order of hundreds of nanometres, which is rather low. Previously, it has been shown that addition of an inhibitor or retarder increases the relief height. This inhibitor forms a meta-stable compound with the initiator radicals and thereby preserves the radicals from reacting with ambient oxygen. When the film is heated, the meta-stable compound breaks down releasing the initiator for the polymerisation. Processing in a nitrogen atmosphere can improve the effect of inhibitor.^{5, 6} It was also shown in Chapter 3 that the chemical composition of the photopolymer mixture affects the relief height. It is anticipated that the effects of these parameters observed in these studies also apply to the systems presented here and that the dimensions of the relief structures can be improved.

More importantly for these experiments, the speed of the substrate was only $0.05 \text{ m}\cdot\text{s}^{-1}$ and it is interesting to estimate the maximum line speeds that are feasible in a continuous operation. Equation 4.2 expresses the maximum speed of the substrate $\dot{\epsilon}_{\text{max}}$ ($\text{m}\cdot\text{s}^{-1}$) to fully cover a moving film with surface relief structures without overlapping of continuous gratings. This equation is a function of the repetition rate of the laser f_{pulse} (Hz), the diameter of the laser beam d_{beam} (m) and the beam expansion factor k (Eq. 4.3).

$$\dot{\epsilon}_{\text{max}} = f_{\text{pulse}} \times d_{\text{beam}} \times k \quad (4.2)$$

$$k = \frac{d_{\text{hologram}}}{d_{\text{beam}}} \quad (4.3)$$

The laser used here produces a 6 mm wide circular beam with a repetition rate of 10 Hz, which limits the maximum speed of the substrate to $6 \times 10^{-2} \text{ m}\cdot\text{s}^{-1}$ without beam expansion ($k = 1$). This maximum speed of the substrate can be enhanced in a variety of ways. For instance, the laser beam can be expanded with the proper beam expander. However, the power of beam will be decreased at the same time. The exposure energy on the film should be kept high enough to get a high modulation surface relief grating. The pulsed laser used in our experiments can

only be expanded by factor of 3.5, resulting in an optimum energy (~ 8 mJ/cm) that leads to a maximum line speed of 2.1×10^{-1} m·s⁻¹. Several routes can be utilised to increase the maximum line speed, such as the use of higher energy or higher frequency lasers and the reduction of the optimum exposure energy required for photoembossing.

The above-described experimental data seem to indicate that pulsed laser interference holography is an excellent tool for generating relief structures in more or less classical continuous film/fibre production line. However, there are still several factors that need to be improved, i.e. an enhancement of the relief height to get high diffraction efficiency and a reduction of the optimum exposure energy for photoembossing to increase the maximum line speed. In this case, a new photoembossing procedure is developed in order to satisfy the requirements and this is to be discussed in next section.

4.3.2 RT photoembossing versus HT photoembossing

As mentioned above, in case of the classical photoembossing process (called room temperature (RT) photoembossing in this thesis), the patterned exposure is performed at room temperature. It is found that a low relief height in the order of hundreds of nanometres was obtained at a high exposure dosage (see Fig. 4.2), which is not beneficial to the incorporation of photoembossing in a high-speed spinning line and also to get a high diffraction efficiency. Here, a new photoembossing procedure was developed in order to enhance the relief height and reduce the optimum exposure energy. Also the PMMA-DPPHA photopolymer system was utilised instead of the PBMA-DPPHA system to enhance the height of surface relief structure. The PMMA-DPPHA photopolymer films were exposed to the pulsed laser at a high temperature (130 °C) and partly simultaneously and partly subsequently thermally developed at the same temperature, which is called high-temperature (HT) photoembossing in this thesis.

The comparison was done between the RT photoembossing and HT photoembossing, and the results are displayed in Fig. 4.3.

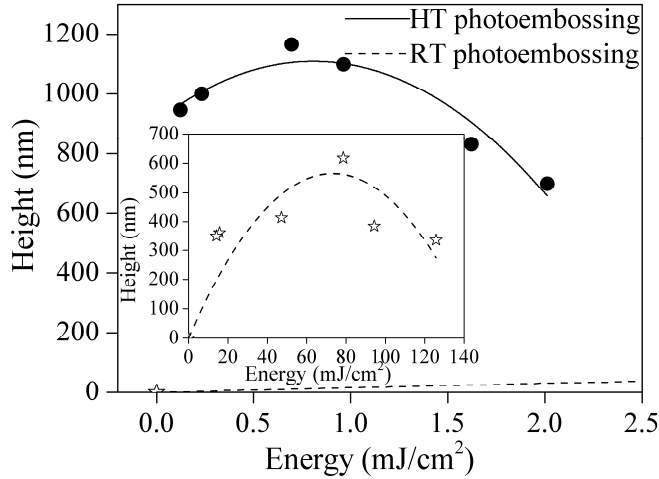


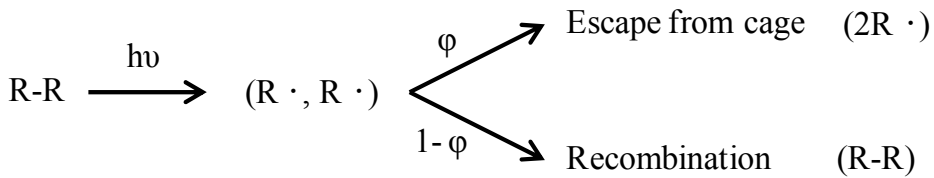
Figure 4.3: Relief height for grating pitch of $8\ \mu\text{m}$ as a function of exposure energy for HT photoembossing. The insert image is the relief height as a function of exposure energy for RT photoembossing.

It shows that by applying this specific HT photoembossing procedure, a much higher relief height is obtained. The optimum relief height goes even up to $\sim 1.2\ \mu\text{m}$, which is a significant enhancement (~ 2 times) compared to the RT photoembossing. The optimum exposure dosage is $\sim 0.6\ \text{mJ}/\text{cm}^2$, which is a dramatic reduction. This is attributed to the “cage effect”.⁷ The kinetics of the radical polymerisation can be described in terms of initiation, propagation and termination. During UV-initiation (see Scheme 4.2), reactive free radicals are formed from the decomposition of initiators. A pair of reactive free radicals may either undergo recombination due to the interaction with the surrounding molecules, or dissociation. The radicals escaped from the cage encounter with the reactive monomers and initiate polymerisation. In contrast, the loss of radical pairs induced by cage combination results in low efficiency of initiators. Under the steady-state conditions, the rate of polymerisation (R_p) can be expressed by Eq.

4.4⁸

$$R_p = k_p [M] \left\{ \varphi I_0 \left(1 - 10^{-\varepsilon [I_n] d} \right) / k_t \right\}^{1/2} \quad (4.4)$$

Where k_p and k_t are the propagation rate constant and termination rate constant, respectively, $[M]$ is the concentration of monomer, φ is radical separation quantum yield, ε is the molar extinction coefficient of the photoinitiator, $[I_n]$ is the concentration of the photoinitiator, I_0 is the intensity of the incident light and d is the thickness of the sample. Compared to the RT photoembossing, the HT photoembossing has a different radical quantum yield φ which is temperature-dependent.⁹ The cage effect appears to decrease with increasing the temperature and this effect is reflected in high polymerisation rate, enhancing the driving forces for monomer diffusion and thus the relief height.



Scheme 4.2: Photogeneration of reactive free radicals.

A representative AFM profile for this grating structure is shown in Fig. 4.4. A typical sinusoidal-shape relief structure is observed and an optimum relief height of $\sim 1.2 \mu\text{m}$ is obtained. Also, the formation process of the surface relief structure on the film is tracked by measuring the +1st transmitted order diffraction efficiency variations of the film during the thermal development. The result is plotted in Fig. 4.5. It illustrates that the diffraction efficiency (+1st order) of the film changes a lot for the first ~ 200 s and almost becomes constant after that. Since the diffraction efficiency is related to the relief height, it indicates that the diffusion of the reactive species is quite fast and the formation of the surface relief structure is almost done within the first ~ 200 s.

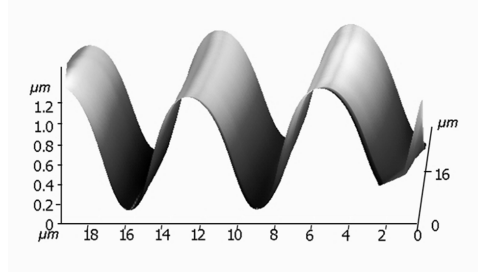


Figure 4.4: AFM profile of a surface relief structure for a pitch of $\sim 8 \mu\text{m}$.

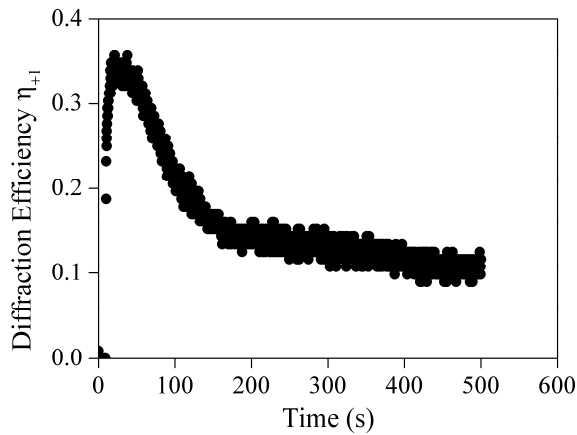


Figure 4.5: Diffraction efficiency (+1st order) of the film as a function of time during the thermal development.

Next, a smaller-size relief structure with a grating pitch of $1 \mu\text{m}$ was created on the surface of films. A comparison between the gratings of $8 \mu\text{m}$ and $1 \mu\text{m}$ is shown in Fig. 4.6. It demonstrates that for the grating of $1 \mu\text{m}$, higher exposure energy is required to get the optimum relief height. This can be explained by the diffusion-polymerisation model developed by Leewis, et al.¹⁰ From the beginning, with increasing the exposure energy, the concentration of radicals increases and thus the relief height increases. In this exposure dose range, the crosslinking does not hinder the diffusion of monomer and a maximum relief height is achieved eventually. Then, the relief height decreases with exposure energy further increasing, which is known as overexposure (above the optimum exposure), the excessive crosslinking of the overexposed area prevents the un-reacted monomers

from diffusing into the centre part of the exposed area. The monomers accumulate near the edges of the exposed area and as a result, two extra peaks appear there. However, as for the smaller grating pitch, these two side shoulders vanishes completely unless a much higher energy dose is applied, which is due to the smaller diffusion length and steeper monomer concentration gradient. Therefore, the optimum exposure energy for the smaller grating pitch is much larger and the maximum relief height obtained for the smaller grating pitch is much lower, which can be explained by the energy cost for the generation of relief surface. The decrease of grating pitch keeping the same height leads to the generation of more surfaces and this is expensive in terms of energy.¹¹⁻¹³ A typical AFM profile for this smaller-size relief structure is shown in Fig. 4.7. A sharp sinusoidal-shape relief structure is formed and an optimum relief height of ~ 90 nm is obtained.

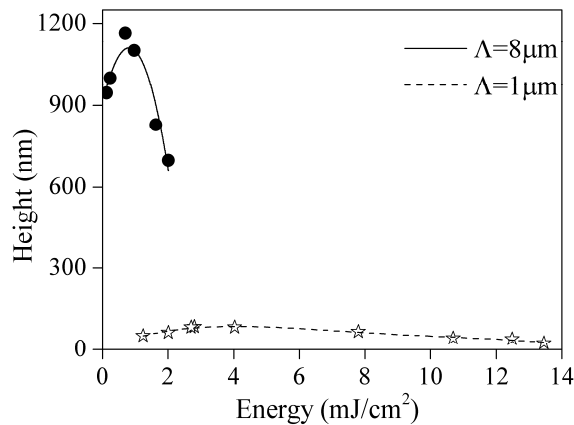


Figure 4.6: Relief height for grating pitch of $8\ \mu\text{m}$ and $1\ \mu\text{m}$ as a function of exposure energy.

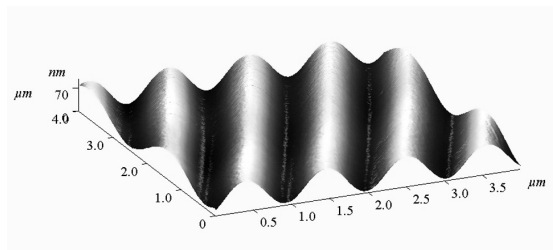


Figure 4.7: AFM profile of a surface relief structure for a pitch of $\sim 1\ \mu\text{m}$.

The experimental data show that by applying HT photoembossing, the height of the surface relief structure can significantly be enhanced. The diffraction efficiency of such surface relief structure is expected to increase as well. Here, the diffraction efficiency in transmission mode was measured as a function of the relief height at normal incidence. The results are compared to the calculated data based on the simulations with the assumption that the grating has a sinusoidal profile and the incident light is defined by specifying its wavelength ($\lambda=633$ nm) with s-polarisation. Since it is difficult to measure the diffraction efficiency of all transmitted orders ($m \neq 0$), the efficiency of the 0th transmitted order is selected to make the comparison, which in fact gives the inverse efficiency. The comparison for the grating pitches of 8 μm and 1 μm is plotted in Fig. 4.8. The result shows that the measured and simulated results are in good agreement. In the case of the large grating pitch (8 μm), a surface relief grating with the optimum height around 1.0 μm can be fabricated by applying HT photoembossing with a minimum inverse efficiency (η_0). In other words, a maximum diffraction efficiency is obtained. Compared to the surface relief grating with a height around 600 nm created using classical RT photoembossing, the diffraction efficiency is dramatically improved. However, in the case of the small grating pitch (1 μm), the obtained relief height (approximately 90 nm) is still far away from the optimum height for the maximum diffraction efficiency.

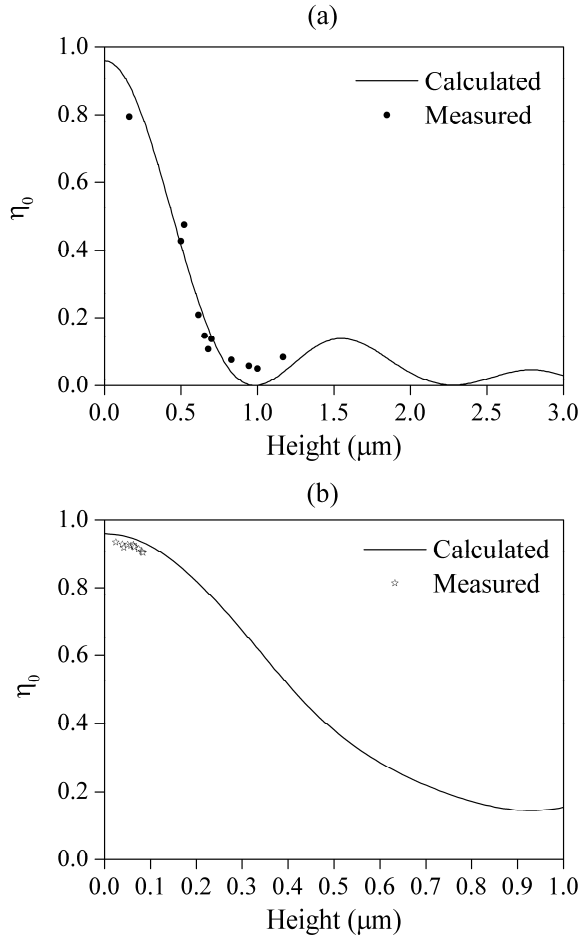


Figure 4.8: Measured and calculated (RCWA) efficiency of 0th transmitted order as a function of relief height for the surface-relief profiles with the pitch of $8 \mu\text{m}$ (a) and $1 \mu\text{m}$ (b): $\lambda = 633 \text{ nm}$, s-polarised light, normal incidence.

More importantly, by applying HT photoembossing, the optimum exposure energy required for the photoembossing is dramatically reduced. We can imagine that the maximum moving speed of substrate can be increased as well. For instance, in the case of the grating pitch of $8 \mu\text{m}$, the optimum exposure energy is reduced to $\sim 0.6 \text{ mJ}\cdot\text{cm}^{-2}$ by applying HT photoembossing. The pulsed laser used in the experiments can be expanded by factor of ~ 46 , leading to a maximum line speed of $2.8 \text{ m}\cdot\text{s}^{-1}$, which is approximately 13 times faster than the maximum line speed ($2.1 \times 10^{-1} \text{ m}\cdot\text{s}^{-1}$) as for the classical RT photoembossing. This maximum line

speed can still be further improved to be compatible with high-speed spinning line by applying a pulsed laser with a much higher energy or frequency in the industry, instead of the pulsed laser that was used in the lab.

4.4 Conclusions

In this chapter, it is demonstrated that surface relief structures can be generated by photoembossing in a moving photopolymer film using pulsed laser interference holography, which is potentially compatible with a continuous operation such as fibre spinning line. The system is insensitive to translational motion of the substrate due to the short time exposure compared to CW recording, which makes it interesting for industrial applications. It is also shown that the maximum speed of the substrate is rather low and limited by the laser specifications. Several routes are proposed for increasing line speeds such as the reduction of the laser energy required for photoembossing. In this case, a new route, HT photoembossing was developed to create surface relief structures. Compared to the classical RT photoembossing, lower optimum exposure energy is required and a higher relief height can be achieved at the same time. The measurements of diffraction efficiency show that an enhanced relief height leads to a higher diffraction efficiency, which is in consistent with the calculated data. More importantly, the reduction of the optimum exposure energy leads to the increase of the maximum line speed, which contributes to the incorporation of the photoembossing process in a high-speed spinning line.

4.5 References

1. D. Y. Xia, Z. Y. Ku, S. C. Lee and S. R. J. Brueck, *Adv Mater*, 2011, **23**, 147-179.

2. T. R. Zhai, X. P. Zhang, Z. G. Pang and F. Dou, *Adv Mater*, 2011, **23**, 1860-1864.
3. S. R. J. Brueck, *Proc IEEE*, 2005, **93**, 1704-1721.
4. C. van Heesch, PhD Thesis, Eindhoven University of Technology, NL, 2007.
5. K. Hermans, F. K. Wolf, J. Perelaer, R. A. J. Janssen, U. S. Schubert, C. W. M. Bastiaansen and D. J. Broer, *Appl Phys Lett*, 2007, **91**, 174103.
6. K. Hermans, I. Tomatsu, M. Matecki, R. P. Sijbesma, C. W. M. Bastiaansen and D. J. Broer, *Macromol Chem Physic*, 2008, **209**, 2094-2099.
7. I. V. Khudyakov and N. J. Turro, *Des Monomers Polym*, 2010, **13**, 487-496.
8. D. J. Broer, G. N. Mol and G. Challa, *Polymer*, 1991, **32**, 690-695.
9. C. Dupuy and H. Vandenbergh, *Chem Phys Lett*, 1978, **57**, 348-351.
10. C. M. Leewis, A. M. de Jong, L. J. van IJzendoorn and D. J. Broer, *J Appl Phys*, 2004, **95**, 4125-4139.
11. N. Adams, B. J. de Gans, D. Kozodaev, C. Sanchez, C. W. M. Bastiaansen, D. J. Broer and U. S. Schubert, *J Comb Chem* 2006, **8**, 184-191.
12. B. J. de Gans, C. Sanchez, D. Kozodaev, D. Wouters, A. Alexeev, M. J. Escuti, C. W. M. Bastiaansen, D. J. Broer and U. S. Schubert, *J Comb Chem*, 2006, **8**, 228-236.
13. C. Sanchez, B. J. de Gans, D. Kozodaev, A. Alexeev, M. J. Escuti, C. van Heesch, T. Bel, U. S. Schubert, C. W. M. Bastiaansen and D. J. Broer, *Adv Mater*, 2005, **17**, 2567-2571.

5 Surface Structuring of Fibres using Photoembossing*

5.1 Introduction

In the previous two chapters, it was presented that the photoembossing could be used to create the surface relief structures on films. All processing conditions were optimised, e.g. the selection of polymeric binder, patterned exposure via interference holography, processing temperature and exposure energy, in order to enhance the surface structures. In addition, the conditions of formation of these structures were improved on their feasibility of being incorporated into a continuous spinning line. In this chapter, the surface structuring of fibres using photoembossing will be reported. Previously, specific die designs or mechanical embossing have been used to generate fibres with relief structures along/perpendicular to the fibre length. However, all these technologies have their own disadvantages that were already discussed in Chapter 1. Photoembossing is for the first time utilised to create the structure on the surface of fibres, which is perpendicular to the fibre axis. It is potentially capable to be incorporated into a

*This chapter is reproduced by permission of The Royal Society of Chemistry:

1. M. Dai, O. T. Picot, N. F. Hughes-Brittain, T. Peijs and C. W. M. Bastiaansen, *J. Mater. Chem.*, **2011**, 21, 15527-15531.

2. M. Dai, T. M. de Jong, Carlos Sánchez, O. T. Picot, D. J. Broer, T. Peijs and C. W. M. Bastiaansen, *RSC Adv.*, **2012**, 2, 9964-9968.

high-speed spinning line and also allows the formation of relief structures in a large number of parallel fibres.

The organisation of this chapter is as follows: first it is discussed in detail whether the photopolymer mixture can be directly spun into single fibres and subsequently photoembossed. Furthermore, bi-component fibre system consisting of common synthetic fibre as core fibre and photopolymer coating is explored to enhance the fibre properties and appearance.

5.2 Surface Structuring of Single Fibres

The typical photopolymer mixture applied for photoembossing consists of a polymeric binder, multifunctional monomer and photoinitiator.¹⁻¹¹ In the previous chapters, it was shown that the utilisation of PMMA-DPPHA photopolymer mixture can improve the surface relief structures, compared to the conventional PBMA-DPPHA photopolymer mixture. This section will first report on the spinnability of the PMMA-DPPHA photopolymer mixture with respect to the rheological properties and eventually the characterisation of the photoembossed fibres.

5.2.1 Experimental

Materials: Poly(methyl methacrylate) (PMMA, $M_w=120$ kg/mol) was used as the polymeric binder, dipentaerythritol penta-/hexa-acrylate as the multifunctional monomer and tert-butyl hydroquinone (TBHQ) as the inhibitor/retarder. All materials were purchased from Sigma Aldrich (United State). Irgacure 819 was applied as the photoinitiator and was obtained from Ciba Specialty Chemicals (Germany).

Melt-spinning of photopolymer mixture: The photopolymer mixture consisted of PMMA and DPPHA (the ratio of polymer to monomer is 1:1) and ~4.4 wt% of Irgacure 819 (photoinitiator) and ~6.9 wt% of TBHQ (inhibitor) were added. This

photopolymer mixture was first dissolved in acetone in a 1:3 weight ratio via stirring and then dried in an oven under vacuum at 80 °C for 3 days to remove the solvent residues. After drying, solid glassy films were obtained. A simple granulation/grinding process at room temperature was used to make photopolymer pellets for spinning.

The photopolymer pellets were melt-spun into monofilaments at 110 °C by using a mini-melt-spinning apparatus which consists of a piston equipped with a heating jacket (see Fig. 5.1). Thermal polymerisation of the monomer should not occur while spinning at 110 °C because it will result in changes in rheological properties in time or even in complete crosslinking of the system prior to spinning, therefore, a low spinning temperature was applied. The molten photopolymer mixture was pumped through a single-nozzle circular die (1 mm diameter) to form photopolymer fibres, which were solidified in air as they proceed to be collected on a rotating bobbin. The winding speed of the rotating bobbin was varied to produce the fibres with diameters between 0.5 and 0.1 mm. The subsequent photoembossing of the fibres was performed in a separate operation (off-line).

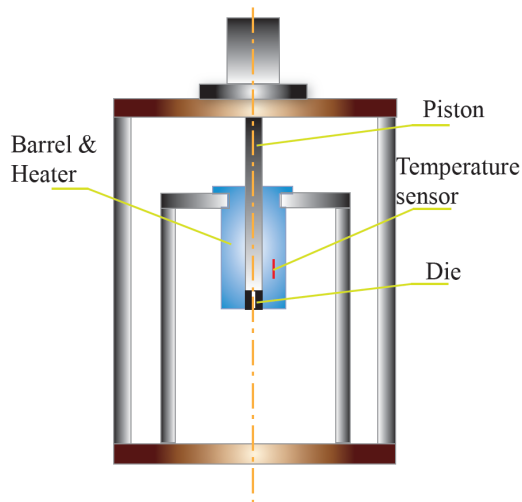


Figure 5.1: *A schematic of mini-extruder.*

Photoembossing of fibres: The photopolymer fibres were exposed to UV-light using an OmniCure Series 2000 UV system (EXFO Photonic Solution Inc., Canada) for 70 s in a nitrogen atmosphere with a lithographic mask (grating) placed on top of the fibres. The UV light had an intensity of $2 \times 10^{-2} \text{ W} \cdot \text{cm}^{-2}$ ($\lambda=320\text{-}500 \text{ nm}$). After exposure, the mask was removed and the fibre was gradually heated to 130 °C and kept at 130 °C for 10 min in a nitrogen atmosphere. The fibres were exposed completely to the UV light (i.e. a flood exposure was applied) in a nitrogen atmosphere at 130 °C to fix the relief structure.

Characterisation: The DSC traces of the multifunctional monomer dipentaerythritol penta-/hexa-acrylate was obtained by using a Q1000 DSC (TA instruments, United States). The sample was weighed in a DSC aluminium pan in air and the pan was sealed after that. Then, it was heated from -30 to 250 °C at a rate of $5 \text{ }^\circ\text{C} \cdot \text{min}^{-1}$.

The flow behaviour of the photopolymer mixture was characterised via a stress-controlled AR-G2 rheometer (TA Instruments, United States) using a 25 mm parallel plate-plate geometry and disk-shape specimens (25 mm in diameter; 1 mm in thickness). Frequency sweeps in the range of 100-0.01 rad/s were performed at a temperature ranging from 60 to 130 °C in a N₂ atmosphere at a constant strain of 1 %, which was within the linear viscoelastic range.

Morphological investigations of the relief structure on the surface of the fibre were performed with Leica DM6000 optical microscope with a 50 × objective. The measurement of the relief structure on the surface of fibre was carried out using a FEI Quanta 3D Scanning Electron Microscope. To prevent charging in the electron beam, a thin gold layer was coated on the surfaces of fibres by vapour deposition. The height of the relief structure on the surface of fibre was measured for each pitch of the gratings.

5.2.2 Results and discussion

The thermal stability of the photopolymer mixture is important for the fibre spinning operation and this was investigated with the DSC experiments. A typical DSC curve for the monomer DPPHA (containing 500 ppm of monomethyl ether hydroquinone as inhibitor) is depicted in Fig. 5.2. The exothermic peak in the DSC curve suggests that thermal polymerisation of the monomer occurs above 200 °C. The processing temperature during the fibre spinning process is therefore kept below 130 °C to be sure that premature polymerisation is avoided.

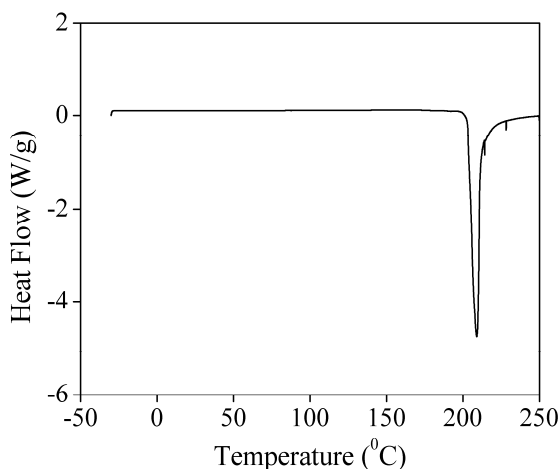


Figure 5.2: DSC curve of the monomer DPPHA.

Before the photopolymer mixture was used for fibre spinning, the rheological properties of the PMMA-DPPHA (1/1) photopolymer mixture were investigated. The storage and loss moduli G' and G'' as a function of the angular frequency ω for the photopolymer mixture are shown in Fig. 5.3 at different temperatures.

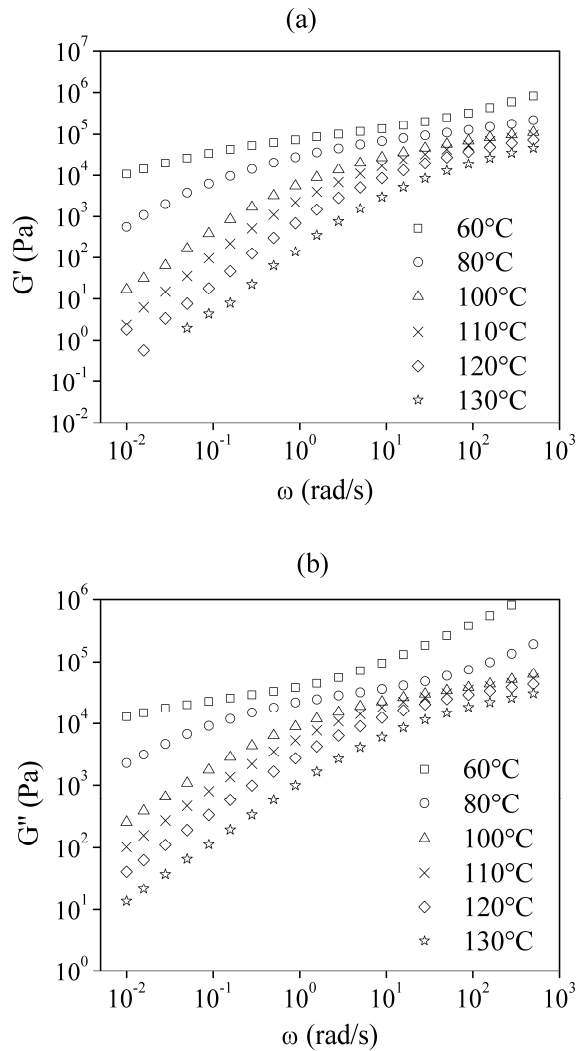


Figure 5.3: Storage and loss moduli G' and G'' for the photopolymer mixture as a function of angular frequency ω in a temperature range of 60-130 °C.

To investigate the flow behaviour of the photopolymer mixture at a broad frequency range, time-temperature superposition (TTS) was utilised.¹² Here 110 °C was chosen as the reference temperature. The master curves of the photopolymer mixture are shown in Fig. 5.4. In Fig. 5.5, the master curve of the complex viscosity as a function of the angular frequency ω for the photopolymer mixture is shown. All the experimental results in Fig. 5.4 and Fig. 5.5 indicate that

the polymer/monomer mixtures are viscoelastic. The melt has a zero shear viscosity of approximately 10^4 Pa·S and shows shear rate dependence. The viscosity drops when the angular frequency (shear rate) increases, showing a significant shear thinning behaviour, which is an indication that a spinnable fluid has been generated.^{13, 14}

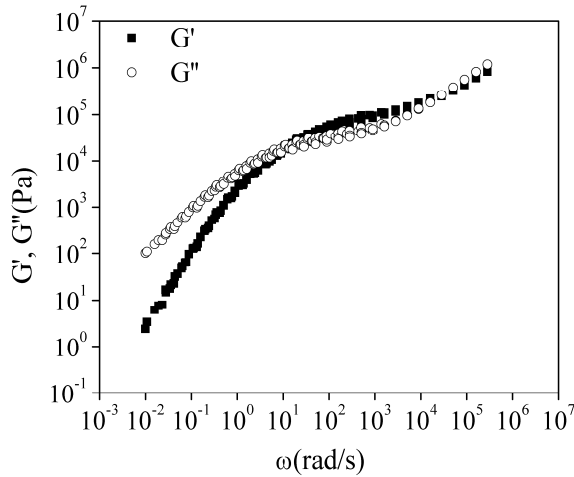


Figure 5.4: The master curves of G' and G'' for the photopolymer mixture as a function of angular frequency at $T_r = 110$ °C.

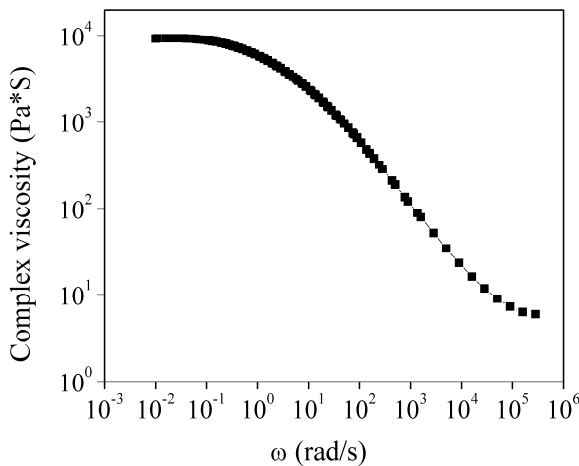


Figure 5.5: The master curve of the complex viscosity for the photopolymer mixture as a function of angular frequency at $T_r = 110$ °C.

Next, photopolymer fibres were prepared by spinning of the photopolymer mixture at 110 °C. After spinning and cooling down to room temperature, the photopolymer mixture has a glass transition temperature above it and, consequently, vitrified fibres were obtained which could be collected on a bobbin. Photopolymer fibres with different diameters were obtained by varying the rotational speed of the bobbin. The diameter of the obtained thinnest photopolymer fibre was around 0.10 mm. Subsequently, the photoembossing process was applied to the fibres using a photo-mask exposure. Fig. 5.6 shows optical microscopy images of the surface structures of obtained patterned fibres with different diameters. It indicates that the relief structures are formed on the surface of the fibres perpendicular to the fibre axis no matter how thin the fibre is.

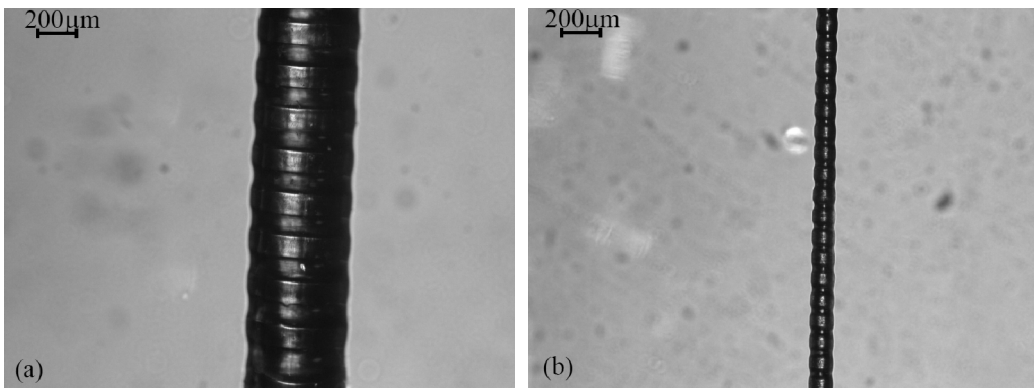


Figure 5.6: *Optical microscopy images of the relief structures on the surface of the patterned fibre with different diameters: (a) ~0.50 mm and (b) ~0.10 mm.*

The fibres were mask-exposed from a single side. It was therefore of interest how the relief shape was changing along the periphery of the fibre. Fig. 5.7 exhibits optical microscopy images of the surface structures on both top (a) and bottom (b) surfaces of the same part of the patterned fibres which indicate that an almost identical relief structure is generated on both top and bottom sides of the fibres.

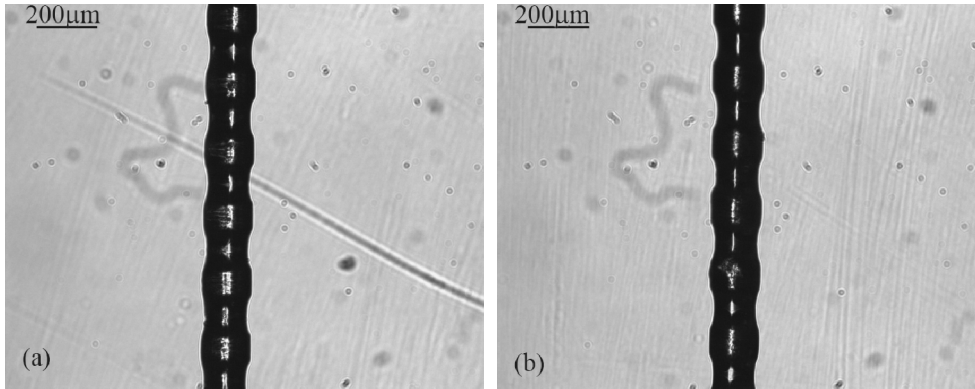


Figure 5.7: *Optical microscopy images of the top (a) and bottom (b) surfaces of the patterned fibre. Diameter of the fibre is ~ 0.10 mm and the pitch of relief structure is $200 \mu\text{m}$.*

To characterise the relief structures on the surfaces of fibres in more detail, SEM images were taken and the heights of the relief structures on the surfaces of fibres were measured. Fig. 5.8 shows the height of the relief structure on the surface of the patterned fibres with the diameter of ~ 0.50 mm and ~ 0.10 mm, respectively. As expected, it is observed that the height of the relief structures depends on the pitch of the relief structures, i.e. the height of the relief structures increases with increasing pitch. Also, a higher height of the relief structure (at large pitches) is achieved using photopolymer fibre with larger diameter (~ 0.5 mm). Apparently, when the pitch size exceeds the diameter of the photopolymer fibre, the relief height is influenced by the fibre diameter.

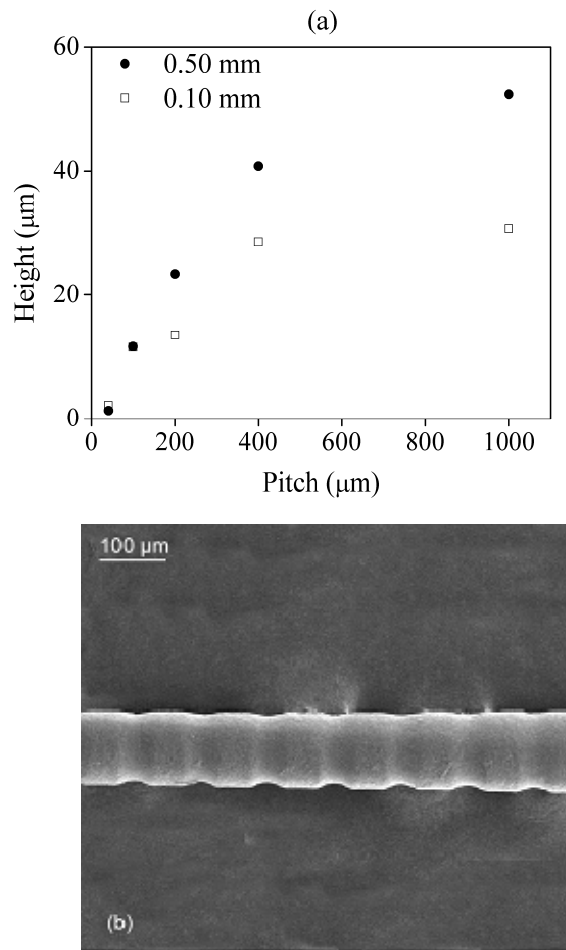


Figure 5.8: (a) Height of the relief structures on the surfaces of fibres with the diameters of ~ 0.10 mm and ~ 0.50 mm for different pitches: 40 μm , 100 μm , 200 μm , 400 μm and 1000 μm . (b) SEM image of the patterned fibre with a diameter of ~ 0.10 mm and a pitch of 100 μm . The SEM image is taken to measure the height of the relief structure.

A few critical remarks are appropriate with respect to the experimental data presented here. First, the monofilament fibres are extremely brittle after spinning and also after photo-patterning and complete conversion of the monomer to polymer. Directly after spinning, a vitrified solution of a brittle polymer in a monomer is obtained and a brittle fibre is therefore to be expected. After the photoembossing, a crosslinked system is obtained which also is expected to have a very low strain at break. Secondly, the structured fibres presented here have a

larger grating pitch ($> 40 \mu\text{m}$) and consequently pronounced angular-dependent colours are not expected and observed. To improve the mechanical performance of these fibres and also get the desired angular-dependent visual effects, bi-component fibres are to be explored and attempts to reduce the grating pitches are done in the next section.

5.3 Surface Structuring of Bi-component Fibres

To overcome the problems discussed in previous section, a bi-component fibre was prepared, which consists of a polyester (PET) core fibre and a functional coating. A synthetic core fibre is employed to avoid brittleness of the fibre and to provide mechanical stability, while a thin photopolymer coating is applied to generate a diffraction grating structure on the surface of the fibre via photoembossing. The patterned exposure in photoembossing is performed via interference holography using a pulsed laser (4 ns pulse duration) which is expected to allow continuous spinning processes.¹⁵ HT photoembossing, as introduced in Chapter 4, is applied to improve the structures on the surface of bi-component fibres. All the processing conditions were discussed in the previous chapters and will be directly utilised in this section.

The whole procedure will be incorporated into a continuous spinning line, as shown in Fig. 5.9. The common polymer pellets for textile fibres are extruded out from the spinning die, cooled and stretched. Subsequently, the mono/multifilaments are coated with the photopolymer mixture, exposed to a holographic interference pattern using a pulsed laser, and then thermally or UV cured. Finally, fibres with surface relief gratings are collected.

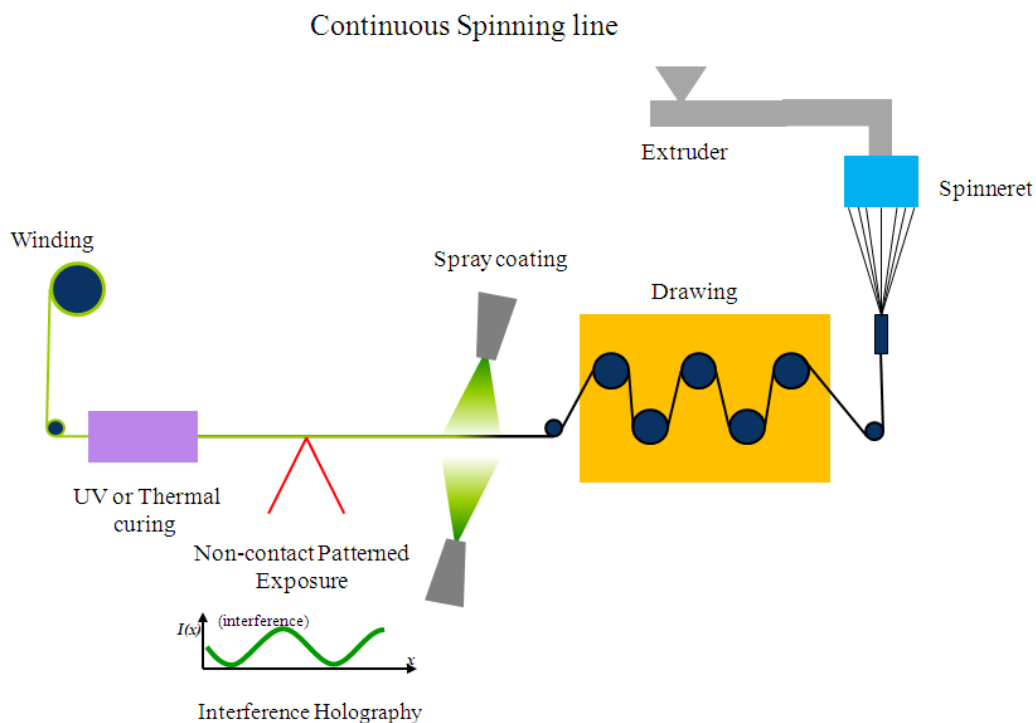


Figure 5.9: Schematic representation of incorporation of photoembossing via interference holography into a continuous spinning line.

5.3.1 Experimental

Materials: PMMA photopolymer mixture were prepared using 47.6 wt% of PMMA ($M_w=120$ kg/mol) polymer, 47.6 wt% of DPPHA monomer and 4.8 wt% of Irgacure 369 and dissolved in propylene glycol methyl ether acetate (PGMEA) in weight ratio of 1:10.

PET monofilaments were melt-spun using PET granulates (M_n : ~18,500, MFI: ~135g/10 min (280 °C, 2.16 kg), T_g : 79 °C, T_m : 258 °C, X%: 24%) received from Teijin and post-drawn to a draw ratio of 3 ~ 3.5 at ~90 °C. The diameter of obtained PET monofilaments is $\sim 185 \pm 15$ μm .

Photoembossing of fibres: The PET monofilaments were spray-coated using an airbrush with the PMMA photopolymer solution. During spraying, most of PGMEA solvent was removed under the high air pressure of the airbrush. After

spraying, the bi-component fibres were heated again at 80 °C for 20 min to remove the residual traces of solvent. To induce a grating structure on the surface of fibres, a pulsed Nd:Yag laser was coupled to second and third harmonic modules to emit 4 ns pulses of 355 nm linearly polarised light with vertical polarisation. The laser beam was split into two equal intensity beams, which were subsequently combined to make an interference pattern on the substrate. The recording angle between the two interfering beams was 2.5° and 20.5°, which gave a grating pitch of ~8 µm and ~1 µm, respectively. The photopolymer fibres were fixed on a sealed hot-stage at 130 °C with an opening facing the interfering beams (see Fig. 5.10) and subsequently exposed to the laser interference pattern. The exposure energies were optimised for respectively a grating pitch of 8 µm (exposure energy: ~0.6 mJ/cm²) and for grating pitch of 1 µm (exposure energy: ~3.0 mJ/cm²). During the procedure, only the two ends of the fibres touched the hot-stage and the real temperature of the central part of fibres could be lower than the temperature of the hot-stage. After exposure, the fibres were kept at 130 °C for 10 min for thermal development. The obtained relief structures were chemically fixed by a flood exposure to a UV Exfo Mercury lamp for 10 min at room temperature.

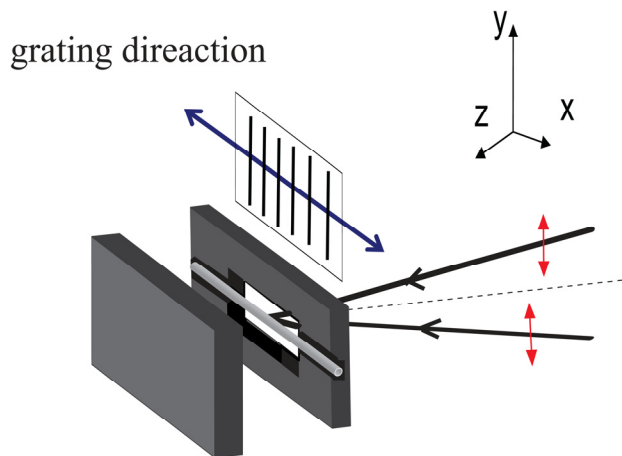


Figure 5.10: Schematic representation of the hot-stage set-up.

Characterisation: The investigation of the cross-section and the surface-relief structure of the bi-component fibres were also carried out using a FEI Quanta 3D Scanning Electron Microscope.

Mechanical properties of the original PET fibres, annealed PET fibres, the coated PET fibres and the structured fibres were measured using a tensile tester Z010 (Zwick Co., Germany) at a speed of 0.1 % strain per second. Here, for reference purposes, the PET fibres were post-annealed at 80 °C and 130 °C at a fixed length and exposed using a UV lamp for 10 min at room temperature. The coated PET fibres were also post-annealed at 130 °C at a fixed length and cured using a UV lamp for 10 min at room temperature. Since the length of the grating structure on the surface of fibre is limited (<6 mm long), the gauge between the two clamps is ~5 mm.

The investigation on the angular dispersion of the gratings on fibres was carried out using an Autronic DMS 703 (Melchers GmbH) together with a CCDSpect-2 array detector (CCD-camera). The sample was placed in a custom-made holder and exposed to a uniform light source at normal incidence and located at a distance of about 15 cm. The reflected light spectra were recorded at angles θ_m from 20 to 60° with respect to the normal of the top surface of the sample (see Fig. 5.11).

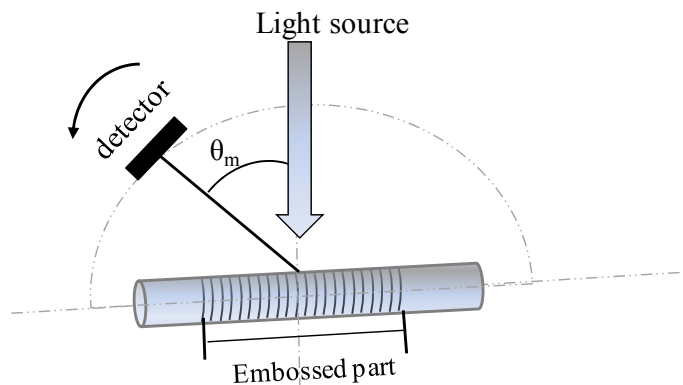


Figure 5.11: The experimental setup for measuring the reflection spectra. The sample is illuminated by a light source at normal incidence.

5.3.2 Results and discussion

A conventional melt-spun polyester (PET) monofilament was produced with a Young's modulus of approximately 4~8 GPa (see Table 5.1). For reference purposes, the fibres were post-annealed at a fixed length which increased the stiffness to 6~9 GPa, which is probably due to post-crystallisation effects.^{16, 17} Subsequently, a thin coating of the photopolymer mixture was applied to the monofilament fibres using a volatile solvent and an air brush. Typically, fibres with a core diameter of $185 \pm 15 \mu\text{m}$ with a thin coating of the photopolymer (thickness: $12 \pm 1 \mu\text{m}$) were obtained. The coated PET fibre as a composite has a similar modulus of 6~9 GPa as the post-annealed PET fibre. Apparently, the comparatively small fraction of cladding material does not influence the modulus of the coated fibre significantly.

Table 5.1: *Modulus comparison of original PET fibre, annealed PET fibre, coated fibre without a relief structure and structured fibre*

Sample	Original PET fibre	Annealed PET fibre*	Coated fibre**	Structured fibre***	
				8 μm	1 μm
Modulus (GPa)	4~8	6~9	6~9	5~8	5~8

*: For reference purposes, the PET fibres were post-annealed at 80 °C and 130 °C at a fixed length and exposed using a UV lamp at RT.

** : For reference purposes, the coated PET fibres were also post-annealed at 130 °C at a fixed length and cured using a UV lamp at RT.

***: The fibres were photoembossed at 130 °C.

Photoembossing via interference pulsed holography was applied to the bi-component fibre. A grating structure is formed on the surface of the fibre. Within the experimental error, the structured PET fibre has the similar modulus as the coated PET fibre without a relief structure (see Table 5.1.). The grating structures on the fibres were investigated using scanning electron microscopy (SEM) and are shown in Fig. 5.12. A grating structure is formed on the exposed side of the bi-component fibre while no grating structure is found on the non-exposed side of

the bi-component fibre. That might be due to the absorption of UV light by the core fibre or the lense effect induced by the refractive index changes while the interfering beams pass through the fibre. A fully structured fibre could be obtained by a multi-exposure covering the whole fibre surface. The relief height depends on the processing conditions and grating pitches. For the grating structure of $8\ \mu\text{m}$, the relief height is in the optimum conditions (see experimental part) approximately $900\sim 1300\ \text{nm}$. For the grating structure of $1\ \mu\text{m}$, the relief height reached was $60\sim 110\ \text{nm}$ in the optimum conditions. The rather large scatter in the height of the relief structures is probably related to the inhomogeneities in the core fibre or coating.

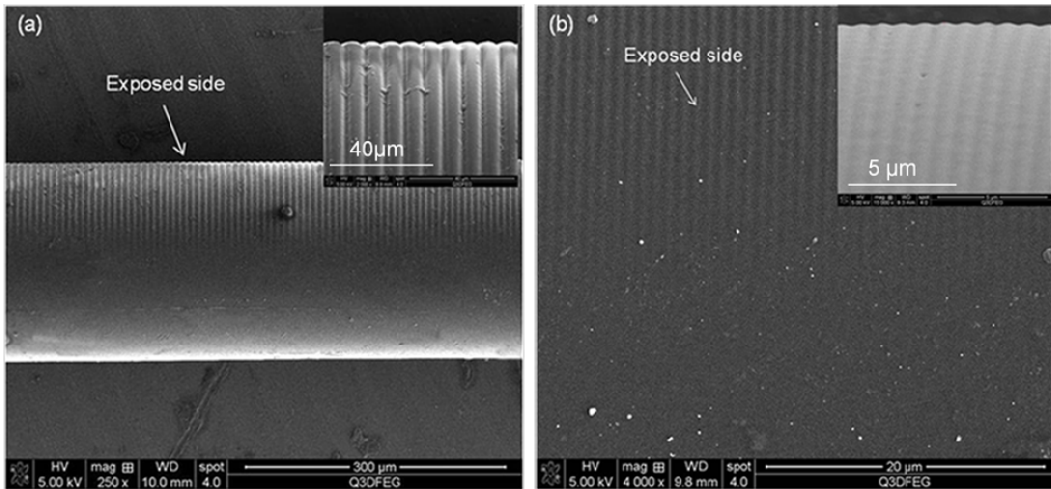


Figure 5.12: SEM images of the photoembossed bi-component fibre: a) $\Lambda = 8\ \mu\text{m}$ and (b) $\Lambda = 1\ \mu\text{m}$.

As mentioned before, white light incidence is diffracted towards the viewer at different angles by the grating structure. To investigate the angular-dependent visual effect of fibres, the photoembossed fibre with a surface grating structure of $1\ \mu\text{m}$ was illuminated by a light source at normal incidence and the reflected spectra were recorded at angles θ_m with respect to the normal of the top surface of fibre by using Autronic system. The result is shown in Fig. 5.13. The colour shift to the large wavelength is observed when θ_m increases. The central part of the

fibre with the relief structures of $1\ \mu\text{m}$ shows separated colours (red, green and blue) at different viewing angles (approximately 45° , 35° , 30° , respectively), while the two ends of the fibre without grating structure are transparent (see Fig. 5.14).

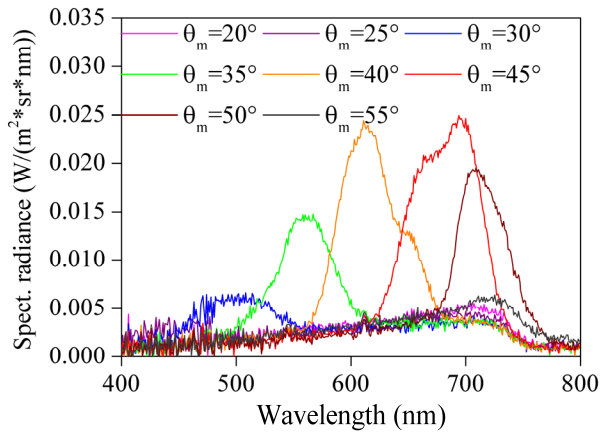


Figure 5.13: The reflected light power of photoembossed fibre with surface grating structure of $1\ \mu\text{m}$ illuminated by a light source at normal incidence and measured at angles between 20 - 55° .

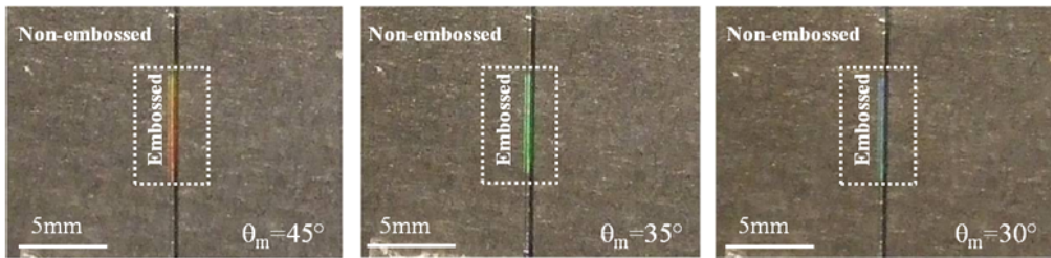


Figure 5.14: Photographs of photoembossed fibre with surface grating structure of $1\ \mu\text{m}$, showing red, green and blue at different viewing angles, approximately 45° , 35° , 30° , respectively.

In contrast, the fibres with a surface-relief grating with a pitch of $8\ \mu\text{m}$ exhibit a certain visual effect, but the different diffracted colours at the slightly different viewing angles are hard to detect (see Fig. 5.15). This is consistent with the theoretical analysis according to the grating equation as mentioned in Chapter 2.

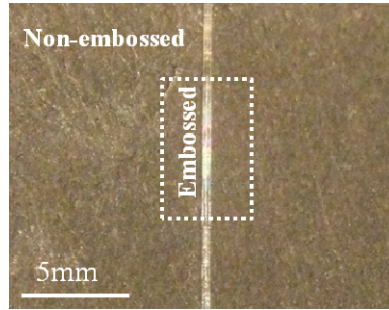


Figure 5.15: Photographs of photoembossed fibre with surface grating structure of $8\ \mu\text{m}$ under ambient light.

5.4 Conclusions

In this chapter, surface structuring of fibres was investigated. It is demonstrated that photoembossing can be used as a method to create relief structures on the surface of fibres perpendicular to the fibre axis.

To investigate whether the photopolymer mixture can be used in spinning operations, the rheological properties of the photopolymer mixture were studied. It is shown that the photopolymer mixture has viscoelastic properties and exhibits shear thinning behaviour. Photopolymer fibres were produced and photoembossed using a photo-mask. The results show that relief structures were formed on both top and bottom surfaces of fibres. The relief height of the surface structures strongly depends on the grating pitches of the relief structures. As for the smaller pitches, lower relief height is obtained. It is also found that the structured fibres do not have good mechanical properties, which is mainly due to the crosslinked system obtained after photoembossing.

To get high performance fibres with surface-relief gratings, so-called bi-component fibres were prepared by coating a high-modulus core fibre with a functional photopolymer. A small-size grating structure was created on the surface of the bi-component fibres, which is perpendicular to fibre axis. High-temperature photoembossing via pulsed holography was utilised to enhance the

height of surface gratings. Consequently, it is found that the fibres with a grating structure of 1 μm exhibit a strong angular-dependent visual effect. Separated diffracted colours (red, green, blue) are observed at different viewing angles. In contrast, the fibres with a grating structure of 8 μm exhibit different diffracted colours only at slightly different viewing angles.

5.5 References

1. F. T. O'Neill, I. C. Rowsome, A. J. Carr, S. M. Daniels, M. R. Gleeson, J. V. Kelly, J. R. Lawrence and J. T. Sheridan, *Opto-Ireland 2005: Photonic Engineering*, 2005, **5827**, 445-456.
2. A. Liedtke, C. H. Lei, M. O'Neill, P. E. Dyer, S. P. Kitney and S. M. Kelly, *Acs Nano*, 2010, **4**, 3248-3253.
3. C. Sanchez, B. J. de Gans, D. Kozodaev, A. Alexeev, M. J. Escuti, C. van Heesch, T. Bel, U. S. Schubert, C. W. M. Bastiaansen and D. J. Broer, *Adv Mater*, 2005, **17**, 2567-2571.
4. N. Adams, B. J. de Gans, D. Kozodaev, C. Sanchez, C. W. M. Bastiaansen, D. J. Broer and U. S. Schubert, *J Comb Chem* 2006, **8**, 184-191.
5. K. Hermans, C. W. M. Bastiaansen, D. J. Broer and J. Perelaer, Int. Pat., WO 2008025508, 2008.
6. K. Hermans, M. van Delden, C. W. M. Bastiaansen and D. J. Broer, *J Micromech Microeng*, 2008, **18**, 095022.
7. K. Hermans, F. K. Wolf, J. Perelaer, R. A. J. Janssen, U. S. Schubert, C. W. M. Bastiaansen and D. J. Broer, *Appl Phys Lett*, 2007, **91**, 174103.
8. B. J. de Gans, C. Sanchez, D. Kozodaev, D. Wouters, A. Alexeev, M. J. Escuti, C. W. M. Bastiaansen, D. J. Broer and U. S. Schubert, *J Comb Chem*, 2006, **8**, 228-236.
9. S. Liu, M. R. Gleeson, J. X. Guo and J. T. Sheridan, *Macromolecules*, 2010, **43**, 9462-9472.

10. K. Hermans, I. Tomatsu, M. Matecki, R. P. Sijbesma, C. W. M. Bastiaansen and D. J. Broer, *Macromol Chem Physic*, 2008, **209**, 2094-2099.
11. K. Hermans, S. Z. Harnidi, A. B. Spoelstra, C. W. M. Bastiaansen and D. J. Broer, *App Opt*, 2008, **47**, 6512-6517.
12. M. van Gulp and J. Palmen, *Rheol Bull*, 1998, **67**, 5-8.
13. T. Nakagawa, *Bull Cheml Soc Jpn*, 1952, **25**, 88-93.
14. T. Nakagawa, *Bull Cheml Soc Jpn*, 1952, **25**, 93-97.
15. O. T. Picot, R. Alcalá, C. Sánchez, M. Dai, N. F. Hughes-Brittain, D. J. Broer, T. Peijs and C. W. M. Bastiaansen, *Macromol Mater Eng*, 2012, **298**, 33-37.
16. F. S. Smith and R. D. Steward, *Polymer*, 1974, **15**, 283-286.
17. P. N. Peszkin, J. M. Schultz and J. S. Lin, *J Polym Sci Part B: Polym Phys*, 1986, **24**, 2591-2616.

6 Humidity Responsive Bilayer Actuator via Bending*

6.1 Introduction

In the former chapters the decoration of fibres with interference patterns was discussed to enhance the visual effects of textiles. The second topic that is discussed in this thesis is the introduction of stimuli-responsiveness into the textiles with the aim to improve wearing performance and comfort of clothing. For this purpose a single fibre that can deform in response to a stimulus from the environment is investigated. As a result, it is anticipated that the textiles produced from these fibres will respond to the same stimulus as well. Stimuli-responsive polymers are a class of materials to produce such responsive fibres since they can generate large mechanical actuation in response to a change in the environment. So far, liquid crystal elastomers that can deform in response to the external factor changing the order parameter have been utilised to spin fibres.¹⁻⁴ However, these liquid crystal elastomer fibres have low modulus, which is not applicable in most of textiles applications.

In this thesis, it is proposed to use a bi-component fibre system that consists of

*This chapter is reproduced in part with permission from *ACS Appl Mater Inter*:

M. Dai, O. T. Picot, J. M. N. Verjans, L. T. de Haan, A. P. H. J. Schenning, T. Peijs and C. W. M. Bastiaansen, *ACS Appl. Mater. Inter.*, **2013**, 5(11), 4945-4950. Copyright ©2013 American Chemical Society.

a core fibre and a stimuli-responsive polymer coating based on a liquid crystalline (LC) network. The core fibre is only half coated instead of fully coated (see Fig. 6.1) to get the responsiveness. Common natural or synthetic fibres can be utilised as core fibres since they are cheap and can provide the mechanical stability. Another important advantage is that fibres usually consist of oriented polymers, which in turn can align the LC mesogens.^{5, 6} Therefore, a well-aligned LC polymer coating can be formed on the surface of the core fibre and the obtained bi-component fibre is anticipated to exhibit the desired response to an external trigger.

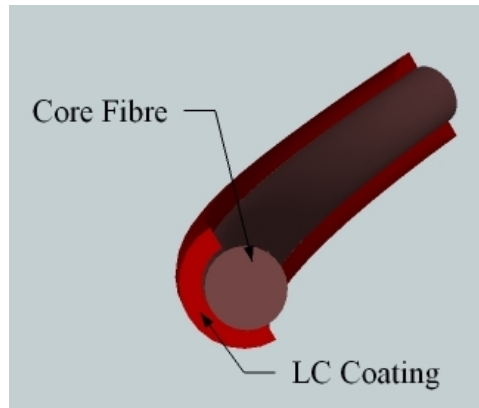


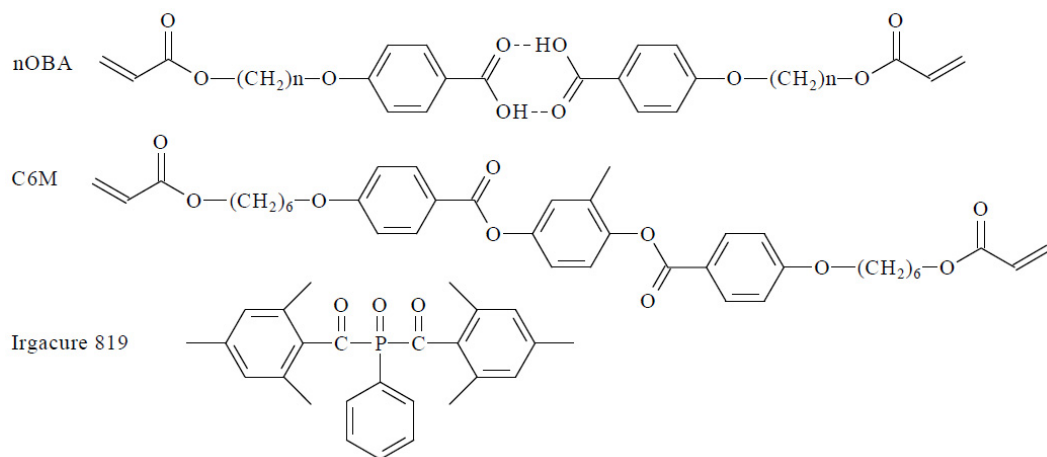
Figure 6.1: A bi-component fibre consisting of core fibre and LC coating.

Because humidity is variable in nature, humidity responsive polymer actuators are receiving a lot of attention for personal comfort, health, and industrial and technological applications.⁷⁻¹⁰ In this thesis, the prime objective is to make textile fibres that respond to humid conditions. Thus breathable textiles can be produced from these fibres that respond to the humidity changes. This kind of smart textiles can be utilised to produce sport clothing to improve the wearing performance. To simplify the system, a bilayer tape is investigated, in which one layer is a humidity responsive LC polymer coating and the other layer is a uniaxially oriented polyamide-6 as is often used in textiles. A well-aligned LC coating can be formed on the oriented polymer substrate to obtain a humidity responsive

bilayer actuator.

6.2 Humidity Responsive LC polymer

The humidity responsive LC polymer utilised in our bilayer actuator is based on a self-assembled supramolecular network consisting of covalent crosslinks and hydrogen-bonded crosslinks. The monomers used in this work are not liquid crystalline by themselves. But they are capable to pair under the formation of hydrogen bonds to form the rod-like conformation that is necessary to induce a liquid crystalline behaviour.¹¹⁻¹³ Scheme 6.1 shows the chemical structures of monomers (nOBA) utilised in this thesis. Usually the monomer nOBA is utilised as a mixture of three homologues with different aliphatic acid lengths ($n = 3, 5$ and 6) in a weight ratio of 1:1:1 to generate a low crystallisation temperature and a broad temperature range in which the mixture exhibits a nematic phase.¹⁴ The photoinitiator Irgacure 819 is added for the photopolymerisation and a covalent crosslinker C6M is used for mechanical stability (Scheme 6.1).¹⁴⁻¹⁶



Scheme 6.1: Chemical structures of the components of the LC mixture.

The nematic order can be efficiently maintained in the network by photopolymerising the monomers while they are in the nematic phase. The formed

hydrogen bonds are sufficiently strong to withstand immersion in water without significant deformation. To activate the system, the hydrogen bonds have to be broken, which requires a reaction with a base. The network is converted into a polymer salt and becomes much more hygroscopic and it exhibits anisotropic swelling under humid conditions. Fig. 6.2 displays the response of a uniaxially aligned film ($\sim 18 \mu\text{m}$ thick) which was prepared by using anti-parallel aligned cells (INTEC, US) and activated with 0.1M NaOH upon fully immersion in water, perpendicular and parallel to the director. Additional information regarding the preparation of the LC film and expansion measurement is available in Appendix A. The film swells upon immersion in water. It exhibits a significantly larger expansion in the direction perpendicular to the director than parallel to the director.

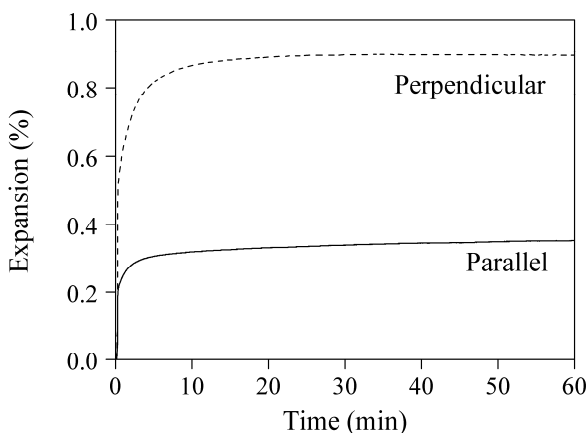
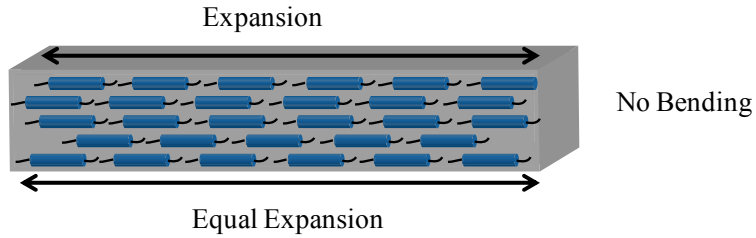


Figure 6.2: Response of a uniaxially aligned film upon immersion in water. Samples are treated with 0.1M NaOH for 25 s. The expansion curves were generated by immersing clamped activated film in water at time $t=0$ and subsequently measuring the length of the sample parallel and perpendicular to the alignment direction, respectively.

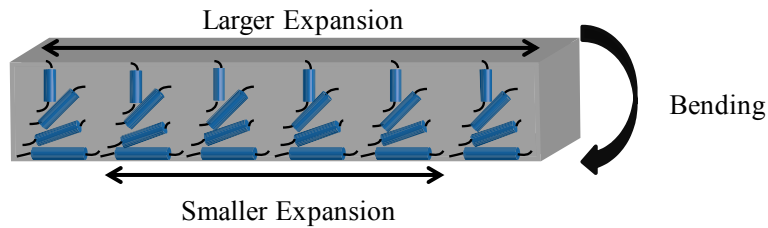
This anisotropic expansion under humid conditions allows different macroscopic deformations by designing specific director orientation profile throughout the film. As shown in Fig. 6.3, in a uniaxial planar configuration, (in-plane) expansions at two surfaces are balanced and no bending occurs. On the

other hand, the mismatch of (in-plane) expansion at the two surfaces results in the bending deformation out of the plane of film. This is achieved in two configurations, including splayed (the director moves between the planar and homeotropic boundary conditions) and twisted nematic (the director in-plane rotates 90° within the sample) configurations.¹⁴

(a) Uniaxial Planar



(b) Splayed



(c) Twisted nematic

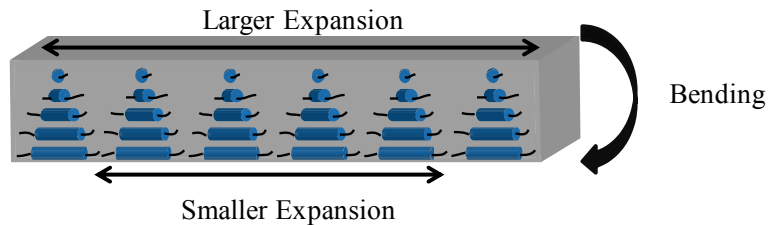


Figure 6.3: Director profiles and the corresponding deformations under humid condition.¹⁴

In this thesis, the above-described humidity responsive LC polymer network is utilised to create a bilayer actuator based on an oriented polyamide-6 substrate. The macroscopic motion induced by the director profile in the LC network contributes to the deformation of the bilayer system. The detailed humidity responsive deformation of the bilayer actuator is discussed in this chapter.

6.3 Experimental

Materials: The monomers nOBA ($n = 3, 5,$ and 6) (see Fig. 6.1) were obtained from SYNTHON Chemicals (Germany) and mixed in the weight ratio of 1:1:1. The mesogen C6M was obtained from Merck (Germany). The photo-initiator Irgacure 819 was obtained from CIBA Specialty Chemicals (Germany). The uniaxially stretched PA-6 tapes (thickness: $15\ \mu\text{m}, 25\ \mu\text{m}$) were obtained from Goodfellow (UK).

Fabrication of bilayer humidity responsive system: The LC mixture contains 86 wt% nOBA, 12 wt% C6M and 2 wt% Irgacure 819. It was found by DSC measurement that the nematic phase of the mixture was between $56\ ^\circ\text{C}$ and $95\ ^\circ\text{C}$, which is close to the results shown in literature.¹⁴ The mixture was mixed with the solvent xylene in weight ratio of 1:5 at $100\ ^\circ\text{C}$ and sprayed using an airbrush onto the surface of the stretched PA-6 tape to form a thin uniform coating. After spraying, the sample was heated at $110\ ^\circ\text{C}$ to evaporate the solvent. Then, the sample was cooled down and polymerised using a UV Exfo Mercury lamp at $85\ ^\circ\text{C}$ in the nematic phase of the mixture. After cooling to RT, the sample was treated in a 0.1M NaOH solution for 25 s to break the hydrogen bonds. Finally, a bilayer humidity responsive system was obtained. The whole procedure is shown in Fig. 6.4.

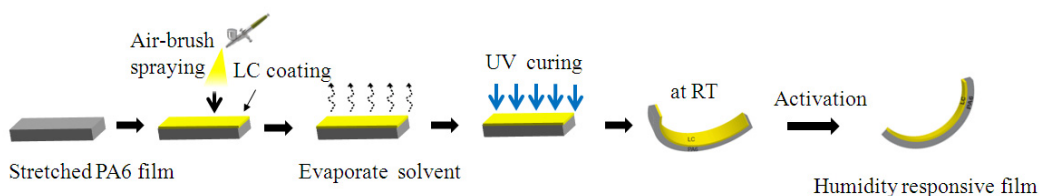


Figure 6.4: Schematic representation of the fabrication process of the humidity responsive bilayer polymer actuator.

To characterise the isolated LC coating, the LC coating with the substrate was UV-glued to a glass slide, then the PA-6 substrate was peeled off. Consequently, a

LC coating on a glass slide was obtained.

Humidity response of the activated bilayer polymer actuator: The activated bilayer polymer actuator was exposed to a gradient in water vapour. The images of the sample were taken every 5 s using a camera.

To investigate the humidity responsive deformation of the bilayer polymer actuators in a spatially homogeneously humid air environment, a homemade humidity chamber was utilised, which is basically made up by a plastic container (~25 cm × 40 cm). The plastic container has two entries equipped with two tubes that are connected to dry nitrogen and humid nitrogen, respectively. To obtain humid nitrogen, a special cylindrical glassware (diameter: ~10 cm; height: ~20 cm) was made that contains water. The glassware is enclosed to prevent water evaporation. As shown in Fig. 6.5, there are two interconnected tubes (A & B) inside the glassware and incorporated into the same piece of the glassware. The two tubes are filled with water through which nitrogen is passed. As the nitrogen is fed through, it becomes more humid and is sent into the container. By adjusting the ratios of dry and humid nitrogen, a spatially homogeneous humid nitrogen environment is obtained in the container. The samples were placed inside this humidity chamber to study their deformation in response to the relative humidity (R.H.). The images of the samples under different R.H. were taken using a camera and used to measure the bending radii of the samples. The relative humidity is measured with a humidity/temperature sensor (Vaisala, Finland).

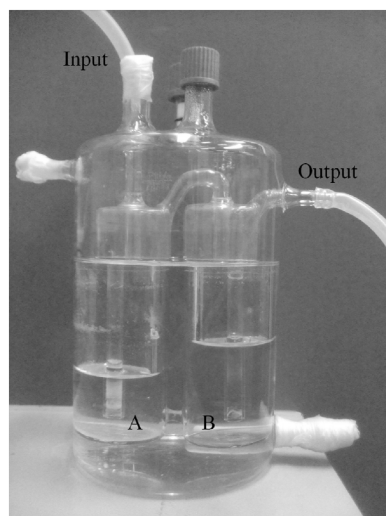


Figure 6.5: *Photography of the glassware used to get humid nitrogen.*

Characterisation: The optical anisotropy of the pure LC coating was examined by a Leica DM6000 polarised optical microscope (POM) between two crossed polarisers prior to activation.

Attenuated total reflectance (ATR) infrared spectra were measured with a VARIAN 670 IR spectrometer with a slide-on ATR accessory and a germanium (Ge) crystal was used. Approximately the penetration depth is $<1 \mu\text{m}$. The sample was positioned with the stretching direction parallel and perpendicular to the polarisation direction of the infrared beam to obtain polarised ATR spectra, respectively. To check whether the hydrogen bonds are completely broken, the absorbance spectra of the LC coating on the sample were recorded respectively before and after activation in the alkaline solution using the same IR spectrometer.

The measurement of the thickness of the LC coating was carried out using a FEI Quanta 3D Scanning Electron Microscope. To prevent charging in the electron beam, a thin gold layer was coated on the cross section of the bilayer tape by vapour deposition.

6.4 Results and Discussion

A thin layer ($\sim 4 \mu\text{m}$) of the LC mixture is spray-coated on the surface of the uniaxially stretched PA-6 tape and then polymerised in the nematic phase at 85°C using a UV Exfo Mercury Lamp. After polymerisation and cooling down to room temperature, a pre-bent tape with a curvature $1/r$ (r is the bending radius) is obtained in which the PA-6 substrate is always on the outside of the curvature. Probably, this bending of the tape originates from the polymerisation shrinkage of the LC network.¹⁷ Subsequently the tape is dipped in the NaOH solution for activation and dried. Again a pre-bent bilayer polymer is obtained (see Fig. 6.6) with the bending direction similar to the direction before the base treatment.

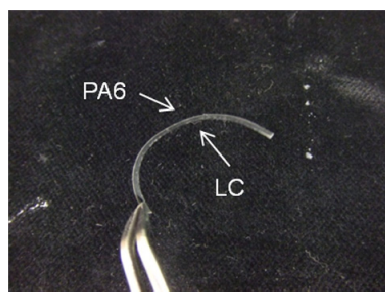


Figure 6.6: Image of a bent bilayer actuator containing a $25\text{-}\mu\text{m}$ -thick PA-6 layer and a $4\text{-}\mu\text{m}$ -thick LC polymer salt layer at ambient conditions at RT.

The response of the activated bilayer polymer actuator to a gradient in humidity (or water vapour) is shown in Fig. 6.7. It is found that the bending curvature decreases with increasing humidity and that the bilayer responds to changes in humidity within seconds.

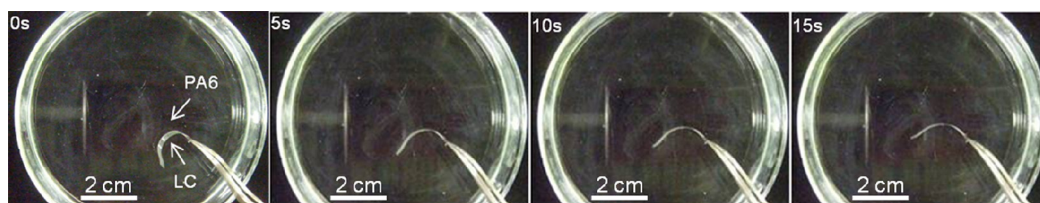


Figure 6.7: Humidity responsive behaviour of the activated bilayer actuator ($25\text{-}\mu\text{m}$ -thick PA-6 substrate and $4\text{-}\mu\text{m}$ -thick LC coating) after exposure to water vapour.

The deformation of the bilayer polymer actuator (PA-6 of 15 μm thick and LC coating of 4 μm thick, one end is fixed, the other end is free-standing) was investigated in more detail in a homemade humidity chamber in a spatially homogeneous humid air environment. The curvature of the bilayer tape at equilibrium as a function of the relative humidity (R.H.) shows a high curvature κ equal to $1/r$ at low R.H. and is bent with the PA-6 substrate on the outside of the curvature (Fig. 6.8). Upon increasing the R.H., the curvature decreases and the bilayer tape bends less resulting in a flatter bilayer actuator. To estimate the reproducibility, the experiment was cycled a number of times between the low R.H. and high R.H. (Fig. 6.8). The results indicate that the bending motion is reversible and repeatable.

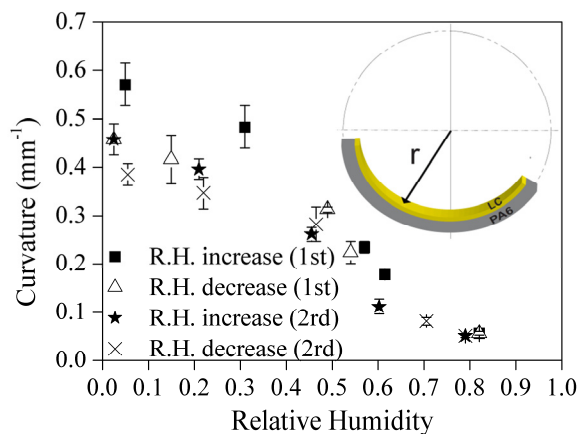


Figure 6.8: Curvature of a bilayer tape as a function of the relative humidity. The insert illustrates the bending radius r defined for the bilayer tape.

The influence of the substrate thickness (t) on the bending behaviour of the bilayer tape was also studied (Fig. 6.9). A comparison was made between a bilayer tape **I** (PA-6: $t=25 \mu\text{m}$, LC coating: $t=4 \mu\text{m}$) and a bilayer tape **II** (PA-6: $t=15 \mu\text{m}$, LC coating: $t=4 \mu\text{m}$). For reference purposes, the response of a pure single PA-6 tape **III** ($t=25 \mu\text{m}$) to the relative humidity was also studied. It is found that the pure single PA-6 tape **III** does not respond to variations in humidity

in a bending mode deformation. The bilayer tapes **I** and **II** both show a bending-mode deformation under humid conditions and the bending curvature of the bilayer tape **I** is smaller than that of the bilayer tape **II**. Of course, this is to be expected because the bending moment of the PA-6 substrate increases substantially with increasing thickness.¹⁸

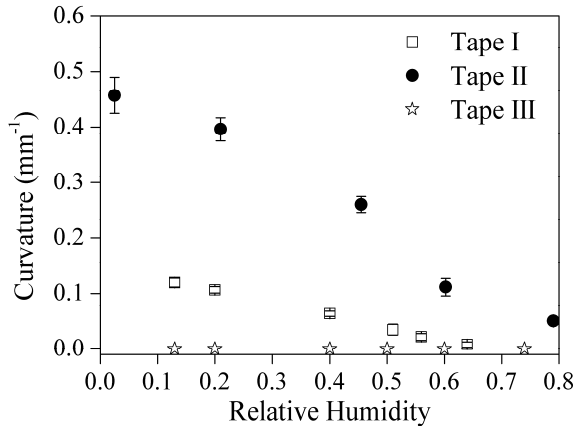


Figure 6.9: *Curvature of the bilayer tapes as a function of the relative humidity in the second running.*

To determine the bending mechanism of this humidity responsive bilayer actuator, the alignment of the isolated LC coating was first investigated prior to activation by separating it from its substrate. POM images recorded between two crossed linear polarisers (see Fig. 6.10) show that when the LC coating is positioned with the stretching direction (of the PA-6 substrate) parallel/perpendicular to the polariser axis, a homogeneous dark state is observed. When the LC coating is oriented with the stretching direction at approximately 45° to the polariser axis, a bright state is observed. This indicates the LC mesogens are well aligned, and a mono-domain LC coating is obtained.

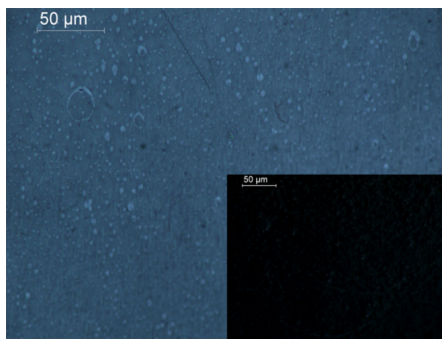


Figure 6.10: POM image of LC coating between crossed polarisers with the stretching direction of initial PA-6 substrate oriented at $\sim 45^\circ$ to the polariser axis. The inset is a POM image of LC coating between crossed polarisers with the stretching direction of the sample parallel or perpendicular to the polariser axis.

The optical anisotropy in the surface region of the pure LC coating prior to activation was also examined by ATR-IR spectroscopy. It has been reported that polarised ATR can be used to study the molecular orientation near the surface of the polymer substrates.¹⁹⁻²¹ The polarised ATR spectrum shows a band at 1729 cm^{-1} which is assigned to the stretching vibration of carbonyl groups attached to the polymer backbone and shows no anisotropy in the spectra (Fig. 6.11). The band at 1682 cm^{-1} originates from the asymmetric stretching vibration of the carbonyl groups of the cyclic dimer. The bands at 1255 and 1165 cm^{-1} are due to the C-O-C asymmetric stretching vibration. The bands associated with the stretching vibrations of the benzene rings occur at 1606 , 1580 , 1511 and 1422 cm^{-1} , which are usually used to determine the orientation of the mesogens.^{19, 20} Considering the intensity at 1729 cm^{-1} as the same in each spectrum, it is clearly indicated that the bottom surface of the LC coating, which is attached to the substrate and was removed from the substrate has a high dichroism around 1606 cm^{-1} which originates from the stretching vibration of benzene rings. The dichroic ratio D can be calculated from the polarised ATR spectra by the relation:²¹

$$D = \frac{A_{//}}{A_{\perp}} \quad (6.1)$$

where $A_{//}$ and A_{\perp} are the ATR spectra in absorbance for the sample positioned

with the stretching direction parallel and perpendicular to the polarisation direction of the infrared beam, respectively. The dichroic ratio of the bottom surface is ~ 5.6 . On the other hand, the top layer of LC coating shows a relatively low dichroism at 1606 cm^{-1} and the average dichroic ratio D is ~ 2.8 . The order parameter S can be calculated from the dichroic ratio by the relation:²¹

$$S = \frac{D-1}{D+2} \quad (6.2)$$

As for the top layer, the order parameter S is approximately 0.6 while the order parameter of the bottom layer is approximately 0.37. This indicates that a splayed alignment (bottom surface having parallel alignment and top surface having close to homeotropic alignment with a tilt) of the LC was obtained on the PA-6 substrate. This splayed configuration is expected to enhance a bending deformation.

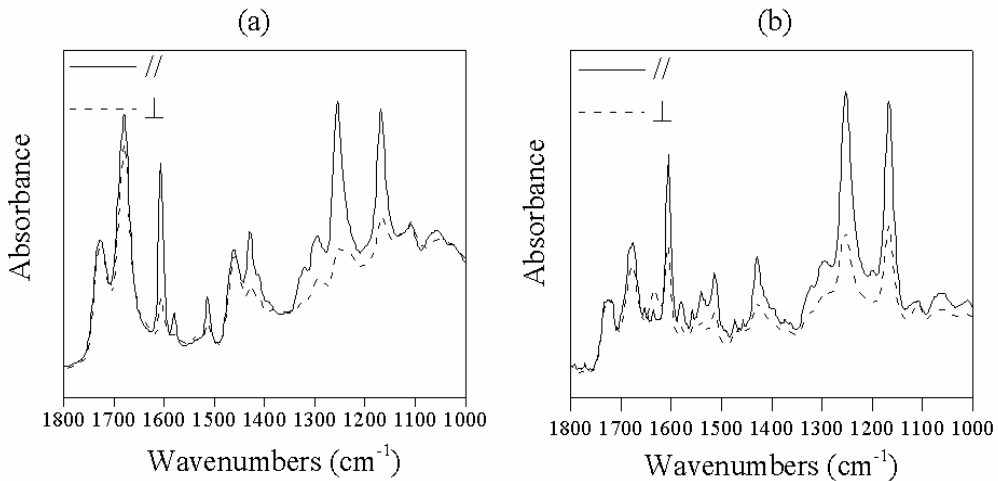


Figure 6.11: Polarised ATR spectra of the LC coating. (a) bottom surface of the LC coating attached to the substrate, (b) top surface of the LC coating exposed to air.

To check whether the H-bonds in the LC network are completely broken after activation with NaOH, both sides of the LC coating, i.e. the top surface and the bottom surface that is attached to the substrate, were investigated by FTIR measurement in reflection. The FTIR spectra (see Fig. 6.12) indicate that, after

activation, the absorption peak at 1682 cm^{-1} for the top surface has completely disappeared which indicates that the hydrogen bonds are completely broken.¹² However, for the bottom surface, the absorption peak at 1682 cm^{-1} still exists, which means that H-bonds in the LC network are not completely eliminated. This is probably due to diffusion limitations of the alkaline solution into the bottom surface of the LC network. In other words, it is assumed that the PA-6 substrate restricts diffusion of the alkaline solution into the LC coating and a sodium salt gradient is generated.²²

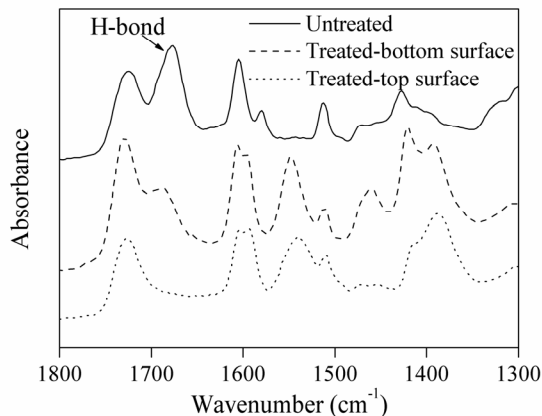


Figure 6.12: FTIR spectrum of the LC coating before and after activation. The top surface is the surface of the LC coating exposed to air and the bottom surface is the surface of the LC coating attached to the substrate.

Based on these data, the bending motion of the humidity responsive bilayer actuator could be due to one or several parameters (see Fig. 6.13), such as the expansion difference between the LC polymer layer and substrate PA-6, the splay alignment of the LC network and the sodium salt gradient in the LC network. When the humidity increases, the LC polymer layer exhibits a larger expansion than the substrate, leading to the unbending of the bilayer actuator since the bilayer actuator is pre-bent with the PA-6 substrate on the outside of the curvature. The LC network exhibits a significantly larger expansion in the direction perpendicular to the director than parallel to the director, thus the director rotation

profile in the network results in the mismatches of (in-plane) expansion at the two surfaces (top and bottom) of the LC polymer layer, which force the bending deformation towards the bottom surface of the LC polymer layer. Besides, the sodium salt gradient in the LC network also results in the larger expansion at the top surface and smaller (or even no) expansion at the bottom surface of the LC polymer layer. All of these parameters contribute to the unbending of the bilayer actuator. At the moment, the exact or dominant mechanism of the deformation of the bilayer actuator has not been determined yet.

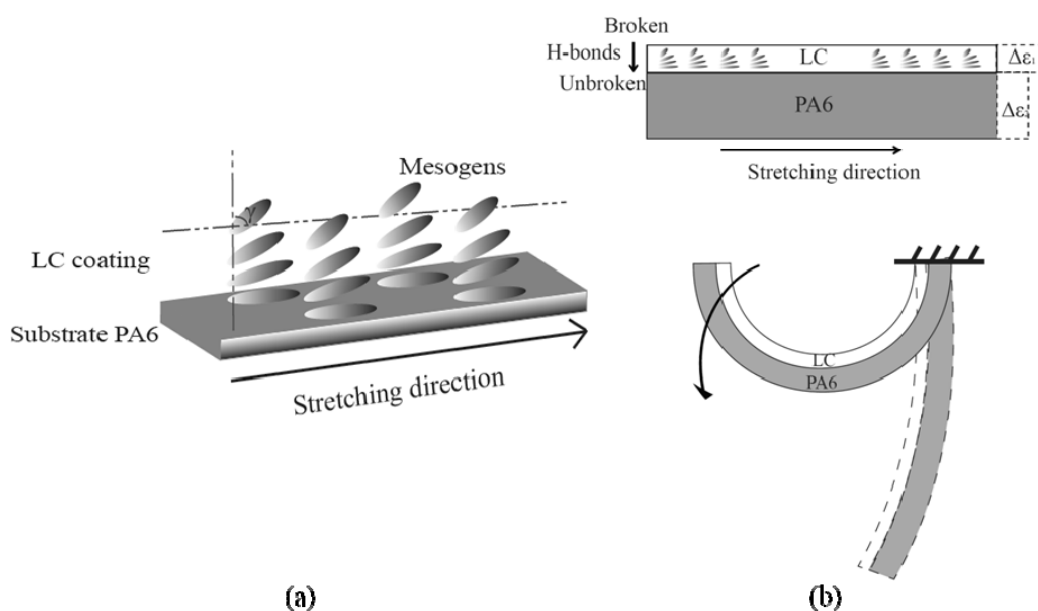


Figure 6.13: (a) Schematic illustration of the splay-aligned LC coating on the substrate PA-6. (b) Schematic representation of a humidity responsive bilayer tape. The LC coating shows splay alignment and has a H-bonds gradient from the top to bottom in the network. Under the humid conditions, the LC coating has a larger expansion than the PA-6. The bilayer tape exhibits less bending.

6.5 Conclusions

In this chapter, it is demonstrated that a humidity responsive bilayer polymer actuator can be fabricated, which consists of an oriented PA-6 substrate and a splayed-aligned H-bonded LC coating. After the hydrogen bonds are broken, the

bilayer tape acts as a humidity actuator that responds to the humidity changes with a bending-mode deformation. At high humidity the actuator is relatively straight while at low humidity the polymer bends. It is found that the splay-alignment of the LC network, the hydrogen bonds gradient in the LC network and expansion difference between the LC network and the polyamide-6 contribute to the bending deformation of the bilayer system.

6.6 References

1. H. J. Choi, K. U. Jeong, L. C. Chien and M. H. Lee, *J Mater Chem*, 2009, **19**, 7124-7129.
2. S. V. Ahir, A. R. Tajbakhsh and E. M. Terentjev, *Adv Funct Mater*, 2006, **16**, 556-560.
3. J. Naciri, A. Srinivasan, H. Jeon, N. Nikolov, P. Keller and B. R. Ratna, *Macromolecules*, 2003, **36**, 8499-8505.
4. T. Kaneko, K. Yamaoka, Y. Osada and J. P. Gong, *Macromolecules*, 2004, **37**, 5385-5388.
5. H. Fujikake, M. Kuboki, T. Murashige, H. Sato, H. Kikuchi and T. Kurita, *J Appl Phys*, 2003, **94**, 2864-2867.
6. H. Aoyama, Y. Yamazaki, N. Matsuura, H. Mada and S. Kobayashi, *Mol Cryst Liquid Cryst*, 1981, **72**, 127-132.
7. J. L. Hu, H. P. Meng, G. Q. Li and S. I. Ibekwe, *Smart Mater Struct*, 2012, **21**, 053001.
8. K. M. Holder, M. A. Priolo, K. E. Secrist, S. M. Greenlee, A. J. Nolte and J. C. Grunlan, *J Phys Chem C*, 2012, **116**, 19851-19856.
9. Y. H. Ma, S. G. Ma, T. L. Wang and W. L. Fang, *Sens Actuat A-Phys*, 1995, **49**, 47-50.
10. N. Yamazoe and Y. Shimizu, *Sensor Actuator*, 1986, **10**, 379-398.
11. C. M. Paleos and D. Tsiourvas, *Liq Cryst*, 2001, **28**, 1127-1161.
12. S. K. Kang and E. T. Samulski, *Liq Cryst*, 2000, **27**, 371-376.

13. S. K. Kang, E. T. Samulski, P. Kang and J. Choo, *Liq Cryst*, 2000, **27**, 377-385.
14. K. D. Harris, C. W. M. Bastiaansen and D. J. Broer, *J Microelectromech Syst*, 2007, **16**, 480-488.
15. K. D. Harris, C. W. M. Bastiaansen, J. Lub and D. J. Broer, *Nano Lett*, 2005, **5**, 1857-1860.
16. K. D. Harris, C. W. M. Bastiaansen and D. J. Broer, *Macrom Rapid Comm*, 2006, **27**, 1323-1329.
17. R. A. M. Hikmet, B. H. Zwerver and D. J. Broer, *Polymer*, 1992, **33**, 89-95.
18. S. Timoshenko, *J Opt Soc Am*, 1925, **11**, 233-255.
19. M. Kondo, J. Mamiya, M. Kinoshita, T. Ikeda and Y. L. Yu, *Mol Crystals Liq Crystals*, 2007, **478**, 245-257.
20. E. Anglaret, M. Brunet, B. Desbat, P. Keller and T. Buffeteau, *Macromolecules*, 2005, **38**, 4799-4810.
21. T. A. Huy, T. Luepke and H. J. Radusch, *Journal of Applied Polymer Science*, 2001, **80**, 148-158.
22. Longer exposure time to completely break the H-bonds results in a brittle LC coating.

7 Humidity Responsive Bilayer Actuator via Curling

7.1 Introduction

In the previous chapter, a bilayer actuator based on a splay-aligned LC network and a uniaxially oriented polyamide-6 substrate was fabricated which exhibits a bending-deformation in response to the humidity changes. In order to get a larger mechanical actuation, a bilayer actuator that can respond to the humid condition via curling deformation is desirable.

As mentioned before, the deformation of a LC polymer actuator can be controlled by the alignment of the LC units in the network.¹ It is expected that a different deformation can be induced into the bilayer system by changing the director orientation profile of the LC network on the substrate as well, e.g. curling deformation. Previously, it was reported that a thermal responsive tape with so-called twisted-nematic configuration which is cut at 45° to the alignment direction of the surface, exhibits a curling-mode deformation.² In that case, two alignment layers were applied to induce the in-plane rotation of the LC mesogens in the network and a chiral dopant was added to control the rotation direction.

In this thesis, a bilayer system was utilised in order to get the desired mechanical stability. However, in such a bilayer system, only one layer, i.e. a uniaxially oriented PA-6, was utilised to align the LC mesogens.^{3,4} Thus, in order to induce a rotation of the LC mesogens, a chiral dopant needs to be added into

the humidity responsive LC mixture. Usually when a certain amount of the chiral dopant is added into the LC mixture, a chiral nematic phase can be formed with a helical pitch (p) (see Fig. 7.1). The helical pitch (p) of a chiral nematic phase can be calculated by:

$$p = \frac{1}{HTP \times c \times ee} \quad (7.1)$$

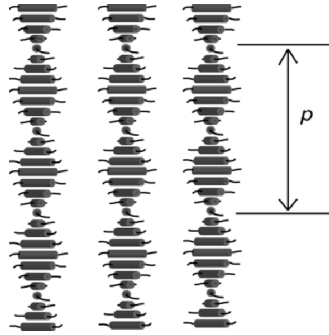


Figure 7.1: Schematic illustration of the chiral nematic alignment.

in which HTP (μm^{-1}) is the helical twisting power (ability of the dopant to induce the helical twist), c is the concentration and ee is the enantiomeric excess (ideally equal to 1).⁵ For the same LC system and chiral dopant, the HTP is constant and the helical pitch is only related to the concentration of chiral dopant. In this thesis, only a small amount of the right-handed chiral dopant LC756 (see Fig. 7.2) is added into the LC mixture. As shown in Fig. 7.3, it will induce a counter-clockwise rotation of LC mesogens in the director through the thickness of the LC coating. Eventually, after activation, the bilayer tape exhibits a humidity sensitive response through curling, which is discussed in more detail in this chapter.

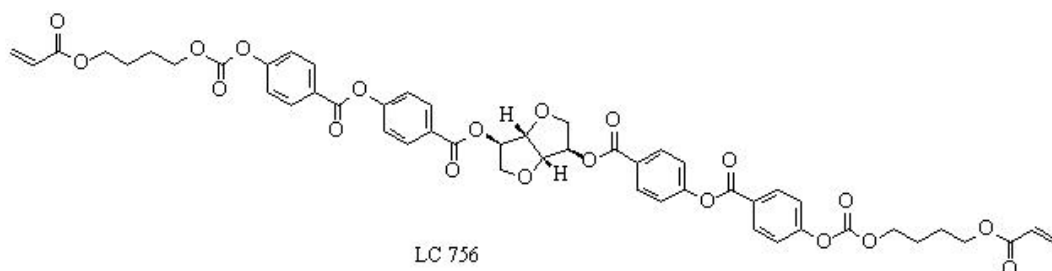


Figure 7.2: Chemical Structure of chiral dopant LC756.

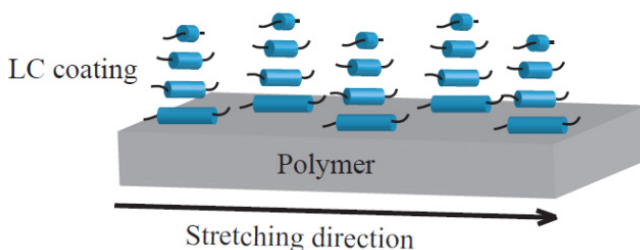


Figure 7.3: Schematic illustration of the rotation of the LC mesogens in the director through the thickness of LC coating on the PA-6 substrate.

7.2 Experimental

The LC mixture usually contains 86 wt% monomer nOBA ($n=3, 5, 6$ in weight ratio of 1:1:1, Synthion Chemicals), 12 wt% reactive mesogen C6M (Merck) and 2 wt% photo-initiator Irgacure 819 (Ciba Specialty Chemicals). Different percentages of chiral dopant LC756 (BASF) were added to induce the rotation of LC mesogen. A small amount (10^3 ppm) of surfactant (2-(*N*-ethylperfluorooctanesulfonamido) ethylacrylate) was added to obtain in-plane alignment at the air interface.⁶ The phase behaviour of the mixtures was investigated by optical polarisation microscopy and differential scanning calorimetry (DSC). The samples were mixed with the solvent xylene at 100 °C and sprayed using an airbrush onto the surface of the uniaxially stretched PA-6 tape with the thickness of 25 μm (Goodfellow, UK) to form a thin uniform coating. Obtained samples were heated at 110 °C to evaporate the solvent. Then,

the samples were cooled down and UV polymerisation was performed at 85 °C which is in the nematic phase of the mixture. To activate this bilayer system, the samples were immersed at 0.1M NaOH for 25s to break the hydrogen bonds. To check whether the H-bonds are broken, attenuated total reflectance (ATR) infrared spectra of the LC coatings before and after activation were measured using a VARIAN 670 IR spectrometer with a slide-on ATR accessory, where a germanium (Ge) crystal was used. Here both sides of the LC coating, i.e. the top surface and the bottom surface that is attached to the substrate, were investigated. Finally, a bilayer humidity responsive actuator was obtained.

The deformation of the activated bilayer actuator (2.5 mm×25 mm) (one end is fixed, the other end is free standing) in response to the relative humidity was investigated in a homemade humidity chamber with a humidity/temperature sensor. The humidity chamber consists of a plastic container (~25 cm × 40 cm) which has two openings equipped with two tubes connected to dry and humid nitrogen, respectively. By adjusting the input flow rate of the dry and humid nitrogen, respectively, a spatially homogeneous humid nitrogen environment can be created in the container.

7.3 Results

A thin layer (4~5 μm) of the LC mixture is spray-coated on the surface of a uniaxially stretched polyamide-6 tape using an airbrush. Then, it was polymerised in the nematic phase using an UV Lamp. After polymerisation, these samples were treated in the alkaline solution to break H-bonds to obtain the actuation. The FTIR measurement (see Fig. 7.4) indicates whether the hydrogen bonds are completely broken, as this is related to the absorption peak at 1682 cm⁻¹.⁷ It clearly demonstrates that on the bottom surface, hydrogen-bonds still exist. There is a hydrogen-bond gradient in the LC network, which is similar to the result shown in Chapter 6. This is probably also due to diffusion limitations of the

alkaline solution into the bottom surface of the LC network.

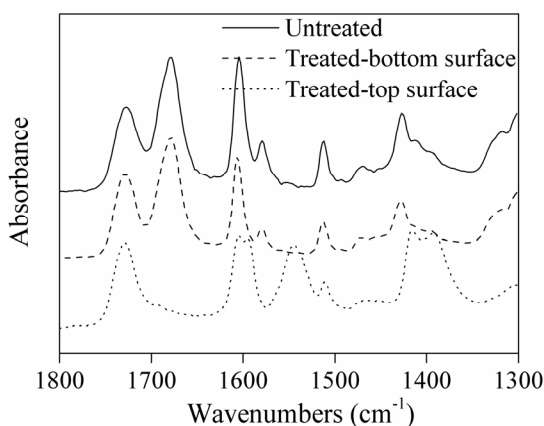


Figure 7.4: FTIR spectrum of the LC coating before and after activation. The top surface is the surface of the LC coating exposed to air and the bottom surface is the surface of the LC coating attached to the substrate.

For reference purposes, a bilayer humidity responsive actuator without any chiral dopant was produced. It is found that at room temperature and a relative humidity of $\sim 45\%$ it is pre-bent with the PA6 substrate on the outside of the curvature (see Fig. 7.5). When a small amount (0.1 wt%) of chiral dopant LC756 is added into the LC mixture, a left-handed spiral bilayer actuator with a curling pitch (S) is formed (see Fig. 7.5). It can be seen that the end-to-end distance of the curled strip is significantly reduced in comparison to the bent strip.

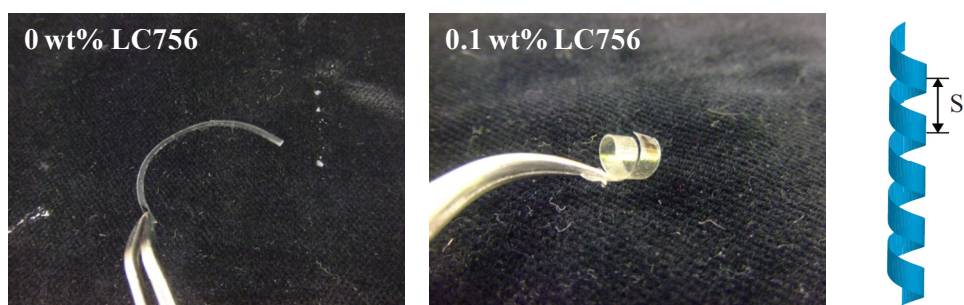


Figure 7.5: Photographs of activated bilayer actuators ($2.5\text{ mm} \times 25\text{ mm}$) with or without chiral dopant in an ambient environment. A schematic representation of a curled tape with a curling pitch (S) is shown.

The response of these activated bilayer actuators to relative humidity (R.H.) variations in a spatially homogeneously humid nitrogen environment is shown in Fig. 7.6. The bilayer tape deforms in curling mode in response to the humid conditions. For reference purposes the response of a pure PA-6 tape to the relative humidity is also studied, and the comparison between the bilayer tape with 0.1 wt % of LC756 and the pure PA-6 is shown in Fig. 7.6b. The result indicates that the pure PA-6 tape does not respond to the variations in humidity with any curling-mode or bending-mode deformation. In Chapter 6, it was shown that the bilayer tape with LC coating (with 0 wt % LC756) on the PA-6 substrate exhibits a bending deformation under the humid conditions. Here, the bilayer tape with LC coating (with 0.1 wt % LC756) on the PA-6 substrate exhibits a curling-mode deformation in response to humidity changes. The curling pitch of the bilayer tape decreases while R.H. increases, which means the bilayer tape is further winded. This curling motion is reversible.

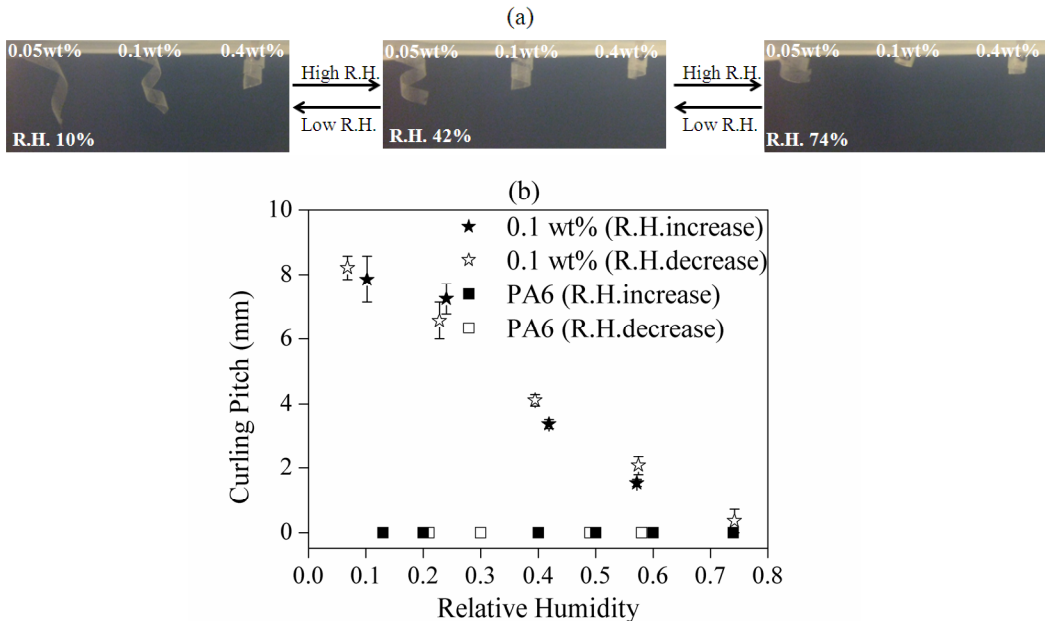


Figure 7.6: (a) Photographs of the curling deformation of the activated bilayer actuators in response to the relative humidity. (b) The curling pitch of the bilayer tape with 0.1wt% LC756 and pure PA-6 tape as a function of humidity.

The relationship between the director-rotation angle of the LC coating and the curling pitch of the spiral bilayer tapes is investigated and shown in Fig. 7.7. Different director-rotation angles were obtained by adding different amounts of chiral dopant into the LC mixtures. Additional information regarding the calculations of the director-rotation angles of the LC coating on the substrate is available in Appendix B. The result indicates that at an identical humidity, different director-rotation angle of the LC network leads to a different curling pitch of the spiral bilayer tape, or even results in the bent bilayer tape (curling pitch is zero). When the R.H. is increased, for the spiral bilayer tapes, they exhibit a curling-mode deformation and their curling pitches decrease. For the bent bilayer tapes, a bending-mode of deformation is created.

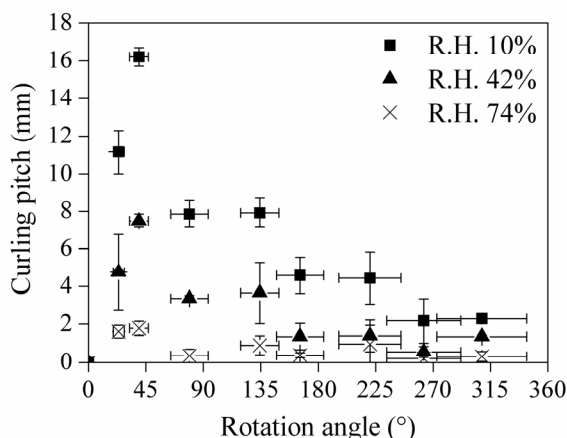


Figure 7.7: *The curling pitch of the bilayer tape as a function of the director-rotation angle of LC756 coating on the substrate.*

Next, the influence of the width of the bilayer tape on the curling deformation is studied. Here, a comparison between three bilayer tapes with the same concentration of the chiral dopant (0.1 wt% LC756), the same thickness and length was carried out. The curling pitches of three bilayer tapes as a function of relative humidity are plotted in Fig. 7.8. It is found that at the same R.H., the pitch of the tape is depended on the width of the tape. A wider bilayer tape has a larger

pitch, which means it is less winded than a narrower bilayer tape. This is expected because the torsion stiffness of the sample increases substantially with increasing width.⁸

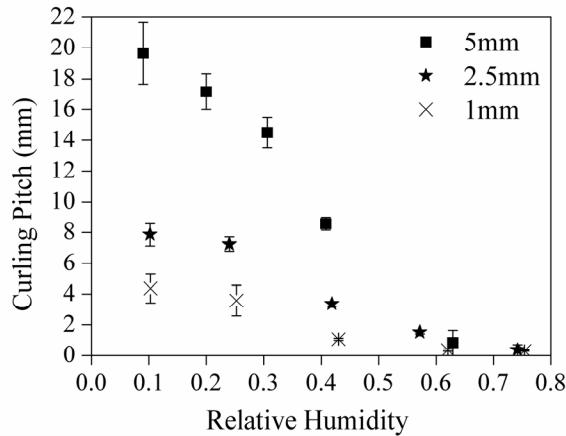


Figure 7.8: The pitch of the bilayer tapes (0.1 wt% LC756) with different widths as a function of the relative humidity.

7.4 Discussion

In the bilayer tape system, chiral dopant LC756 is added into the LC mixture, thus the LC coating shows a director rotation of the nematic phase from the bottom to the top surface of the coating. The director-rotation angle (θ) can be calculated from:

$$\theta = c \times HTP \times d \times 360^\circ \quad (7.2)$$

where c is the weight fraction of chiral dopant and d is the thickness of the LC coating. After activation, again hydrogen bonds are broken. An anisotropic shrinkage is observed with a larger contraction perpendicular to the director and a smaller contraction parallel to the director (see Appendix A). This might cause the left-handed curling of the bilayer actuator after activation. When R.H. increases, the bilayer actuator exhibits curling deformation with decrease of the curling pitch. It is clear that the LC layer exhibits anisotropic expansion/contraction with

varying relative humidity, which causes larger resultant stresses perpendicular to the director and lower stresses parallel to the director.^{9, 10} Because of the director rotation profile in the LC network, these stresses result in the distortion of the sample, leading to the curling deformation.¹¹ When relative humidity increases, it is expected that the LC layer becomes less winded and the curling pitch increases. However, the bilayer actuator shows an opposite deformation behaviour. The curling pitch of the bilayer actuator decreases with increasing humidity. It is speculated that the expansion of the PA-6 substrate induced by the humidity increase is strong enough to prevent the un-winding of sample which is expensive in terms of energy.

Next to the relative humidity, the shape of the bilayer tape and the corresponding curling pitch of the spiral bilayer tape also depend on the width of the tape and the director-rotation angle. Under the same humidity conditions, usually samples with a larger width exhibit a larger curling pitch, which is due to the torsion stiffness as mentioned above. As for samples with the same dimensions, the curling pitch is only related to the director-rotation angle (see Fig. 7.7). When the director-rotation angle (θ) is within $0^\circ \sim 90^\circ$, a maximum curling pitch is obtained when θ is 45° , while a minimum curling pitch is obtained when θ is 0° or 90° . A similar trend can be observed when θ is within $n \times 90^\circ$ to $n \times 180^\circ$ ($n=1, 2, 3, \dots$). It is not surprising that the curling pitch decreases as n increases. More importantly, it is expected that when the rotation angle of the director is exactly at 0° , or a multiple of 90° , the LC mesogens on the top layer of the LC coating are aligned just parallel or perpendicular to the stretching direction of the substrate PA-6 and the bilayer tapes only exhibit a bending-mode deformation.^{2, 12-14} However, it was found that some samples still exhibit a curling-mode deformation, which is because the H-bonds in the LC network are not completely broken.

On the whole, a bilayer system responding to humidity conditions in a curling-

mode deformation was successfully produced. This curling-mode deformation is expected to have a larger humidity responsive actuation than the bending-mode deformation. To prove this, a comparison between these two deformation modes was performed. Here, the strain ($\Delta\epsilon$) of the bilayer actuator upon the R.H. changing is defined by:

$$|\Delta\epsilon| = \frac{|L_2 - L_1|}{L_1} \quad (7.3)$$

where L_1 and L_2 are the end-to-end distance of the bilayer actuator corresponding to different R.H., respectively (see Fig. 7.9). In the case of the bilayer actuator exhibiting a curling deformation, the strain ($\Delta\epsilon$) of the bilayer actuator under humid condition is related to the curling pitch of the actuator, which can be simply expressed by:

$$|\Delta\epsilon| = \frac{|S_2 - S_1|}{S_1} \quad (7.4)$$

where S_1 and S_2 are the curling pitch of the bilayer actuator at different R.H., respectively. The result is shown in Fig. 7.10. The comparison was done between the bent bilayer actuator (0 wt% LC756) and the curled bilayer actuator (0.1 wt% LC756). It clearly illustrates the benefit of curling deformation, i.e. the addition of a small amount of chiral dopant enlarges the strain of the actuator induced by humidity changes in comparison to bending deformation.

Eventually, this bilayer system is supposed to be applied in textile fibres that can exhibit similar humidity-responsive deformation as well. The humidity-responsive deformation could be controlled by adjusting the thickness of the LC polymer coating and the diameter of the fibres. Consequently, a humidity responsive textile can be produced from these fibres.

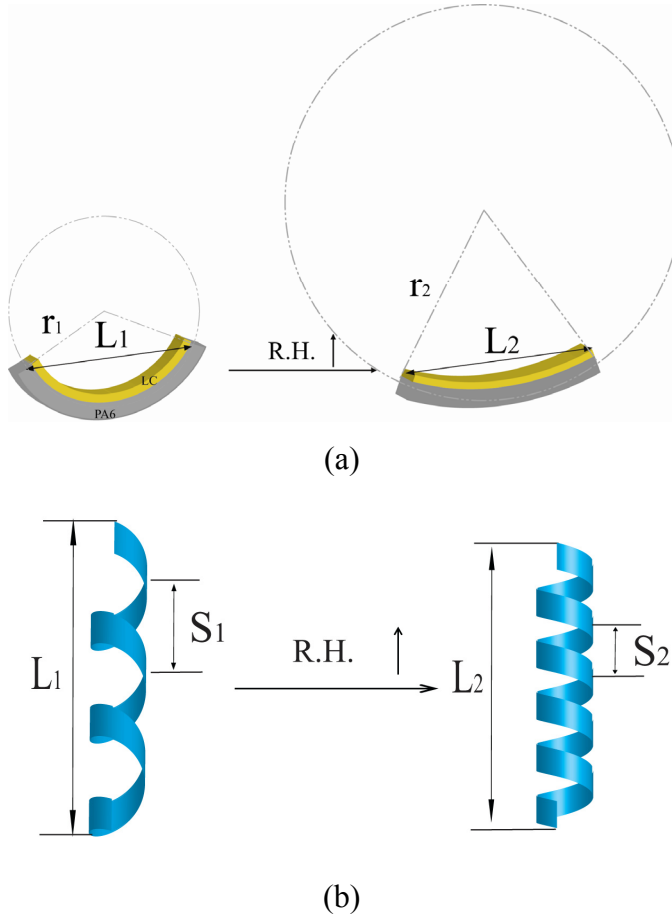


Figure 7.9: (a) Bending deformation (b) curling deformation of the bilayer actuators under humid conditions.

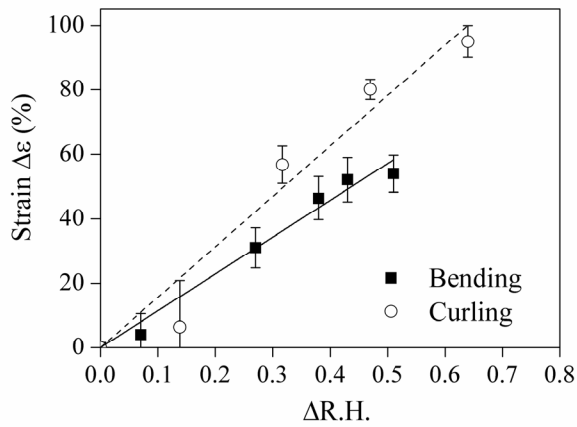


Figure 7.10: The bending/curling deformation strain of the bilayer actuators with 25- μm -thick PA-6 and $\sim 4\text{-}\mu\text{m}$ -thick LC coating as a function of the R.H. changes.

7.5 Conclusions

In this chapter, a humidity responsive bilayer system was described, which consists of an oriented polymer substrate (PA-6) and a LC coating. A certain amount of chiral dopant is added into the LC mixture to induce rotation of the LC mesogens in the director along the coating thickness, which results in the formation of a spiral humidity responsive bilayer actuator, except when the LC director is just rotated at 0° , 90° and a multiple of 90° . It was also investigated that the curling pitch of the spiral humidity responsive bilayer tape can be controlled with adjusting the amount of the chiral dopant and the width of the tape. Under humid conditions, the bilayer system exhibits a curling deformation, which shows a greater humidity responsive actuation compared to the bilayer system exhibiting a bending deformation.

7.6 References

1. D. J. Broer, C. L. van Oosten, K. D. Harris, C. W. M. Bastiaansen, J. Lub and M. C. Luengo Gonzalez, Liquid crystal networks and self-organizing hydrogels: nanotechnology towards soft actuators and nanoporous systems, <http://www.sbpamat.org.br/icam2009dir/submission/palestrante/arquivos/PP2.pdf>
2. Y. Sawa, F. F. Ye, K. Urayama, T. Takigawa, V. Gimenez-Pinto, R. L. B. Selinger and J. V. Selinger, *Proc Nat Acad Sci USA*, 2011, **108**, 6364-6368.
3. H. Fujikake, M. Kuboki, T. Murashige, H. Sato, H. Kikuchi and T. Kurita, *J Appl Phys*, 2003, **94**, 2864-2867.
4. H. Aoyama, Y. Yamazaki, N. Matsuura, H. Mada and S. Kobayashi, *Mol Cryst Liquid Cryst*, 1981, **72**, 127-132.
5. M. R. Wilson and D. J. Earl, *J Mater Chem*, 2001, **11**, 2672-2677.
6. C. L. van Oosten, PhD thesis, Eindhoven University of Technology, 2009.
7. K. D. Harris, C. W. M. Bastiaansen and D. J. Broer, *Macrom Rapid Comm*, 2006, **27**, 1323-1329.

8. K. J. Bathe and A. Chaudhary, *Int J Numer Meth Eng*, 1982, **18**, 1565-1568.
9. K. D. Harris, C. W. M. Bastiaansen, J. Lub and D. J. Broer, *Nano Lett*, 2005, **5**, 1857-1860.
10. K. D. Harris, C. W. M. Bastiaansen and D. J. Broer, *J Microelectromech Syst*, 2007, **16**, 480-488.
11. L. Teresi and V. Varano, *Soft Matter*, 2013, **9**, 3081-3088.
12. M. Warner, C. D. Modes and D. Corbett, *Proc R Soc A*, 2010, **466**, 3561-3578.
13. M. Warner, C. D. Modes and D. Corbett, *P Roy Soc a-Math Phy*, 2010, **466**, 2975-2989.
14. K. D. Harris, R. Cuypers, P. Scheibe, C. L. van Oosten, C. W. M. Bastiaansen, J. Lub and D. J. Broer, *J Mater Chem*, 2005, **15**, 5043-5048.

8 Technical Assessment

8.1 Introduction

In this thesis, new techniques have been developed to introduce new functionalities into the textile fibres, including light diffraction and actuation, which potentially leads to the novel smart textiles applications. In this chapter, the results of this thesis are discussed with an emphasis on the technology and applications. Potential future research will also be discussed, including some preliminary results.

8.2 Textiles for Fashion Design

The “structural coloration” has been investigated and a new technique, i.e. photoembossing, has been developed in this thesis to create gratings on the surface of fibres to exhibit diffraction-based visual effects. Picot, et al introduced reflection-based optical effects into fibres using a cholesteric liquid crystal (CLC) coating in which the molecules were arranged into a helical structure (see Fig. 8.1).^{1, 2} Although all of these fibres exhibit an angular-dependent visual effect, the fibres based on CLC coatings exhibit a smaller angular dependence. For instance, the fibres using a green reflecting CLC coating shows green colour at normal incidence and only a blue shift can be observed under oblique incidence in one dimension, i.e. along the fibre axis. To generate other colours, the pitch of the helical structure of the CLC coating has to be tuned. The textiles produced from these fibres were predominantly intended for applications in fashion design. The

fibres with diffractive gratings will give the textiles a new visual effect with stronger angular dependence.

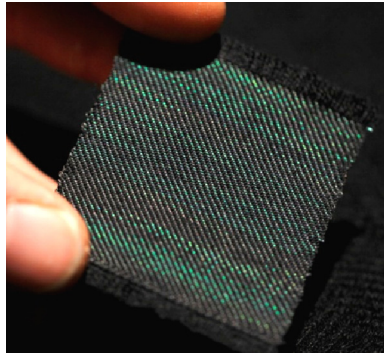


Figure 8.1: *Woven fabric composed of a black cotton thread and PA-6 monofilaments. The monofilament is coated with a cholesteric liquid crystal layer giving the green metallic aspect to the fabric.²*

8.3 Biomedical Application

A tissue engineering scaffold is a temporary supporting structure for the cell in-growth and proliferation, which attempts to mimic the function of the natural extracellular matrix (ECM).³ In order to create an ideal scaffold served for tissue engineering, it is important to mimic the surface relief structures of natural ECM, which plays an important role in the cell behaviour, e.g. cell adhesion and proliferation. Non-wovens based on electrospun nano- and micro-fibres are nowadays extensively investigated for tissue engineering.^{4,5} Photoembossing has been used for the first time to texture surfaces of electrospun fibres.⁶ The biocompatible polymer binder, i.e. polymethyl methacrylate (PMMA) and the monomer trimethylolpropane ethoxylate triacrylate (TPETA) were utilised for electrospinning and photoembossing whilst maintaining a fibrous structure (see Fig. 8.2). It was found that cells adhere faster on the photopolymer blend compared to pure PMMA without pre-coating the surface with proteins. However, there was no significant difference between the smooth and the embossed surfaces. This was attributed to PMMA binder not being suitable for endothelial

cell adhesion.

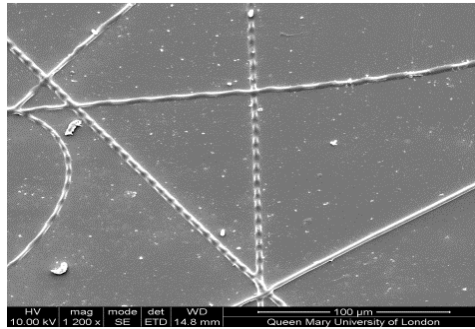


Figure 8.2: SEM of photoembossed PMMA-TPETA.⁶

PMMA was replaced by polylactic-co-glycolic acid (PLGA). A better cell adhesion and proliferation compared to smooth photopolymer and pure PLGA films was obtained for the embossed surfaces. Attempts to get a completely degradable system that can be photoembossed to allow complete tissue takeover were done. PLGA was blended with a PEG-diacrylate and a thiol to get a photopolymer blend that showed complete and faster degradation than pure PLGA polymer. This was attributed to the high hydrophilicity of the crosslinked network which enhanced hydrolysis of ester bonds.

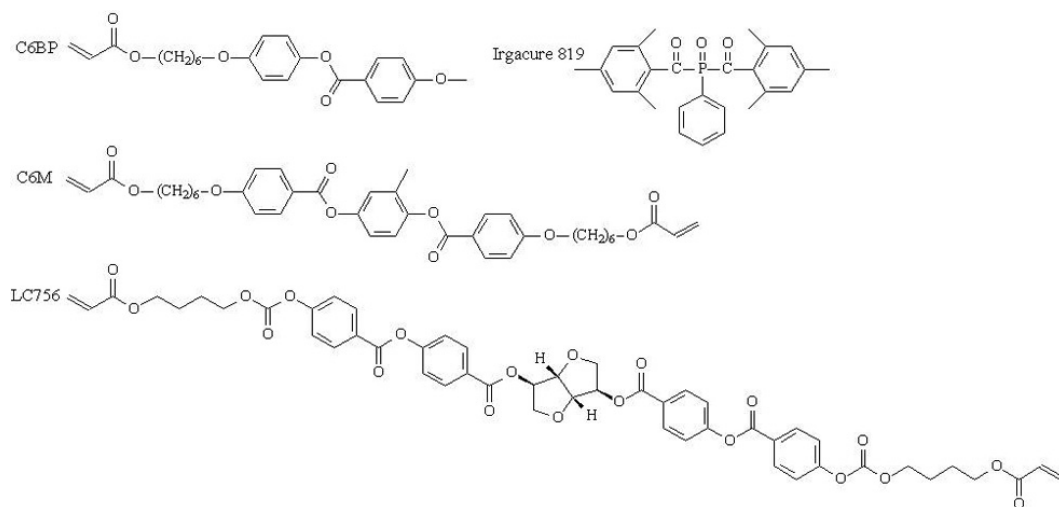
The results in the above-described studies illustrate that photoembossing can be used to produce surface relief structures on electrospun fibres. The biocompatible and biodegradable photopolymer blends are utilised for the application in the tissue engineering.

8.4 Breathable Textiles

Breathable textiles that can change water vapour transmission rate in response to environmental condition are developed to improve the wearing comfort. Such breathable textiles can be either humidity responsive or thermal responsive. In Chapters 6-7, a humidity responsive liquid crystal network was integrated with the oriented polymer substrate, mimicking a fibre made of an oriented polymer, to

fabricate a bilayer actuator. This bilayer system was intended for the fabrication of humidity responsive fibres and it is expected that breathable textiles can be produced from these fibres and change the water vapour transmission rate in a response to changes in humidity conditions in the environment.

Thermal responsive actuator based on the liquid crystal network can also be developed for the textile applications. The LC mixture utilised for the thermal responsive liquid crystal network consists of 76 wt% C6BP (Synthon) and 24 wt% C6M (Merck). The liquid crystal C6BP has a glass transition temperature above room temperature and a modulus at room temperature around 1-3 GPa.⁷ The addition of the methyl group to the rigid part of the molecule makes the polymerised network to be more ductile. C6M is used as a crosslinker for mechanical stability. The photoinitiator Irgacure 819 is added for the photopolymerisation. A small amount of chiral dopant LC756 is added to induce the desirable director rotation in the liquid crystal network. The chemical structures of these materials are shown in Scheme 8.1.



Scheme 8.1: Chemical composition of the thermal responsive LC mixture.

The investigation was first carried out on the pure LC tape. To get a director rotation, a home-made LC cell was prepared using two glass slides coated with rubbed polyimide that were put on top of each other at an angle of 45°. The LC

mixture containing tiny amount of chiral dopant LC756 was filled into the cell in the isotropic state, then cooled down to the nematic phase and subsequently UV-cured. As a result, a single layer LC tape with director rotation of 45° was obtained. The investigation on the thermal responsive behaviour of such a tape was carried out in a silicon oil bath that gives a uniform temperature around the sample. The result is shown in Fig. 8.3. It clearly illustrates that the tape responds to the temperature via curling deformation. The tape first becomes less curled upon heating, at a certain temperature it becomes flat, while subsequently, the tape curls up again at the same moment that the outer surface of tape becomes the inner surface. Such a thermal responsive liquid crystal network can be integrated into the oriented polymer substrate to fabric a bilayer actuator.

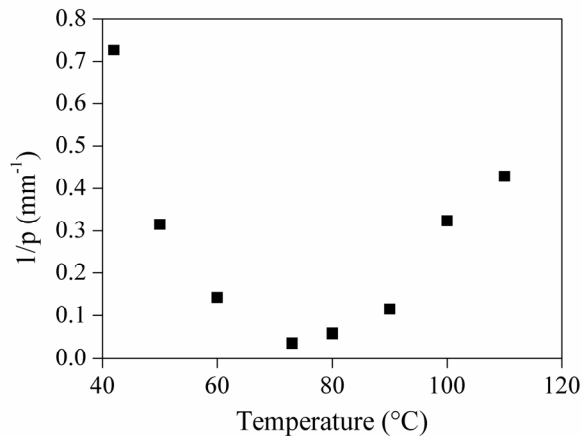


Figure 8.3: Inverse curling pitch ($1/p$) of spiral LC film as a function of temperature in the second heating run.

These humidity or temperature responsive bilayer actuators will be utilised to fabricate responsive fibres. In a fabric, it is expected that the pores among these fibres are open and closed based on the shape deformation of fibres responding to humidity or temperature. Thus breathable textiles can be obtained that change the water vapour transmission rate and air permeability in response to environmental condition without electrical field.

8.5 Strain Sensor

Detecting the deformations of materials is important to monitor the conditions of materials and prevent the mechanical failure. In the past, strain sensors have been produced by attaching a metal array on the surface or by embedding the fibre Bragg grating (FBG) sensors in the material.⁸⁻¹¹ In the first case, deformations can be detected through changes in resistance of the metal grid. The FBG is a type of distributed Bragg reflector constructed in an optical fibre in which the core refractive index is periodically modulated so that it acts as a wavelength-selective reflection filter, reflecting particular wavelengths of light and transmitting all the others.¹² The refractive index modulation is achieved by exposing the core to an intensive UV interference pattern or by a phase mask. Stretching causes a change in the grating period, leading to a change in wavelength of the reflected light. Such kind of sensors can be utilised for the structural health monitoring, e.g. civil works, road and rail bridges.¹²

Cholesteric liquid crystal (CLC) polymers show another possibility to fabricate a flexible strain sensor. CLCs are a type of liquid crystals with a helical structure, which can reflect circular polarised light at a given wavelength defined as:

$$\lambda = \bar{n}p \quad (8.1)$$

where \bar{n} is the mean refractive index of the liquid crystal, p is the length of pitch. When the pitch length is of the same order of magnitude as the wavelength of visible light, the CLCs show a colour in the visible range, which can be detected by eye. As for the responsive CLCs, this pitch can change upon external triggers, for instance, strain, resulting in colour change, which enables the use of CLCs as optical strain detectors that do not require batteries.¹³⁻¹⁶ Previously, a mechanically induced colour changes has been predicted and demonstrated for CLC elastomers.^{17, 18} These strain sensors are very useful for detecting large

deformations, which might have applications in systems with large shape changes, e.g. morphing aircraft that can change wing shapes to adapt to varying flight conditions.¹⁹ On the other hand, an optical sensor to detect small uniaxial deformation in oriented polymer films was developed,²⁰ which consists of a CLC network coating and an oriented substrate, e.g. a uniaxially-stretched PA6 film. Uniaxially stretching leads to a thickness reduction of the sample along the orientation direction, resulting in a decrease of the helical pitch of the CLC network coating and the corresponding reflective wavelength. This is reflected in a colour change of sample (see Fig. 8.4). Such kind of strain sensor can be utilised to detect the mechanical fracture of materials, for instance, automotive parts based on engineering materials.

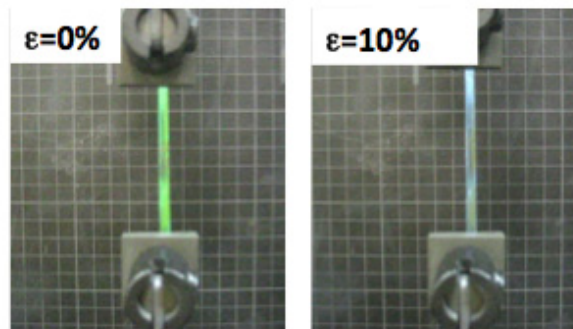


Figure 8.4: Images of strain sensor.²⁰

8.6 Recommendations for Future Research

In conclusion, in this thesis it was demonstrated that photoembossing and responsive liquid crystal networks can be used to introduce new functionalities into fibres or tapes, leading to a number of potential applications. However, there are still many open questions that are not yet fully understood, such as the mechanism of deformation of the bilayer actuator. A deeper understanding and modelling of actuation are desirable. More importantly, the bilayer actuator system discussed in this thesis will be eventually transferred from thin tapes to

monofilaments/multifilaments. It has been tried to spray a humidity responsive LC coating on filaments. A uniform LC coating can be formed on the monofilaments. On the other hand, de-wetting problem occurs when the coating is applied on the thin multifilaments (diameter $< 50 \mu\text{m}$) (see Fig. 8.5), which is probably due to the high surface tension. Future studies to reduce the surface energy, e.g. adding surfactant into the LC mixture, should be done.

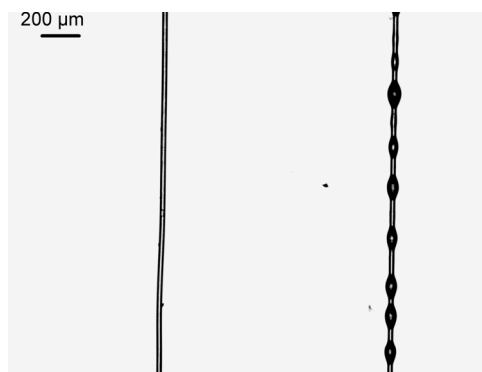


Figure 8.5: Optical microscopy image of filaments ($\sim 30 \mu\text{m}$) without LC coating (left side) and with LC coating (right side).

8.7 References

1. O. T. Picot, M. Dai, T. Peijs and C. W. M. Bastiaansen, *Mater Res Soc Symp Proc*, 2012, **1403**, 113-118.
2. O. T. Picot, M. Dai, D. J. Broer, T. Peijs and C. W. W. Bastiaansen, *Acs Appl Mater Inter*, 2013, DOI: 10.1021/am401438z.
3. W. Y. Yeong, C. K. Chua, K. F. Leong and M. Chandrasekaran, *Trends Biotechnol*, 2004, **22**, 643-652.
4. J. Lannutti, D. Reneker, T. Ma, D. Tomasko and D. F. Farson, *Mat Sci Eng C-Bio S*, 2007, **27**, 504-509.
5. F. Yang, R. Murugan, S. Wang and S. Ramakrishna, *Biomaterials*, 2005, **26**, 2603-2610.
6. N. F. Hughes-Brittain, O. T. Picot, L. Qiu, C. Sanchez, T. Peijs and C. W. M. Bastiaansen, *Mater Res Soc Symp Proc*, 2012, **1418**, 127-132.

7. C. L. van Oosten, PhD thesis, Eindhoven University of Technology, 2009.
8. R. Suo, X. F. Chen, K. M. Zhou, L. Zhang and I. Bennion, *Meas Sci Technol*, 2009, **20**, 034015.
9. M. Silva-Lopez, W. N. MacPherson, C. Li, A. J. Moore, J. S. Barton, J. D. C. Jones, D. H. Zhao, L. Zhang and I. Bennion, *Appl Opt*, 2005, **44**, 6890-6897.
10. X. W. Shu, K. Chisholm, I. Felmeri, K. Sugden, A. Gillooly, L. Zhang and I. Bennion, *Appl Phys Lett*, 2003, **83**, 3003-3005.
11. Z. Wisniewski, R. Wisniewski and J. L. Nowinski, *Rev Sci Instrum*, 2001, **72**, 2829-2831.
12. I. Bennion, L. Zhang and L. A. Everall, *Strain*, 2000, **36**, 115-121.
13. N. Herzer, H. Guneyusu, D. J. D. Davies, D. Yildirim, A. R. Vaccaro, D. J. Broer, C. W. M. Bastiaansen and A. P. H. J. Schenning, *J Am Chem Soc*, 2012, **134**, 7608-7611.
14. Y. Han, K. Pacheco, C. W. M. Bastiaansen, D. J. Broer and R. P. Sijbesma, *J Am Chem Soc*, 2010, **132**, 2961-2967.
15. A. Mujahid, H. Stathopoulos, P. A. Lieberzeit and F. L. Dickert, *Sensors*, 2010, **10**, 4887-4897.
16. C. K. Chang, C. W. M. Bastiaansen, D. J. Broer and H. L. Kuo, *Macromolecules*, 2012, **45**, 4550-4555.
17. P. Cicuta, A. R. Tajbakhsh and E. M. Terentjev, *Phy Rev E*, 2004, **70**, 011703.
18. P. Cicuta, A. R. Tajbakhsh and E. M. Terentjev, *Phys Rev E*, 2002, **65**, 051704.
19. H. Baier and L. Datashvili, *Int J of Aeronautical & Space Sci*, 2011, 225-240.
20. O. T. Picot, M. Dai, E. Billoti, D. J. Broer, T. Peijs and C. W. M. Bastiaansen, *RSC Adv*, 2013, in submission.

APPENDIX A: Anisotropic deformation of LC polymer actuator

In the bilayer system, the LC coating becomes humidity responsive after activation and swells under humid conditions. The dimension changes of the pure LC polymer after the activation and under humid conditions are discussed in detail in this section.

The LC monomer mixtures (without any chiral dopant LC756) were filled into the anti-parallel aligned cells for homogeneous alignment obtained from INSTEC (United States) in the isotropic state, and the temperature was subsequently cooled down to the nematic region of the monomer mixture. UV polymerisation was performed in nitrogen atmosphere using an UV Exfo Mercury Lamp. The uniaxial planar aligned LC films with the thickness of approximately 18 μm were then obtained.

The expansion/contraction of the uniaxial planar aligned film induced by activation and humidity changes was monitored in a Perkin-Elmer TMA 7 thermal mechanical analysis system. The sample was clamped held in a vertical position under a 60 mN load. This force was intended to ensure the film was fully straight. At time=1 min, the sample was first immersed in 0.1M NaOH for 25 s for the activation, followed by flashing with water for 10 s, and then drying in air. At time=60 min, the sample was immersed in water. The length (L) of the sample during the whole procedure was recorded by TMA software. The length of the sample before activation is set as the original length (L_0). In Fig. A1, the expansion/contraction (%) of the sample is shown parallel and perpendicular to the nematic director. It was observed that once the film is activated in alkaline solution, hydrogen bonds are broken and immediately swelling is observed in both directions of the film, perpendicular and parallel to the director. After activation, the film is dried in ambient condition, some water is extracted from the film and

the film shrinks. A larger contraction is observed perpendicular to the director and a smaller contraction parallel to the director. This assumes that some polymerisation shrinkage which was frozen in the network and was released after activation.¹ In combination with the increased order, the film shows anisotropic contraction after air drying.² Subsequently, when the sample was immersed in water, a strong anisotropic expansion was observed. The expansion perpendicular to the director is significantly larger than the expansion parallel to the director. This anisotropic swelling is same as the observation in the previous study.³ Remarkably, the samples were only activated in 0.1M NaOH for 25 s, it is expected that the hydrogen-bond gradient exists in the network as we found in the bilayer system.

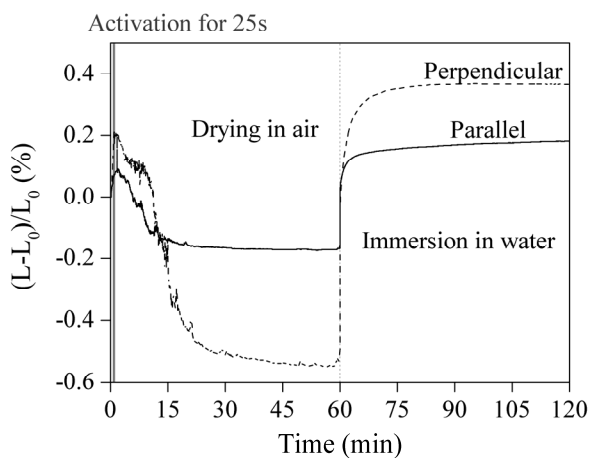


Figure A1: Anisotropic contraction/expansion of poly(*n*OBA/12%C6M) films during and after activation in 0.1M NaOH.

References

1. R. A. M. Hikmet, B. H. Zwerver and D. J. Broer, *Polymer*, 1992, **33**, 89-95.
2. C. L. van Oosten, PhD thesis, Eindhoven University of Technology, 2009.
3. K. D. Harris, C. W. M. Bastiaansen, J. Lub and D. J. Broer, *Nano Lett*, 2005, **5**, 1857-1860.

APPENDIX B: Calculation of director rotation angle

In this thesis, chiral dopant is added into the LC mixture to induce the rotation of the director, which can be calculated from

$$\theta = \frac{d}{p} \times 360^\circ \quad (\text{B.1})$$

Where d is the thickness of the LC coating on the substrate, p is the helical pitch of chiral nematic phase in which the LC mesogens in-plane rotate 360° throughout the director. Since

$$p = \frac{1}{HTP \times c} \quad (\text{B.2})$$

The Eq (B.1) can be expressed by:

$$\theta = c \times HTP \times d \times 360^\circ \quad (\text{B.3})$$

where c is the concentration of the chiral dopant and HTP is the helical twisting power which is constant for the same chiral dopant in the same LC system. When the LC coating thickness (d) is constant, different director-rotation angles can be obtained by simply changing the amount of the chiral dopant in the LC mixture.

However, to calculate the director-rotation angle, it is necessary to know the value of HTP of chiral dopant LC756 in the LC system. In this case, a cholesteric aligned LC film was prepared. The anti-parallel aligned cells for homogeneous alignment obtained from INSTEC was filled with the LC monomer mixtures containing 0.5 wt% LC756 in the isotropic state, and the temperature was subsequently cooled down to the nematic region of the monomer mixture. UV polymerisation was performed using an UV Exfo Mercury Lamp to get a cholesteric aligned LC film. The cross section of this LC film was investigated using a FEI Quanta 3D Scanning Electron Microscope. To prevent charging in the electron beam, a thin gold layer was coated on the surface of sample via vapour deposition. The result is shown in Fig. B1. The helical pitch can be easily

measured based on the SEM image. Based on the Eq (B.2), the *HTP* of the chiral dopant LC756 can be calculated, which is $\sim 48.78 \mu\text{m}^{-1}$.

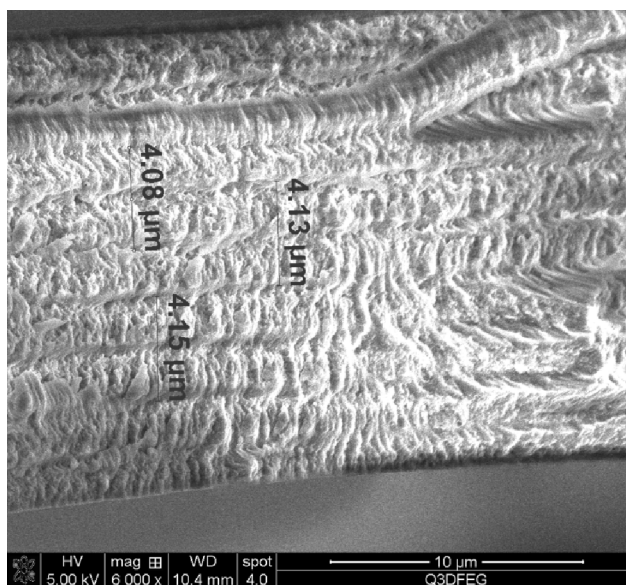


Figure B1: SEM image of the cross section of the chiral nematic aligned LC film (0.5 wt% LC756).

Since the *HTP* is obtained, the director-rotation angle corresponding to different amount of the chiral dopant can be easily calculated from Eq (B.3).

Samenvatting

Slim textiel vertegenwoordigt de volgende generatie van weefsels en producten gemaakt van deze weefsels. Deze nieuwe generatie van ‘intelligente kleding’ legt een grote vraag naar innovatieve ontwikkeling neer bij academici en industrie en biedt nieuwe mogelijkheden voor toepassingen van bijvoorbeeld mode. Het project beschreven in dit proefschrift richt zich op het genereren van nieuwe functionaliteiten in vezels en weefsels met de nadruk op visuele perceptie en respons op externe stimuli zoals luchtvochtigheid.

De hedendaagse methode voor het kleuren van vezels is gebaseerd op het gebruik van anorganische of organische kleurstoffen, welke zorgen voor lichtabsorptie. Deze conventionele vezels hebben een glad oppervlak en een hoekonafhankelijke kleur. Om aan de eisen van de modeontwerpers tegemoet te komen op het gebied van nieuwe visuele effecten zijn nieuwe methoden voor het verkrijgen van lichtdiffractie onderzocht. Dit is gerealiseerd doormiddel van micro- en nano-structuren op het vezeloppervlak.

Het accuraat aanbrengen van texturen op het fiber oppervlak is een uitdaging, in het bijzonder wanneer de structuren loodrecht op de vezel-as gewenst zijn. Foto-embossing is een relatief nieuwe techniek voor het produceren van dergelijke reliëfstructuren die geen gebruik maakt van etsen, wat het mogelijk maakt deze techniek te gebruiken in een spinlijn. Het foto-embossing proces bestaat normaal gesproken uit het aanbrengen van een film op een substraat, gevolgd door een gepatroneerde UV belichting met behulp van een masker of interferentie-holografie bij kamertemperatuur, een thermische ontwikkelingsstap en een extra homogene belichtingsstap voor volledige polymerisatie. Typische fotopolymere mengsels bestaan uit een polymere binder zoals poly (benzyl methacrylaat) (PBMA) en een multifunctioneel monomeer (dipentaerytritol penta-

/hexa- acrylaat) (DPPHA) in een ratio 1/1, hetgeen resulteert in een vast en niet-plakkend materiaal bij kamertemperatuur. In dit proefschrift wordt gebruik gemaakt van een nieuw fotopolymeer mengsel met daarin een polymere binder met een hogere glastransitietemperatuur (T_g) zoals poly (methyl methacrylaat) (PMMA). Dit resulteert in mengsels die hard zijn bij kamertemperatuur, zelfs bij hoge monomeer concentraties ($>1/1$), wat de hoogte van voornamelijk reliëfstructuren met grote periode verbetert. Om interferentie-holografie op een vezel in een spinlijn te simuleren is het belichten van bewegende substraten met een interferentiepatroon van een gepulste laser onderzocht. Hierbij is ook het foto-embossing proces verder geoptimaliseerd door te belichten bij hogere temperaturen. Dit laatste heeft geresulteerd in reliëf-structuren die een factor 2 hoger zijn, tevens is de benodigde optimale belichtingsenergie verminderd.

Van het PMMA-DPPHA fotopolymeer mengsel is direct een vezel gesponnen waarop, met behulp van foto-embossing waarbij gebruik is gemaakt van een masker, oppervlaktestructuren loodrecht op de vezel-as gecreëerd zijn. De resultaten hiervan laten zien dat er goed gedefinieerde structuren op het vezeloppervlak aanwezig zijn bij geoptimaliseerde condities. Echter, de vezels zijn erg bros, hetgeen gerelateerd is aan het gecrosslinkte netwerk in de vezel. Om de mechanische eigenschappen te verbeteren is gebruik gemaakt van een bicomponent-vezel welke is opgebouwd uit een conventionele synthetische kern (PET- of PA6-vezel), met daaromheen een fotopolymere coating. Met behulp van foto-embossing bij hoge temperatuur zijn, door middel van gepulste laser interferentie-holografie, traliestructuren met de tralie-vector parallel op de vezel-as gecreëerd. De resultaten demonstreren dat de diffractie van licht geoptimaliseerd kan worden met behulp van RCWA en dat een relatief kleine pitch van de tralie vereist is voor een grote golflengteverstrooiing. De verkregen gestructureerde vezels vertonen duidelijk gescheiden kleuren onder verschillende kijkhoeken.

Tegelijkertijd is ook gewerkt aan het ontwikkelen van responsieve vezels gebaseerd op vloeibaar kristallijne netwerken die reageren op externe stimuli zoals temperatuur, luchtvochtigheid en/of UV-licht. Hierbij was het primaire doel het ontwikkelen van vezels die buigen of krullen onder invloed van luchtvochtigheid. Men verwacht dat in een weefsel deze deformaties leiden tot veranderingen in vochtdoorlaatbaarheid, luchtpermeabiliteit etc. Voor het creëren van vochtgevoelige vezels is gebruik gemaakt van vloeibaar kristallijne coatings die bestaan uit een chemisch netwerk met daarin waterstofbrug-gebonden eenheden, welke gevoelig zijn voor veranderingen in luchtvochtigheid na activatie. Als modelsysteem is gebruik gemaakt van een uitgerekte polymere film om uitlijning in het vloeibaar kristallijne netwerk te induceren. Op deze manier wordt een film bestaande uit twee lagen gecreëerd waarbij de toplaag uit een goed uitgelijnd vloeibaar kristallijn netwerk bestaat. Voor deze films is de invloed van dikte, breedte en rotatie van de director bij buigen of krullen onderzocht. Hierbij is ondervonden dat het buig- en krulgedrag afhangt van de hoeveelheid chirale dopant. Wanneer geen gebruik wordt gemaakt van chirale dopant en het netwerk in een splay uitlijning verkeerd, zal het systeem bestaande uit twee lagen buigen. Wanneer men wel gebruik maakt van chirale dopant zal de director in het netwerk roteren. In het geval dat de director een rotatie van 90° of een veelvoud van 90° ondergaat, zal het tweelagensysteem buigen. In alle andere gevallen is er sprake van krullen.

De resultaten in dit proefschrift laten zien dat het mogelijk is met behulp van foto-embossing reliëfstructuren op vezels te creëren, waarmee optische effecten gebaseerd op diffractie kunnen worden verkregen. Deze optische actieve vezels zijn potentieel nuttig in de modewereld. Het vochtresponsieve systeem gebaseerd op twee lagen is mogelijk bruikbaar bij ademende textiel-applicaties die reageren op veranderingen in de luchtvochtigheid van de omgeving.

Acknowledgements

At the end of these four years, I would like to spend the last words of my thesis to thank people who have contributed to my thesis and made my time at TU/e so enjoyable.

First of all, I would like to thank my promoters and daily supervisor, Dick Broer and Kees Bastiaansen. Thanks for giving me the opportunity to do research on this interesting and challenging topic. Dick, you are one of the most patient and kind supervisors I have met. Your expertise, profound knowledge and professional guidance considerably helped me especially when I was immobilized in a difficult problem. Kees, your critical questions and different opinions always drive me go further in my project. Your great insight and constructive comments have broadened my mind. Many times you gave me invaluable suggestions and advices when I was lost in my project. I am really grateful to you for all your impressive ideas, careful guidance and inspiring discussions throughout my PhD study in the Netherlands. This thesis wouldn't have been finished without you. I would also like to thank you for intensively structuring and correcting my thesis.

My special thanks owe to Jacques Joosten and Rosalie Greven. Rosalie, thanks for giving me a chance to apply for the PhD positions in the Netherlands. Jacques, we have met with each other since I worked in DSM. I really appreciated you for your help on my application for the PhD project. Without you, I would not be in the Netherlands and started my new life in Eindhoven.

Furthermore, I would like to give my appreciation to Prof. Ton Peijs, Dr. Albert Schenning, Dr. Han Goossens and Prof. Jaap Toonder, for accepting to be members of my defense committee and reading my thesis.

My gratitude also goes to a number of persons deeply involved in this project. Ton Peijs for the interesting discussions and useful suggestions in my project,

Carlos Sánchez for sharing his expertise on the photoembossing and many useful discussions, Bob Fifield for great help on the fibre spinning, Bjorn for helping and training me on the tensile testing system, Olivier and Nanayaa for their help and collaboration in my project, Johan van Haare and the participants to the DPI FPS review meetings for their feedback and constructive questions on our results.

It was my pleasure to work together with so many nice colleagues in the SFD groups. Albert, thanks for your deep and intensive discussion on my project and nice suggestion for my publication. Danqing, Yousefi, Laurens, Tom, Antonio, Yang, Xiaoran, Julien, Jurica, Hitesh, Wanyu and Pit: thank for the nice working environment and all the fun times in the office. Michael, Marjolijn, Claudia, Irén, Jelle, Huub, Ivelina, My, Ties, Paul, Nicole, Amol, Katherine, Natalia, Robert, Debarshi, Michiel, Patrick, Peter, Ko, Joost, Casper, and anyone else I might have forgotten: thank you all for your help and wonderful four years at TU/e. I have had the pleasure to work with two students. Stephanie, I would like to thank you for your working and contribution to my thesis. Yuchen, I also have a good time working with you.

I would like to extend my thanks to Ties de Jong. Thank you very much for the simulation work and all your contributions towards the theoretical analysis of my work. All the discussions with you were very helpful. Many thanks!

Also, my thanks to my friends in the Netherlands: Chunxia, Shufen and Weizhen. The time we spent together was indeed the most memorable time in Eindhoven. There were so much support and encouragement I got from you that I can't express in words. Although we three do not live in the same place now, I still believe that we are friends forever. I really hope we can get together in the near future, enjoying the good time again. Lijing (Shijie) and Kangbo, thanks for helping and the time we spent together in the first year of my PhD study. I learned a lot from you two. Piming and Xiaoxia, thanks for your help, kindness and all delicious dinners. Also special thanks to Danqing, my officemate. I enjoyed the

time spent with you: working late in the evening, discussion on our projects, shopping and having dinner together. I wish you all the best for your future. My gratitude also goes to my lunch partners: Yulan, Yang Yun, Yingyuan, Chunliang, Delei, Liu Hao and Louzhang. The chats during lunch were always very interesting and relaxing. There are two other important persons that I especially would like to thank: Guanna and Yanmei. In the first two years, we spent a lot time together which helped me get used to the life in Eindhoven. I wish both of you all the best for your future developments in academic area.

Last but not least, my appreciation to my parents in China. 我要将这本论文特别献给我的父母，谢谢你们的理解，关爱，支持和包容，才使得我能够顺利完成四年的博士学习。

戴 冕

二零一三年八月

Curriculum Vitae

Mian Dai was born on 11-08-1980 in Changzhou, China. After finishing her bachelor study in 2002 at Donghua University in Shanghai, China, she studied Material Science at the same university. In 2005, she received her Master's degree on the topic of 'Synthesis of Copolyimides and Their Spinnability'. From 2005—2009 she was employed at DSM China Limited. From September 2009, she started a PhD project at Eindhoven University of Technology (TU/e), the Netherlands, under the supervision of prof.dr. D.J. Broer and prof.dr.ing. C.W.M. Bastiaansen, of which the results are presented in this dissertation.

Publications

1. M. Dai, O. T. Picot, J. M. N. Verjans, L. T. de Haan, A. P. H. J. Schenning, T. Peijs and C. W. M. Bastiaansen, Humidity responsive bilayer actuator based on a liquid crystalline polymer network, *ACS Appl. Mater. Inter.*, **2013**, 5(11), 4945-4950.
2. O. T. Picot, R. Alcalá, C. Sánchez, M. Dai, N. F. Hughes-Brittain, D. J. Broer, T. Peijs and C. W. M. Bastiaansen, Manufacturing of surface relief structures in moving substrates using photoembossing and pulsed interference holography, *Macromol. Mater. Eng.*, **2013**, 298, 33-37.
3. M. Dai, T. M. de Jong, C. Sánchez, O. T. Picot, D. J. Broer, T. Peijs and C. W. M. Bastiaansen, Surface structuring of bi-component fibres with photoembossing, *RSC Adv.*, **2012**, 2, 9964-9968.
4. N. F. Hughes-Brittain, O. T. Picot, M. Dai, T. Peijs and C. W. M. Bastiaansen, Effect of polymer binder on surface texturing by photoembossing, *Appl. Surf. Sci.*, **2012**, 258, 8609-8612.
5. M. Dai, O. T. Picot, N. F. Hughes-Brittain, T. Peijs and C. W. M. Bastiaansen, Formation of relief structures on fibres by photoembossing, *J. Mater. Chem.*, **2011**, 21, 15527-15531.